UNIVERSIDAD POLITÉCNICA DE MADRID

ESCUELA TÉCNICA SUPERIOR DE
INGENIEROS DE TELECOMUNICACIÓN

SPONTANEOUS EXCHANGE BIAS FORMATION DRIVEN BY A STRUCTURAL PHASE TRANSITION IN THE ANTIFERROMAGNETIC MATERIAL

TESIS DOCTORAL

ANDREA MIGLIORINI

LICENCIADO EN INGENIERÍA FÍSICA

2018

Departamento de Ingeniería Electrónica

ESCUELA TÉCNICA SUPERIOR DE
INGENIEROS DE TELECOMUNICACIÓN

SPONTANEOUS EXCHANGE BIAS FORMATION DRIVEN BY A STRUCTURAL PHASE TRANSITION IN THE ANTIFERROMAGNETIC MATERIAL

Andrea Migliorini

Licenciado en Ingeniería Física

Dirigida por:

José Luis Prieto Martín, doctor en CC. Físicas

Manuel Muñoz Sánchez, doctor en CC. Físicas

2018

Abstract

Most magnetic devices in advanced electronics rely on the exchange bias effect, a magnetic interaction that couples a ferromagnetic and an antiferromagnetic material, resulting in a unidirectional displacement of the ferromagnetic hysteresis loop by an amount called the "exchange bias field". Setting and optimizing the exchange bias involves a thermal treatment in presence of an external magnetic field, which allows to control the degree of magnetic order in the antiferromagnetic material. In this thesis we demonstrate an alternative process for the generation of exchange bias.

Our study focuses on one of the most common systems for technological applications based on exchange bias, which is the ferromagnetic FeCo coupled to the antiferromagnetic IrMn in the form of a multilayered thin film deposited by magnetron sputtering. We have found the deposition conditions which leave the IrMn layer in a metastable amorphous/nanocrystalline phase. The disordered state of the IrMn prevents the setting of the exchange bias in the adjacent FeCo layer, which shows a centered hysteresis loop with low coercivity, typical of soft ferromagnetic thin films. During the days after deposition, a structural phase transition in the IrMn layer develops spontaneously at room temperature and spreads according to a two-dimensional nucleation and growth process. As the phase transition propagates, the FeCo gets progressively exchange-biased according to the direction of its remanent magnetization.

The structural characterization of the IrMn/FeCo bilayers reveals that the as-deposited amorphous/nanocrystalline IrMn undergoes a spontaneous crystallization which leads to a highly crystalline, chemically-disordered γ-phase. Once the phase transition is completed, the IrMn layer consists of very large single-crystal grains, of the order of few hundred nanometers, with a large density of structural defects which extend through its thickness. The images taken by transmission electron microscopy indicate that the origin of these defects may lie in the polycrystalline nature of the adjacent FeCo layer.

The magnetic characterization of the crystallized samples shows a moderately strong exchange bias with good stability at room temperature. It also reveals some unexpected magnetic and thermal responses which cannot be explained with the granular model for the exchange bias, generally used for polycrystalline materials. In order to justify the properties of the crystallized samples upon field annealing, we analyze the results in light of a strong antiferromagnetic domain walls pinning model, which indicates that the structural defects in the IrMn layer may

play an important role in both the stability and the strength of the exchange bias. Furthermore, we propose a possible mechanism for the initial setting of the exchange bias, which would explain the progressive increase of the exchange bias field during its spontaneous formation, as the crystalline phase propagates.

Finally, we report the interesting possibility of controlling the direction of the exchange bias, simply by switching the magnetization of the FeCo layer as the phase transition propagates. This allows microscopic patterning of the direction of the exchange bias, which is generally not possible unless the sample is locally treated with laser or ion radiation. The study of this mechanism for establishing and tailoring the exchange bias in IrMn/FeCo systems can contribute toward the clarification of fundamental aspects of this phenomenon, as well as toward further developments in the field of spintronics.

Resumen

Un gran número de dispositivos magnéticos en la electrónica moderna se basan en el *exchange bias*, una interacción magnética que acopla un material ferromagnético y uno antiferromagnético, dando origen a un desplazamiento unidireccional del ciclo de histéresis ferromagnético en una cantidad llamada *exchange bias field*. Establecer y optimizar el *exchange bias* implica un tratamiento térmico en presencia de un campo magnético externo, que permite controlar el grado de orden magnético en el material antiferromagnético. En esta tesis, demostramos un proceso alternativo para la generación del *exchange bias*.

Nuestro estudio se centra en uno de los sistemas más comunes para aplicaciones tecnológicas basado en el *exchange bias*, el FeCo ferromagnético acoplado al IrMn antiferromagnético en forma de películas delgadas depositada por magnetrón sputtering. Hemos encontrado las condiciones de deposición que dejan la capa IrMn en una fase amorfa/nanocristalina metaestable. El estado desordenado del IrMn previene el establecimiento del *exchange bias* en la capa de FeCo adyacente, la cual muestra un ciclo de histéresis centrado y con baja coercitividad típico de las películas delgadas ferromagnéticas blandas. Durante los días sucesivos a la deposición, una transición de fase estructural se desarrolla espontáneamente a temperatura ambiente en la capa de IrMn y se expande siguiendo un proceso de nucleación y crecimiento bidimensional. A medida que la transición de fase se propaga, el *exchange bias* se forma progresivamente en el FeCo según la dirección de su imanación remanente.

La caracterización estructural de las bicapas de IrMn/FeCo revela que el IrMn, inicialmente amorfo/nanocristalino, experimenta una cristalización espontánea que conduce a una fase químicamente desordenada de tipo γ, altamente cristalina. Una vez completada la transición de fase, la capa de IrMn contiene granos cristalinos muy grandes, del orden de unos cientos de nanómetros, con una gran densidad de defectos estructurales que se extienden a través de su espesor. Las imágenes tomadas por microscopía electrónica de transmisión indican que el origen de estos defectos puede residir en la naturaleza policristalina de la capa de FeCo adyacente.

La caracterización magnética de las muestras cristalizadas revela un *exchange bias* moderadamente fuerte con buena estabilidad a temperatura ambiente. Las medidas muestran también unas respuestas magnéticas y térmicas inesperadas que no se pueden explicar con el modelo granular del *exchange bias*, generalmente utilizado para materiales policristalinos. Con

el fin de justificar como cambian las propiedades de las muestras cristalizadas durante el recocido a varias temperaturas, analizamos los resultados a la luz de un modelo de fuerte fijación de paredes antiferromagnética, que indica que los defectos estructurales en la capa de IrMn juegan un papel importante tanto en la estabilidad como en la resistencia del *exchange bias*. Además, proponemos un posible mecanismo para el establecimiento inicial del *exchange bias*, lo que explicaría el aumento progresivo del *exchange bias field* durante su formación espontánea, a medida que la fase cristalina se propaga.

Finalmente, abordamos la interesante posibilidad de controlar la dirección del *exchange bias*, simplemente cambiando la imanación de la capa de FeCo a medida que se propaga la transición de fase. Esto permite el modelado microscópico de la dirección del *exchange bias*, lo que generalmente no es posible a menos que la muestra se trate localmente con láser o radiación iónica. El estudio de este mecanismo para establecer y modelar el *exchange bias* en los sistemas de IrMn/FeCo puede contribuir a aclarar aspectos fundamentales de este fenómeno, así como a nuevos desarrollos en el campo de la espintrónica.

Table of Contents

Chapter 1: Introduction

This introductive chapter aims to give the reader a general overview of the main phenomenon studied in this thesis work, the exchange bias. It begins with a short account of the discovery of the phenomenon and its importance in magnetoresistive technological applications. Then, it follows with a brief description of the main phenomenology of the effect, the methods employed to establish a strong exchange bias, as well as the materials which are most commonly used in industrial applications. A more detailed introduction of the aspects relevant to the discussions developed in this work can be found at the beginning of every chapter.

The exchange bias (EB) is one of the most intriguing and fascinating unsolved conundrum of modern physics. It was discovered in 1956 by W. H. Meiklejohn and C. P. Bean and reported for the first time in the scientific journal, Physical Review [Meiklejohn, 1956]:

"A new type of magnetic anisotropy has been discovered which is best described as an exchange anisotropy. This anisotropy is the result of an interaction between an antiferromagnetic material and a ferromagnetic material."

The investigation of Meiklejohn and Bean focused on the temperature dependent magnetic behavior of naturally oxidized Co nanoparticles, modelled as a ferromagnetic (F) Co core enclosed by an antiferromagnetic (AF) CoO shell. These CoO/Co particles showed the standard magnetic response of pure Co particles when measured at room temperature. Nevertheless, when cooled below the Néel temperature of CoO (i.e. 293 K), torque measurements revealed the presence of a unidirectional anisotropy, which they associated to the exchange interaction between the F-ordered spins of the Co and the AF-ordered spins of the CoO, at the interface between the two materials. Furthermore, when the nanoparticles were field-cooled in presence of a saturating magnetic field, the hysteresis loop resulted to be displaced laterally, as shown in their original measurement reproduced in figure 1.1. It is this shift of the hysteresis loop what has made the exchange bias a fundamental phenomenon for technological applications.

For the first three decades since its discovery, the study of this fascinating phenomenon was almost exclusively supported by pure academic interest. It is with the development of Spintronics at the end of the 1980s, that exchange-biased thin films started to be employed in technological applications [Wolf, 2001; Johnson, 2004]. Those years were characterized by major findings about spin-dependent electron transport phenomena, which include the giant

magnetoresistance (GMR), independently discovered by Albert Fert [Baibich, 1988] and Peter Grünberg [Binasch, 1989], both awarded with the Nobel Prize in Physics in 2007.

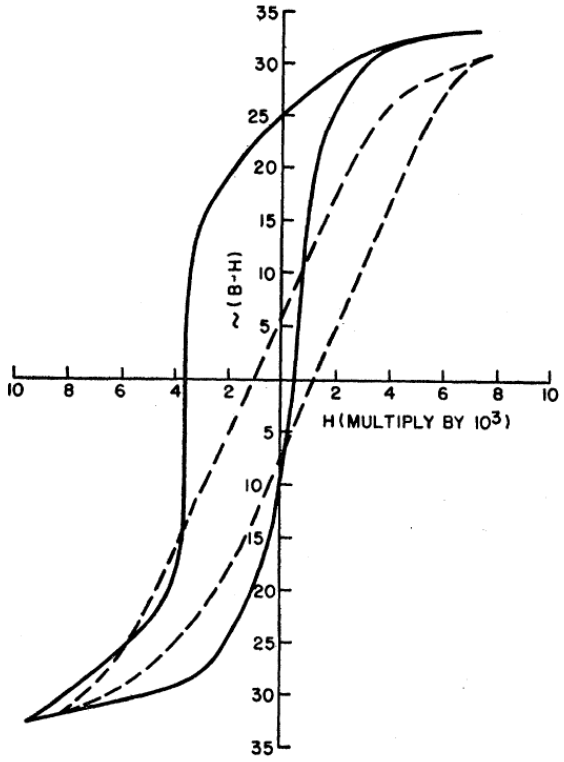

Figure 1.1: Hysteresis loop of partially oxidized Co particles measured at 77 K when field cooled in presence of a saturating magnetic field (solid line) and zero field cooled (dashed line), after [Meiklejohn, 1956].

The exchange bias plays a fundamental role in the operation of spin valves, whose functioning is based on the GMR effect [Dieny, 1991]. A spin valve is a magnetoresistive (MR) multilayered device formed by two ferromagnetic layers separated by a non-magnetic one. The electrical resistance of the device depends on the magnetic alignment of the two F layers, according to the GMR effect. If one of the two F layers is in contact with an AF material, the loop displacement induced by the exchange bias allows the magnetization of the two layers to reverse at different external fields, as can be seen in figure 1.2 [Dieny, 1991]. Hence, the magnetic alignment of the F layers, and thus the resistance of the device, can be controlled by simply switching the free layer with an external field at values close to zero. Thanks to these features and the large MR obtained, exchange-biased spin valves were almost immediately employed in the design of GMR-based sensors [Daughton, 1994], read heads of magnetic hard drives [Tsang, 1994; Childress, 2005], magnetoresistive random-access memories (MRAM) [Daughton, 1992; Åkerman, 2005], and spin transfer torque MRAMs [Kent, 2015]. The great technological interest around MR devices acted as an immense boost to the scientific research

on exchange bias, which has seen an extraordinary acceleration in the last three decades and is still behind many experiments in modern magnetism [Jungwirth, 2016]. Nevertheless, the exchange bias proved to be an extremely complex phenomenon, and a comprehensive theory which can explain and predict all its aspects is still missing.

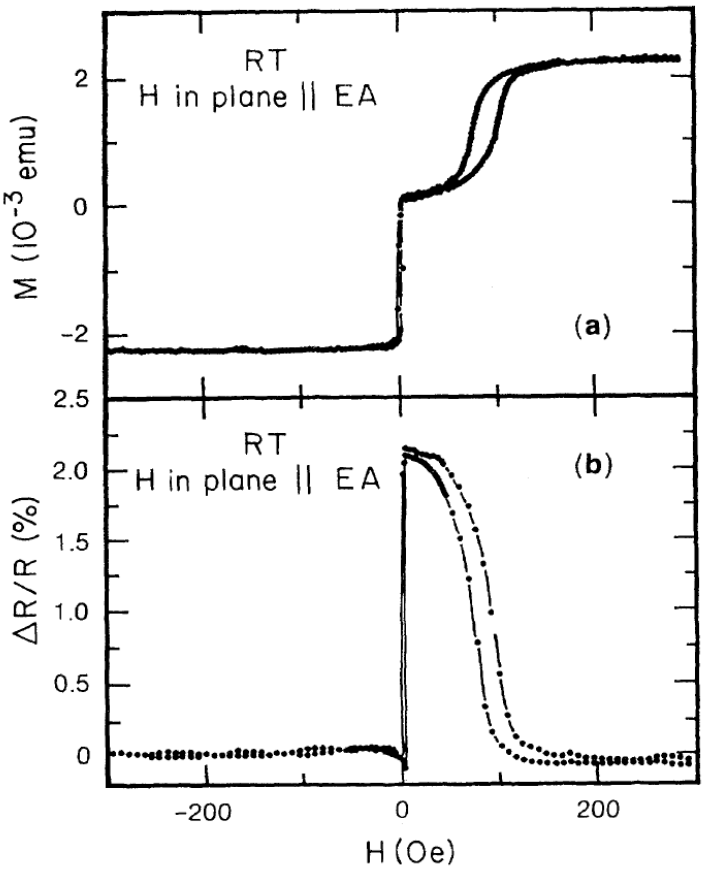

Figure 1.2: a) Magnetometry and b) magnetoresistive response of an exchange-biased spin valve, after [Dieny, 1991].

The most important effect which arises in exchange biased AF/F systems is undoubtedly the lateral displacement of the hysteresis loop of the F material, since this is critical for the operation of spin valves. Despite the complex phenomenology and the incomplete understanding of the effect, the technological importance of the loop displacement allows us to formulate a phenomenological definition of the exchange bias:

Exchange bias arises when a ferromagnetic and an antiferromagnetic material are in direct contact with each other, causing a lateral displacement of the ferromagnetic hysteresis loop.

The magnitude of this loop displacement is represented by the exchange bias field, H_{eb}, which corresponds to the additional external magnetic field needed to reverse the F material. The

exchange bias field is defined as the field value at which the center of the hysteresis loop lies, as shown by the red arrow in figure 1.3. A second important feature is the enhancement of the coercivity of the F material, H_c, defined as half of the width of the hysteresis loop. As shown by the green arrow in figure 1.3, the coercivity of an exchange-biased system increases significantly as compared to the one it had before the exchange bias was established.

Both the loop shift and the coercivity enhancement are fundamental characteristics for the design of technological applications. Nonetheless, the phenomenology of the exchange bias is extremely more complex and multifaceted, and it has been object of several studies since its discovery. In fact, exchange-biased systems are characterized by several other interesting effects and features. Examples of these effects are the reversal asymmetry of the hysteresis loop [Fitzsimmons, 2000], the training effect [Paccard, 1966], the positive exchange bias [Nogués, 2000], the dependence on temperature [Hagedorn, 1967; Schlenker, 1968], time of measurement [Jacobs, 1961], cooling field [Fernandez-Outon, 2008], AF thickness [Xi, 2000], F thickness [Nogués, 1999], crystallinity and texture [Aley, 2008], interface roughness [Pakala, 2000], AF grain size distribution [Vallejo-Fernandez, 2008b] and anisotropy dispersion [McCord, 2003].

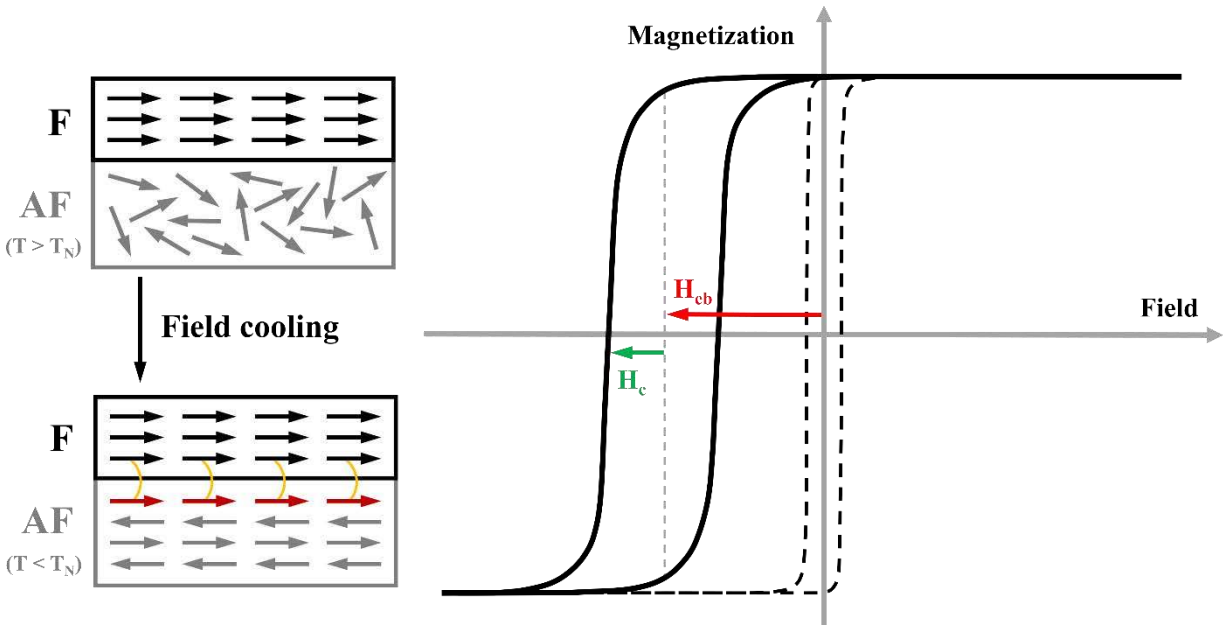

Figure 1.3: Schematic diagram of the hysteresis loop of an AF/F system before (dashed line) and after (full line) the setting of the exchange bias.

The intrinsic complexity of the phenomenon is enhanced by the many different AF/F systems in which exchange bias is detected. Examples of the AF materials used in exchange-biased systems are: oxides (CoO, NiO, FeO, …), nitrides (Fe_2N, CoN, …), sulfides (FeS), flourides

(FeF_2, MnF_2, …), Mn-based AF (FeMn, NiMn, IrMn, …) [Nogués, 1999]. In addition, exchange-biased systems are often produced using distinct deposition techniques, which inevitably lead to different structural, compositional and magnetic properties of the deposited materials. Examples of these deposition techniques are: molecular beam epitaxy, electrodeposition or magnetron sputtering. Therefore, it is not surprising that, despite the several different theoretical models developed to explain the origin and the characteristics of the exchange bias, a comprehensive theory able to predict both qualitatively and quantitatively its phenomenology in different systems has not been developed yet. Full descriptions of both the phenomenon and the theoretical models developed over the years can be found in the several review articles published in the last decades [Nogués, 1999; Berkowitz, 1999; Stamps, 2000; Kiwi, 2001; Nogués, 2005].

To exhibit exchange bias, AF/F systems must undergo a thermal treatment which is generally called the exchange bias setting. The EB setting consists in controlling the magnetic order of the AF so to induce the exchange anisotropy in the F material. The most direct way to set the exchange bias consists in field cooling the system from above the Néel temperature (T_N) of the AF material. A representation of the EB setting of an AF/F system by field cooling is presented in figure 1.3. At temperatures higher than T_N, the AF material is paramagnetic and there is no exchange interaction at the AF/F interface. The corresponding magnetic response of the system above T_N is represented by the dashed hysteresis loop, which shows no lateral displacement, and it is virtually equivalent to the response of the sole F material. When the system is cooled below T_N in presence of a magnetic field, the magnetic ordering of the AF material is influenced by the exchange interaction with the F spins at the interface between the two materials; thus, the exchange bias is set. Accordingly, the hysteresis loop of the system after the EB setting, represented by the full line in figure 1.3, is laterally shifted. The loop displacement is most often in the direction opposite to the magnetization of the F material, and it is sometimes referred to as “negative exchange bias” when ambiguity with “positive exchange bias” is possible [Nogués, 2000]. The role of the external field during the cooling is to saturate the F material and it is not necessary to induce the exchange bias, as this is only the result of the exchange interaction at the AF/F interface [Takahashi, 1980].

Another way to set the exchange bias involves the thermal activation of the small AF grains in polycrystalline AF/F systems [Fulcomer, 1972b], which happen to be the ones used in technological applications. In these materials the exchange bias can be set by annealing the polycrystalline system in presence of a saturating magnetic field, at temperatures lower than

T_N. This method allows to set the exchange bias at moderate temperatures (~ 500 K), thus avoiding the damages related to high-temperature annealing [Vallejo-Fernandez, 2008c]. Both the field cooling from above T_N and the thermal activation of polycrystalline systems operate on a macroscopic level, as the exchange bias is intrinsically set in the whole sample. In fact, microscopic tailoring of the exchange bias is generally not possible unless the sample is locally treated with laser [Johnson, 2003] or ion radiation [Mougin, 2001; Ueltzhöffer, 2015].

Among all the AF and F paired materials for exchange bias, the system most commonly used in industry consists in a polycrystalline IrMn/FeCo thin film deposited by magnetron sputtering. This AF/F bilayer provides large exchange bias field [Fuke, 1997; Iwasaki, 1997] and high thermal stability [Samant, 2000; Childress, 2001], in addition to the good resistance to corrosion of the IrMn [Devasahayam, 1998] and its small critical thickness (i.e. the minimum AF thickness which induces exchange bias) [McFadyen, 2006]. Investigations on the compositional dependence of the exchange bias in IrMn-based systems revealed that the optimal composition is $Ir_{25}Mn_{75}$ [Tsunoda, 2006], which is therefore the common choice in technological applications. Since the Néel temperature of the IrMn is about 690 K, the exchange bias is usually set by thermal activation of the AF grains. In 2010, the research group led by Prof. K. O'Grady at the University of York presented a new paradigm for exchange bias in polycrystalline IrMn/FeCo thin films with small grains (i.e. grain diameter smaller than 15 nm), which they called the York Protocol [O'Grady, 2010]. Their work is based on the granular model developed by Fulcomer and Charap [Fulcomer, 1972b], and it is able to predict most of the features of IrMn/FeCo bilayers, as well as design exchange-biased systems in order to fulfill specific technological requirements.

In the present work, we show an alternative mechanism to set the exchange bias in IrMn/FeCo bilayers deposited by magnetron sputtering, from targets of nominal composition $Ir_{25}Mn_{75}$ and $Fe_{40}Co_{60}$. We found the sputtering conditions that leave the as-deposited IrMn in an amorphous metastable state, which does not induce exchange bias in the FeCo. In fact, our as-deposited IrMn/FeCo bilayers show no exchange bias nor coercivity enhancement. Then, at room temperature, the amorphous IrMn spontaneously undergoes a structural phase transition, which develops according to a two-dimensional nucleation and growth process, leading to a highly crystalline and chemically disordered phase. During this process, the FeCo layer progressively gets exchange-biased as the phase transition propagates, with the direction of the induced exchange bias oriented according to remanent magnetization of the FeCo. By changing the remanent magnetization of the FeCo during the phase transition in the IrMn, we were able to

tailor the direction of the exchange bias microscopically. Therefore, this alternative approach to set the exchange bias allows the patterning of the EB direction, without the need of further treatment but the switching of the external field during the phase transition in the IrMn, a thing that could open the door to explore local magnetic interactions at the interface [Martí, 2012; Wang, 2012; Morales, 2015] and to design innovative devices. What is presented here is a new mechanism to set the exchange bias which has never been reported before, and the results of this study were recently published on the scientific journal, Nature Materials [Migliorini, 2018].

1.1 Outline

This doctoral thesis is organized in six chapters. Chapter two covers the experimental techniques employed to deposit and characterize the samples. Chapter three focuses on the structural characterization of IrMn and IrMn/FeCo thin films, mainly performed by X-ray diffractometry and transmission electron microscopy, before, during and after the phase transition of the IrMn from amorphous to crystalline. Chapter four covers the magnetic characterization of IrMn/FeCo bilayers, with particular emphasis on both the formation of the exchange bias during the phase transition of the IrMn and the magnetic properties of the crystallized samples upon performing temperature dependent experiments. The magnetic characterization was mainly achieved by vibrating sample magnetometry and magneto-optical Kerr microscopy. In chapter five we discuss the relation between the IrMn phase transition and the properties of the exchange bias detected in crystallized samples, including possible interpretations of how the exchange bias is set as the crystalline phase spreads within the AF layer. The final chapter consists in a summary of the results obtained and a brief presentation of the consequent studies and experiments which are under development.

Chapter 2: Experimental Techniques

The purpose of this chapter is to introduce the reader to the experimental techniques employed during the development of this research work. The experimental work was performed among four scientific institutes: The Institute for Optoelectronic Systems and Microtechnology of the Universidad Politécnica de Madrid (ISOM-UPM), the IMDEA Nanociencia Institute (IMDEA), the University of York (UoY) and the Instituto de Ciencia de Materiales de Madrid (ICMM). Each section includes a brief description of the experimental techniques, the equipment employed, and the types of measurement performed. The samples presented in this study are multilayered thin films deposited by magnetron sputtering over silicon substrates. Microdevices based on these thin films were produced by a combination of optical lithography, lift-off and dry etching. The structural properties of the samples were characterized by X-ray diffractometry and transmission electron microscopy, whereas the magnetic response was analyzed by vibrating sample magnetometry, magneto-optic Kerr microscopy and magnetic force microscopy.

2.1 Sample Preparation

All the samples presented in this research work were produced at the ISOM-UPM facilities, which include a 100-1000 class cleanroom where substrates preparation and sample fabrication were performed. The samples were deposited over two types of silicon substrates: thermally oxidized Si (111), with a SiO_2 thickness of 0.4 μm, and naturally oxidized Si (100). In addition, plan-view transmission electron imaging required the use of specific TEM grids. The silicon substrates were cut from commercial wafers using a Kulicke & Soffa Precision Dicing System Model 780. Substrates of 4×3 mm^2, 5×5 mm^2 and 10×5 mm^2 were used, depending on the measurement requirements. In preparation to thin film fabrication, substrates were cautiously cleaned with acetone and isopropyl alcohol (IPA).

2.1.1 Magnetron Sputtering

Sputtering is a physical vapor deposition (PVD) technique known since its discovery in 1852 [Grove, 1852]. With the introduction of unbalanced magnetrons in the late 1980s, sputtering undergoes a rapid commercial diffusion, thanks to great performance improvements [Kelly,

2000]. The main advantage of magnetron sputtering is the high growth-rate achievable, which makes it the most convenient choice among thin film coating techniques. Figure 2.1 shows a schematic diagram of a magnetron sputtering system. A target plate is kept at a negative potential of hundreds of volts in presence of glow discharged plasma. The energetic ions of the plasma are accelerated toward the target and the collisions result in the removal of target atoms, which then condense on a substrate. The plasma is produced by ionization of an inert gas, which is generally Ar. The ionization of the plasma is increased by the presence of a magnetic field parallel to the target, which is produced by permanents magnets properly placed underneath the cathode. This magnetic field constrains the secondary electrons to follow a spiral path along the field lines, increasing the probability of electron-atom collisions by an order of magnitude. This results in a dense plasma near the target surface, which leads to higher sputtering rate. In order to deposit a non-conductive target, a radiofrequency (RF) magnetron is required. In fact, when applying a DC negative potential, the bombardment with positive ions would quickly induce a positive charge on the non-conductive target surface. This positive charge would repulse further ions, and this would stop the sputtering. The use of a radiofrequency power generator allows to balance the surface charges when the positive potential is applied, leading to practical sputtering rate.

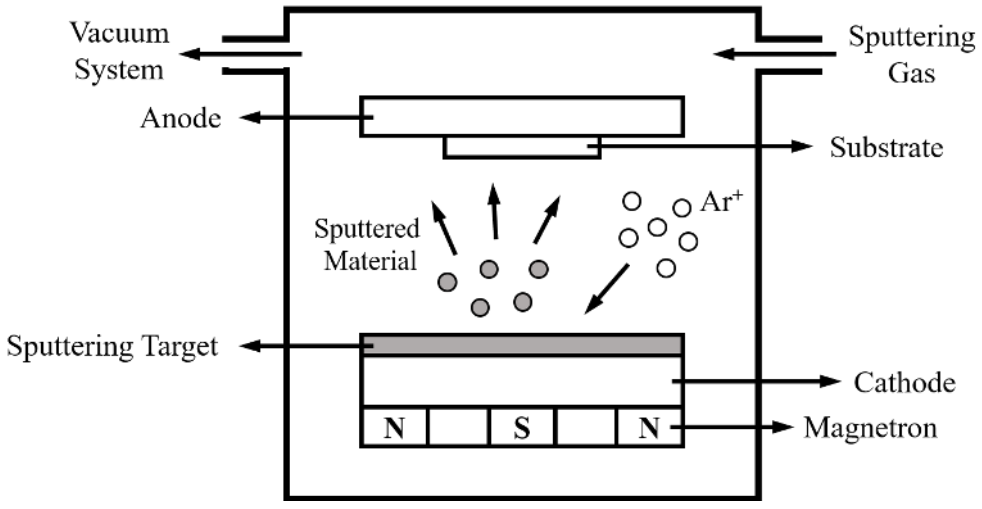

Figure 2.1: Schematic representation of a magnetron sputtering system.

All the samples presented in this work were deposited in the sputtering system of the ISOM-UPM. This sputtering system consists of a main vacuum chamber which can reach a base pressure of 10^{-8} mbar, a group of five DC magnetrons and one RF magnetron properly separated, so to avoid contamination among the targets, and a preload chamber. The magnetrons are positioned circularly at the top of the vacuum chamber and the sample holder

can rotate below each target thanks to a central rotor which is externally controlled. Two permanent magnets are present at opposite edges of the sample holder so to generate a magnetic field parallel to substrate surface. This magnetic field is about 100 Oe and it is sufficient to induce magnetocrystalline anisotropy in the sputtered magnetic materials. The Ar pressure during deposition was usually kept at 6 mTorr by regulating the Ar flow with a mass flow controller. The voltage is applied to the magnetrons using four DC and one RF power generators, which allow to sputter up to five targets simultaneously. Therefore, complex multilayers can be deposited simply by rotating the sample holder below the targets while the magnetrons are functioning. The sputtering system also includes a load lock chamber which allows to reach the base pressure in less than one hour when loading a substrate. Hence, several samples can be processed per day. In the preload chamber two additional RF magnetrons are dedicated to non-conductive targets sputtering.

Table 2.1 summarizes the materials used in this research work, including relevant properties of the targets and sputtering parameters. Column two describes the crystal structure of the materials, which can be face-centered cubic (fcc) or body-centered cubic (bcc). Column three summarizes the magnetic ordering, namely antiferromagnetic (AF), ferromagnetic (F), diamagnetic (D) and paramagnetic (P). Note that $Ir_{25}Mn_{75}$ is the one target deposited with an RF magnetron. The growth rates are relatively high compared to other works using similar materials [Vopsaroiu, 2005]. This is mainly due to the small distance between the targets and the sample holder (approximately 4 cm).

Target	Crystal Structure	Magnetic Ordering	Magnetron Type	Pressure (mbar)	Power (W)	Growth Rate (nm/s)
$Ir_{25}Mn_{75}$	FCC	AF	RF	6	60	0.503
$Fe_{20}Ni_{80}$	BCC	F	DC	6	60	0.596
$Fe_{40}Co_{60}$	BCC	F	DC	6	60	0.562
Cu	FCC	D	DC	6	20	0.396
Ta	BCC	P	DC	6	50	0.579
Pt	FCC	P	DC	7	30	0.578

Table 2.1: Properties of the sputtering targets.

2.1.2 Optical lithography

Microlithography consists in transferring a geometric pattern to a resist by local exposure to an electron beam or ultraviolet light. The resist is a polymeric solution that reacts to electrons or photons of a particular wavelength. There are various types of resists with different properties. The exposure of a "positive" resist makes it soluble in a specific solution, called the developer. If a mask is placed between the exposure source and the resist, the pattern of the mask will be positively reproduced on the resist after the development. A "negative" resist instead is initially soluble in the developer and it is rendered insoluble by the exposure. Hence, the pattern of the mask will be negatively reproduced on the resist.

Firstly, the resist is uniformly distributed on the sample using a spin coater. Varying the spinning speed and the composition of the resist, one can control and reach a desirable thickness. Then the solvent present in the resist is evaporated through a prebake on a hotplate, typically at 90-160 °C for few minutes. Hence, the resist is exposed. The exposure time depends on the dose of the resist used and the technique employed. Finally, the time for development requires a cautious optimization based on the thickness of the resist, the exposure dose and the specific pattern dimensions and geometry.

The resolution of the patterning depends on the critical dimension which is proportional to the wavelength of the source of exposure. In optical lithography, the resist is exposed with photons and the critical dimension is therefore limited by the wavelength of the light source, which in our case is 350-450 nm (i.e. ultraviolet light). In e-beam lithography instead, a smaller critical dimension can be reached since the wavelength of the electron beam reaches sub nanometer values (about 5 pm at 50 kV). For further information about micro- and nanolithography refer to [Feldman, 2014]. The equipment used during this thesis work is a Karl Suss MJB3 which belongs to the ISOM-UPM. It uses a mercury lamp of 350 W and reaches a resolution of 0.6 μm.

2.2 Structural Characterization

The focal point of this research work is the low temperature crystallization of amorphous IrMn deposited by magnetron sputtering. The study of this phenomenon required a comprehensive structural characterization of the material, during the various phases of the crystallization. X-ray diffraction was firstly used to identify and study the process. This fast and non-invasive

technique allowed to analyze the evolution of the IrMn structure during the phase transition. Then, transmission electron microscopy was used to perform a deeper structural analysis of the specimens. The versatility of this technique allowed to characterize most of the aspects of this phenomenon, including the exact identification of the initial and final phases of the IrMn.

2.2.1 X-ray Diffraction

X-ray crystallography is an experimental technique used for studying the structural order of materials, based on the diffraction of X-rays by long range ordered atoms. The interactions between X-rays and atoms are dominated by the elastic scattering due to the electronic shells. According to the Huygens' principle, the scattered X-rays are spherical waves that propagate from the atoms toward all possible directions. If atoms are randomly positioned, e.g. in an amorphous material, the scattered X-rays will cancel out through destructive interference. In presence of some crystallinity, the atoms are long range ordered and the scattered X-rays may add constructively in few specific directions, determined by the Bragg's law

$$n\lambda = 2dsin\theta, \qquad (2.1)$$

where d is the lattice spacing of the crystal, θ is the incident angle, n is any integer, and λ is the wavelength of the incident X-rays. A schematic diagram of Bragg's diffraction is shown in figure 2.2a. For a comprehensive discussion about X-ray diffraction by crystals refer to [Cullity, 2014]. Structural characterization with an X-ray diffractometer consists in determining the lattice spacing d of a crystalline sample by using X-rays of known wavelength and measuring for which θ the Bragg's law is fulfilled. A schematic representation of an X-ray diffractometer (XRD) is shown in figure 2.2b. The XRD is mounted on a goniometer which allows both source and detector to rotate around the sample holder. Coherently with the Bragg's notation, the incident angle is θ and the diffraction angle with respect to the incident direction is 2θ. Note that when source and detector rotate at the same speed but in opposite directions, the Bragg plane is fixed with respect to the sample holder. On contrary, when they move at the same speed and in the same direction, the Bragg plane rotates with respect to the sample holder, while the Bragg angle is kept constant. The sample holder itself is mounted on a goniometer which grants six degrees of freedom. The relative angle ϖ is particularly important and describes the rotation of the sample holder around the diffractometer axis. The rotation around the out-of-plane axis is described by the angle φ, while ψ is the tilting angle. The beam source

is an X-ray tube, where highly energetic electrons are accelerated toward a metal target, which then emits X-rays according to the characteristic spectrum of the metal. The incident-beam optics consists of a series of slits which control the divergence angle and the spot size of the X-ray beam. A monochromator is often used to select one emission peak of the characteristic spectrum. The beam is directed to the sample at the center of the diffractometer and the diffracted signal is collected by the detector. The diffracted-beam optics may also include slits which limit the divergence of the entrance radiation, and an X-ray attenuator.

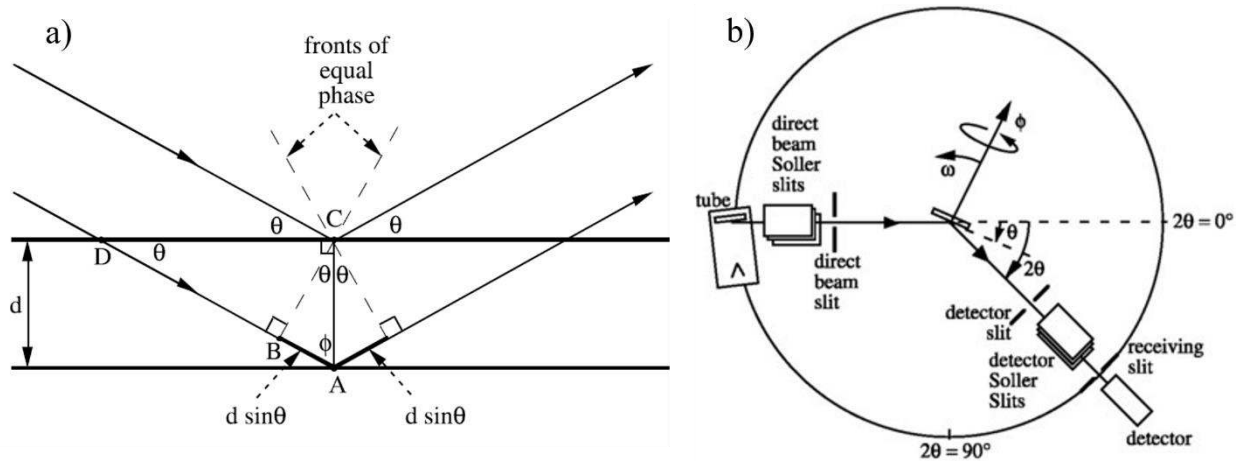

Figure 2.2: Schematic diagram of a) Bragg's diffraction and b) an X-ray diffractometer, after [Fultz, 2013].

XRD is a versatile technique which allows to perform structural characterization of thin films by various types of measurement. Here, only the ones relevant to the present work are discussed. Further details about XRD measurements can be found in [Cullity, 2014].

Out-of-plane $\theta/2\theta$ scan. This standard measurement for thin film characterization consists in rotating both source and detector at the same speed and in opposite directions, so to have a constant Bragg plane. If the system is aligned with the sample, the Bragg plane will be parallel to sample surface and the measurement will analyze the crystal texture in the out-of-plane direction. Note that in this configuration the irradiated volume diminishes as the incident angle increases. This type of measurement is suitable for very well out-of-plane textured samples.

Grazing Incident Angle (GID). This measurement consists in setting the source at a small incident angle, usually about 1 degree, and to perform a 2θ scan with the only detector. In this setup, the Bragg plane rotates as the detector moves and it is never parallel to the surface of the sample. Hence, the measurement is suitable for non-textured polycrystalline materials. In this case, the irradiated volume is constant during the whole scan since it only depends on the incident angle. Moreover, the low incident angle lead to a large irradiated volume and small

penetration depth, which makes this setup ideal for studying thin films [Guinebretière, 2007]. For these reasons, out-of-plane $\theta/2\theta$ scan and GID measurement give complementary information about the structure of materials.

In-plane $\varphi/2\theta_\chi$ scan. Another common setup for studying thin films consist in setting the source at a small incident angle, and to simultaneously rotate the sample and the detector around the out-of-plane axis, which therefore involve the angles φ and $2\theta_\chi$, maintaining the relation $2\theta_\chi = 2\varphi$ satisfied. In other words, the detector rotates two times faster than the sample, so to have a fixed Bragg plane exactly perpendicular to the sample surface.

Rocking curve. It consists in keeping both the source and the detector at fixed positions while "rocking" the sample holder by varying the angle ϖ. This way the system is set at a specific Bragg angle while the sample surface is rocked about the Bragg plane. The purpose of rocking measurements is to study the out-of-plane mosaicity of a crystalline phase, i.e. the misalignment between crystals with respect to the sample surface.

Pole-figure measurements. A pole figure is a stereographic projection that shows the orientation distribution of a specified crystallographic direction. The measurement consists in setting the system at a specific Bragg angle and mapping the diffraction signal on the hemisphere surface defined by the variation of the angles φ and ψ, by respectively 360° and 90°. Despite their long execution time, pole-figure measurements allow detailed texture analysis of thin films that other techniques cannot achieve.

The systems used for XRD measurements during this research work are a PANalytical X´pert Pro diffractometer of ISOM-UPM and a Rigaku SmartLab X-ray diffractometer of UoY. Both systems use a Cu target which emits $K\alpha 1$ and $K\alpha 2$ X-rays, whose wavelengths are 1.541 Å and 1.544 Å.

2.2.2 Transmission Electron Microscopy

A transmission electron microscope (TEM) [Knoll, 1932] takes advantage of the small de Broglie wavelength of electrons to achieve an imaging resolution that is forbidden to optical microscopy. In fact, in an optical microscope the wavelength of the light, which is 550 nm in case of green light, limits the resolution to about 200 nm. The de Broglie wavelength of electron is given by

$$\lambda = \frac{h}{mv}, \qquad (2.2)$$

where λ is wavelength, h is Planck's constant, m is the mass of the electron moving at a velocity v. For highly accelerated electrons the theoretical resolution reaches the sub atomic dimension. The principle of operation of a TEM is to expose an ultra-thin specimen with a highly energetic electron beam and to collect the transmitted electrons, which carry information about their interactions with the specimen.

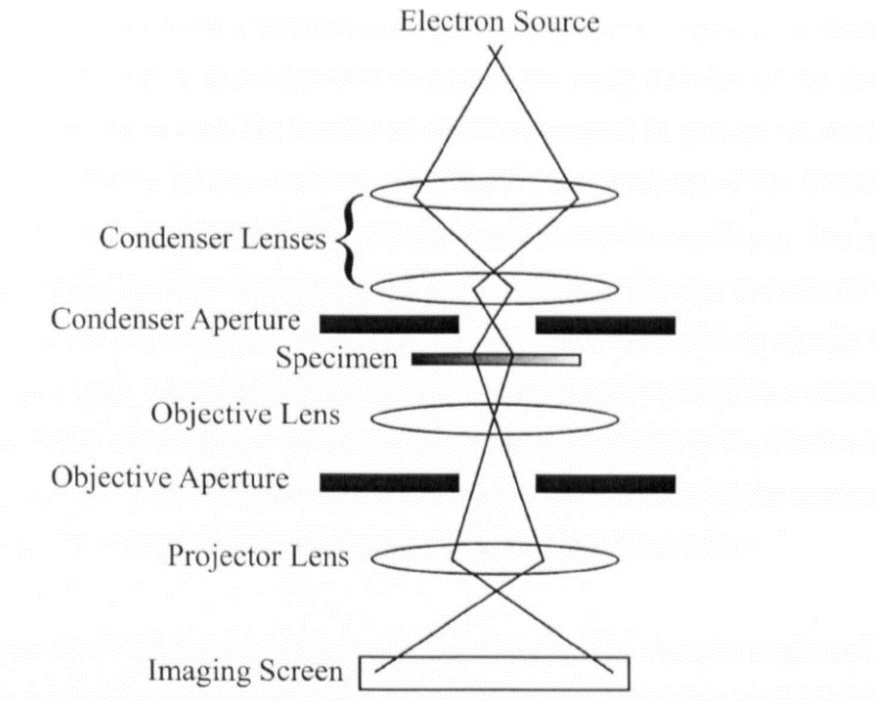

Figure 2.3: Schematic representation of the electrons path in a transmission electron microscope, after [Egerton, 2016].

Figure 2.3 shows a schematic diagram of the fundamental components of a TEM. To minimize interactions between electrons and air, the system is contained by a vacuum chamber, which is generally called "column" due to its cylindrical shape. At the top of the column there is an electron gun, whose emission source can be a tungsten filament or a lanthanum hexaboride (LaB_6) crystal. The source is held at high voltage (100-300 keV) and emits electrons by thermionic or field electron emission. The electrons are accelerated toward an anode, while a Wehnelt cylinder condenses the cloud of electrons into a beam. There are three sets of lenses and apertures in a TEM. The condenser set controls convergence, position and spot size of the electron beam before it reaches the specimen. The objective set includes a strong objective lens and an aperture located at the back-focal plane, where the diffraction pattern of the specimen is first produced. Finally, the projector set includes a series of intermediate lenses and a final

projector lens which control and magnify the beam onto the imaging device. The combination of condenser and objective lenses allows two operation modes. In standard mode, the electron beam is approximately parallel when reaches the sample and a continuous image of the irradiated area of the specimen is produced. In the scanning-mode (STEM) the electron beam is focused into a sub-nm probe, which allows atomic resolution and chemical analysis. Hence, the electron beam is scanned over the specimen by scanning coils and the image of the specimen is formed using the raster-scanning principle.

Contrast in TEM images is due to the interactions between the electrons and the specimen. A detailed kinematic description of these interactions can be found in [Egerton, 2016]. There are different types of imaging that can be performed with TEM. Here, we present only the ones relevant to this research work.

Conventional imaging. This is the basic TEM imaging. In this setup, the objective aperture is totally open, and the intermediate lenses project the image of the specimen on the detector. All the electrons, scattered and un-scattered, contribute to the image.

Selected area diffraction imaging. Selected area diffraction (SAD) imaging allows to study the diffraction properties of a specific zone of the specimen, by opportune tuning of the intermediate lenses which projects the back-focal plane onto the detector. In a SAD image, the un-scattered electrons contribute together to the bright central spot, while the scattered electrons produce a pattern, called the SAD pattern, which represents the diffraction properties of the specimen. The central spot is generally too bright for the CCD camera and it is often stopped with a small shutter. The study of the SAD pattern allows phase and texture analysis of the specimens.

Bright-field imaging. By selecting a particular area in the diffraction plane (SAD) with the objective aperture, one can change the contrast of the real image. In bright-field (BF) imaging, the objective aperture is set to select only the un-scattered electrons. The areas of the sample with a higher scattering probability will appear darker, giving rise to thickness and atomic-number contrast. Moreover, in presence of a polycrystalline specimen, the crystalline grains are likely to diffract the electrons and they will appear dark in the real image (figure 2.4a).

Dark-field Imaging. In dark-field (DF) imaging, the objective aperture is displaced horizontally so to select a particular area of the diffracted plane, admitting only electrons diffracted in that specific direction. Hence, the un-scattered electrons are filtered out, as well as the rest of the diffracted beam, leading to an overall dark real image where only the area of

the specimen which scatters in the selected direction appears bright (figure 2.4b). The DF imaging allows to highlight crystalline features and grains, and to determine where the contribution to the diffracted signal come from.

High-angle annular dark-field imaging. Most STEMs include a high-angle annular dark-field (HAADF) detector that collects electrons scattered through relatively large angles. Since the electron scattering is proportional to Z^2, where Z is the atomic number, the HAADF mode provides atomic-number contrast with atomic resolution. High resolution HAADF mode is extremely useful for phase analysis since it allows to determine the position of different elements in the unit cell.

Electron energy-loss spectrometry. Local chemical analysis can be achieved through electron energy-loss spectrometry (EELS). Energy losses of the transmitted electrons are caused by inelastic scattering such as plasmon and core electron excitations. Most STEMs include an EELS detector which analyzes the energy loss of transmitted electrons when working in HAADF mode. Information on local chemistry and structure is obtained from feature analysis of EELS spectra.

Energy dispersive X-ray spectrometry. When the thin specimen is traversed by the high-energy electrons of a TEM, the atoms will emit X-rays according to their characteristic spectrum. The X-ray spectrum is acquired by a solid-state detector and it is used to determine the concentrations of the different elements in the specimen.

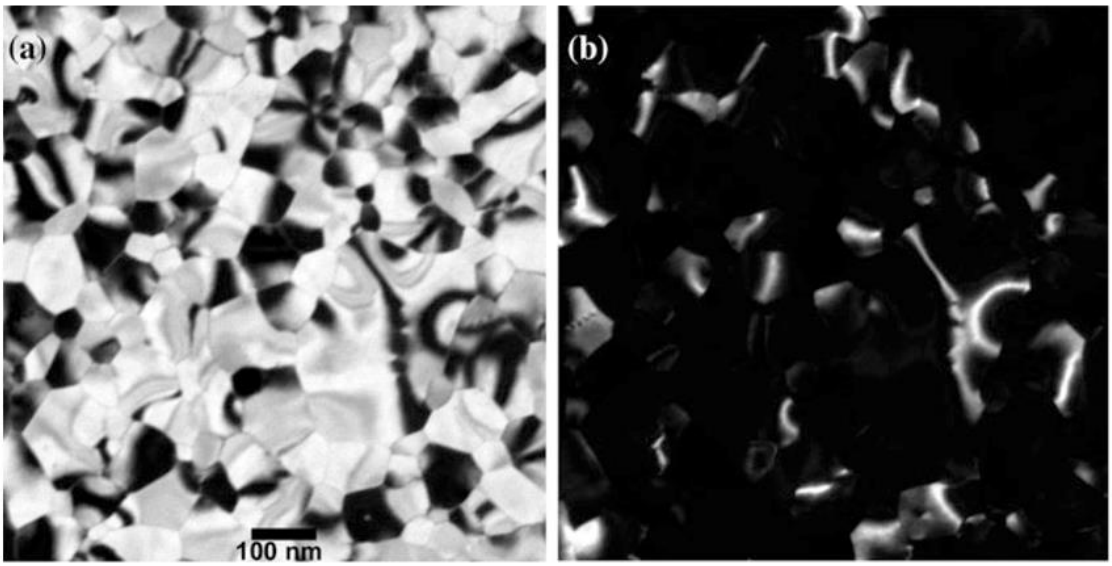

Figure 2.4: Examples of a) bright-field and b) dark-field TEM imaging of a polycrystalline specimen, after [Egerton, 2016].

TEM specimens must be thin enough to allow the transmission of most of the electron beam, i.e. usually about 100 nm thickness. This can be achieved in two configurations, namely plan-view and cross-section. In plan-view TEM imaging, the material is deposited directly onto a fine-mesh copper grid specifically designed for TEM measurements. Since the electron beam goes through the sample transversely, plan-view TEM imaging of multilayer samples overlaps the information from all the layers. This configuration has the advantage that it does not require any sample preparation and it permits to perform lateral grain size analysis and texture analysis of specimens made of few layers. On the other hand, in case of a multilayer the diffraction patterns of all the layers are overlapped and the structural analysis may result more complicated. Moreover, it must be noted that there might be structural differences between specimens deposited over substrates and TEM grids. Hence, additional comparative studies using other structural techniques may be required. Alternatively, the sample can be cut and analyzed laterally in the cross-section configuration. This type of measurement allows to study the sample layer by layer, but it requires a long sample preparation, which finally destroys the specimen. However, the amount of information that can be achieved by cross section TEM is substantially larger than in the case of plan-view imaging. For the samples produced in this research work, cross section TEM was necessary to achieve sufficient structural information.

The systems used for TEM and STEM measurements during this research work are a double-aberration-corrected field emission JEOL FS-2200 JEM TEM/STEM and a JEOL-2011 TEM (both operating at 200 kV) of the UoY.

2.3 Magnetic Characterization

In this research work, we analyzed the influence of the crystallization of IrMn on the exchange bias induced in a ferromagnetic material. In order to do so, a multi-technique magnetic characterization of the specimens was performed. The overall magnetic response of the samples was measured via vibrating sample magnetometry. This technique allowed to analyze the magnetic behavior during the crystallization of the IrMn. Then, local magnetic characterization of the samples was performed by magneto-optic Kerr microscopy and magnetic force microscopy.

2.3.1 Vibrating Sample Magnetometry

The Vibrating Sample Magnetometer (VSM) [Foner, 1959] is a versatile and highly sensitive instrument able to measure the magnetization of a sample as a function of an applied magnetic field. The principle of operation of a VSM is based on the Faraday's law of induction:

$$\mathcal{E} = -N\frac{d\Phi_B}{dt}, \qquad (2.3)$$

where $\mathcal{E}$ is the electromotive force induced in a coil of N turns, when it experiences a variation of the magnetic flux Φ_B with time t. In presence of a magnetic sample, the magnetic flux that the coil will experience is proportional to the magnetic moment of the sample. The principle of operation of a VSM is based on the observation of the voltage induced in a detection coil as the flux changes when the sample position oscillates.

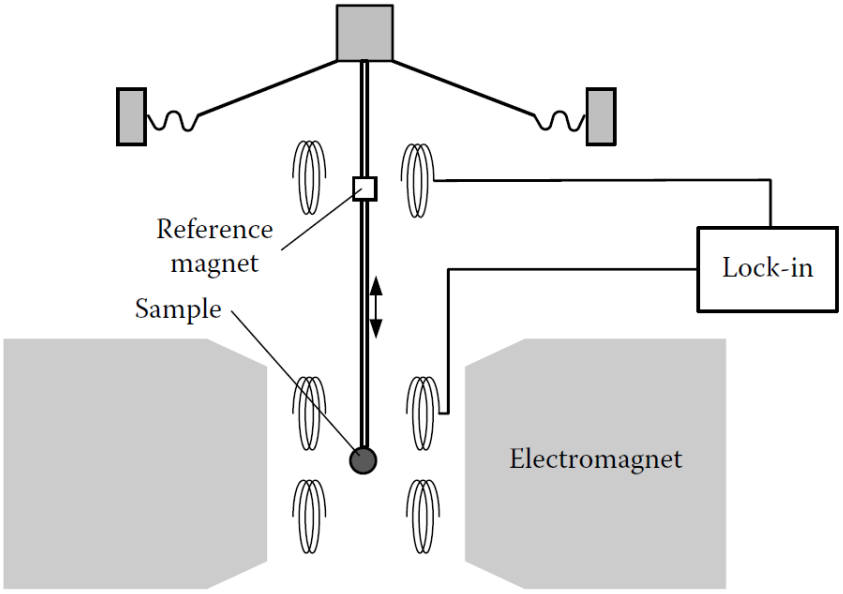

Figure 2.5: Schematic diagram of a VSM, after [Tumanski, 2011].

Figure 2.5 shows a schematic representation of a VSM. A uniform DC magnetic field is generated by a water-cooled electromagnet. Four detecting coils are locked to the poles of the electromagnet to avoid induced vibrations. The sample is placed at the extreme of a rod and positioned in the center of the field. The rod is non-magnetic, and it is connected to a vibrator head which generates a sinusoidal oscillation perpendicular to the magnetic field lines. The oscillation of the magnetic sample generates a field distortion and hence a change in the magnetic flux experienced by the detecting coils. The voltage output from the coils is processed

to extract a value of the magnetic moment of the sample. The rod can rotate freely, allowing to study in-plane anisotropies in different directions.

During the development of this research work three different systems were used. A LakeShore Model 7304 of the ISOM-UPM and a Lakeshore Model 4500 of the UoY were used for hysteresis loop measurements at room temperature. These instruments have a sensitivity of $5 \cdot 10^{-6}$ emu and can reach 14.5 kOe in standard configuration. A MicroSense Model 10 Vector magnetometer of the UoY was used for temperature dependent magnetic characterization. This system has a temperature range of 100 K to 770 K with a stability of 1 K, a sensitivity of $5 \cdot 10^{-6}$ emu and can reach 20 kOe.

2.3.2 Magneto-optic Kerr Microscopy

The principle of operation of a Kerr microscope is based on the magneto-optic Kerr effect (MOKE) [Kerr, 1877]. When light is reflected from a magnetized surface, both polarization and intensity change as a function of the magnetization of the surface. The magneto-optic Kerr effect can be described qualitatively using the concept of the Lorentz force acting on light-agitated electrons [Hubert, 1998]. Consider a linearly polarized light beam incident to a magnetized material (figure 2.6a). The interaction with the electric field of the light beam will induce the electrons to oscillate parallel to the plane of the polarization. Since the electrons are moving in presence of a magnetic field, they are subjected to the Lorentz force which induces a secondary motion proportional to

$$\boldsymbol{v}_{lor} = -\boldsymbol{m} \times \boldsymbol{E}, \qquad (2.4)$$

where $\boldsymbol{v}_{lor}$ is the velocity component due to the Lorentz force, $\boldsymbol{m}$ is the normalized magnetization and $\boldsymbol{E}$ is the electric field of the incident light beam. This secondary motion will generate secondary amplitudes according to the Huygens' principle, which results in an extra component of the reflected beam $\boldsymbol{R}_K$. The resulting polarization of the reflected beam is the superposition of the regular reflection component $\boldsymbol{R}_N$ and the Kerr component $\boldsymbol{R}_K$. Hence, the polarization of the reflected beam experiences a rotation which depends on the direction of the magnetization $\boldsymbol{m}$.

A magneto-optic Kerr microscope uses a polarizer to filter the reflected beam as a function of the direction of polarization. A schematic diagram of a high-resolution Kerr microscope is presented in figure 2.6b. The light beam is generated by a high-pressure mercury lamp and

corrected by a series of filters and lenses. The polarization of the incident light is selected with a polarizer filter. Then, the light beam passes through a strainless objective lens, reaches the sample surface and it is reflected through the same objective lens toward the analyzer. Because of the Kerr effect, the reflected beam polarization carries the information about the magnetic orientation of the sample surface. The changes in polarization are converted by the analyzer into light intensity contrast which are recorded by the detector. The sample holder is placed in a magnetic field generated by a water-cooled electromagnet. Different interchangeable electromagnets allow to choose the direction of the field with respect to the sample. The combination of the direction of the polarizers and the direction and intensity of the magnetic field allows the Kerr microscope to picture the magnetic domains oriented in different directions. For further details about the functioning and the possible configurations of a Kerr microscope refer to [Hubert, 1998].

In this research work magnetic characterization by Kerr microscopy was performed with an Evico Magnets Standard Kerr Microscope of IMDEA.

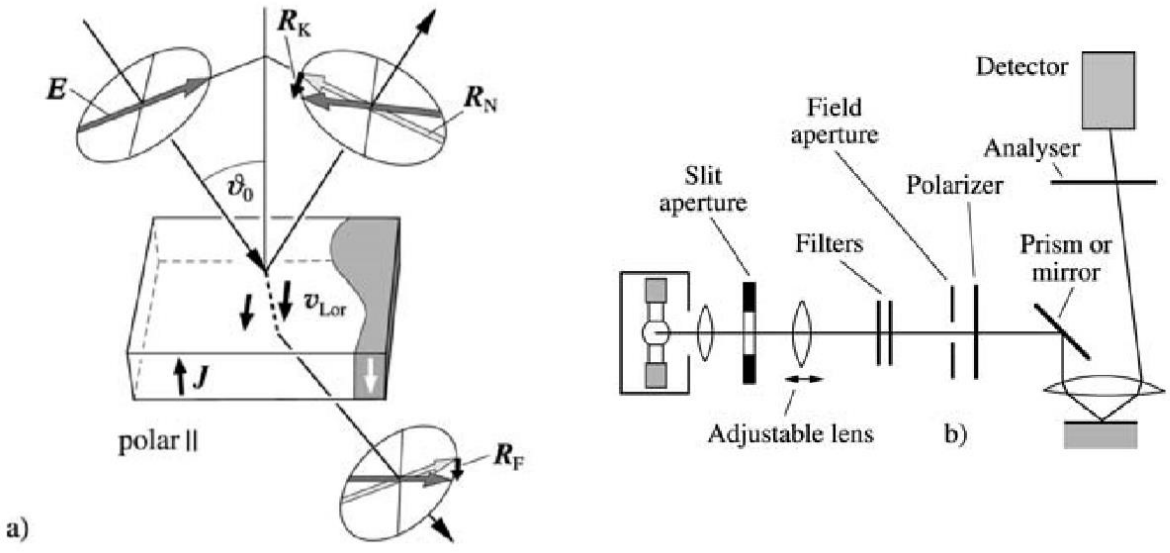

Figure 2.6: Schematic diagram of a) the magneto-optic Kerr effect and b) a magneto-optic Kerr microscope, after [Hubert, 1998].

2.3.3 Magnetic Force Microscopy

Force microscopy [Binnig, 1986] consists in studying the properties of a surface by measuring the forces acting on a sharp tip in the vicinity of the sample. The tip is usually mounted on the end of a cantilever, whose dynamic behavior is influenced by the tip-sample interactions.

Measuring static deflection of the cantilever or the change in its dynamic properties while scanning the tip over a sample allows to study its surface properties.

A schematic diagram of an atomic force microscope (AFM) is presented in figure 2.7a. The cantilever is generally made of single crystalline silicon. The tip is pyramidally shaped along the (100) direction and its dimension depends on the material used and the fabrication process. The resolution of an AFM critically depends on the tip radius, which should be as small as possible. A typical value of commercial silicon tips is 10 nm. A light beam is pointed toward the cantilever and the reflection is monitored by a position sensitive photodiode. When the tip approaches the sample surface, the forces involved bend the cantilever and the photodiode detects the variation in the reflected light beam. A four-segment photodiode is also capable to detect the torsion of the cantilever caused by lateral forces acting on the tip. In order to perform magnetic force microscopy (MFM), tips capable of interacting with magnetic forces are required. MFM tips are usually made of silicon and then covered with a thin layer of soft magnetic material, such as $Fe_{20}Ni_{80}$.

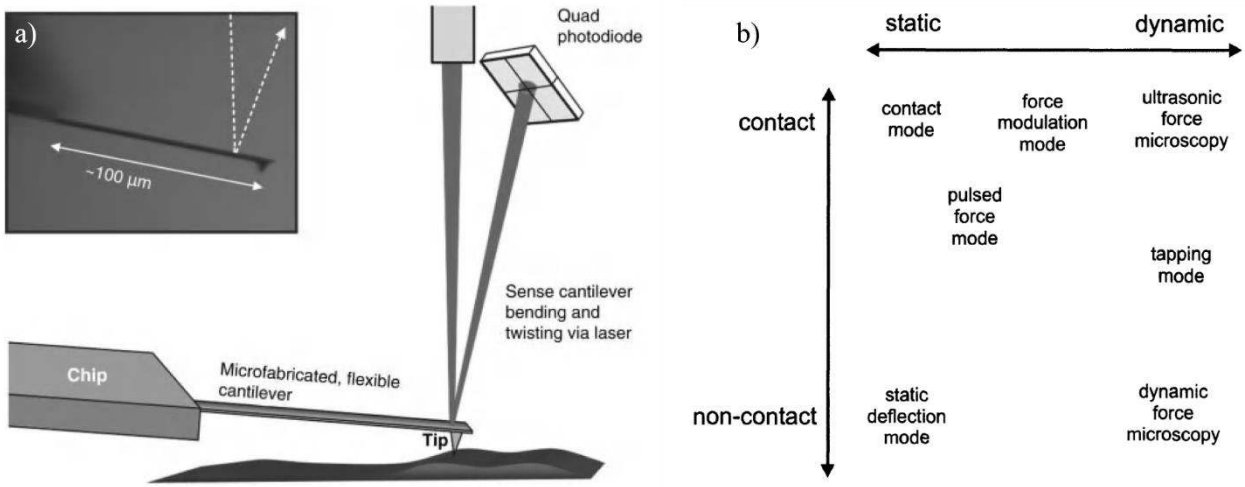

Figure 2.7: a) Schematic representation of an atomic force microscope, after [Haugstad, 2012]; b) AFM operation modes, after [Meyer, 2004].

A force microscope can operate in various modes, depending on the tip-sample distance, the dynamic of the cantilever and the feed-back parameter (figure 2.7b). In this research work the MFM measurements were taken in tapping mode. A detailed discussion about other operation modes can be found in [Meyer, 2004]. In tapping mode, the cantilever is made oscillate at constant frequency and the tip-sample distance is varied using the amplitude of the oscillation as the feedback parameter. Hence, the recorded tip-sample distance is proportional to the force experienced by the tip. The oscillation frequency is usually chosen to be the resonance

frequency of the cantilever. In tapping mode, the tip-sample distance is small enough that the tip is intermittently in contact with the sample, therefore the measurement is sensitive to topography-dependent forces. Note that at short tip-sample distance, the non-magnetic interactions become dominant over the magnetic ones, so the topography measurements are not affected by the magnetic field of the sample. Once the topography has been measured, the data is used to keep the tip-sample distance constant during a second scan of the same sample area. This way the topography-dependent forces are almost constant, and the amplitude variation of the oscillation depends mostly on tip-surface magnetic interactions. In a MFM this process is performed in a line-by-line mode. The tip scans the same sample locations twice, once to measure the topography and a second time to map the magnetic forces with the tip lifted off. Tip-surface distance for magnetic measurements usually range from 20 nm to 200 nm. In this research work magnetic characterization by MFM was performed at ISOM-UPM and at ICMM.

Chapter 3: Structural Characterization

The study of the spontaneous crystallization of IrMn described in this work required an accurate and extensive structural analysis, via multiple characterization techniques. The main issues discussed in this chapter include the characterization of a series of structural properties of the sputtered IrMn, such as the initial and final crystalline phases, the nature of the phase transition, the crystallographic texture and the AF/F interface roughness, as well as the analysis of structural defects and exact stoichiometry of deposited materials. The chapter is organized in four sections. The first section includes fundamental information about the structural properties of IrMn, according to the scientific works published in the last 60 years. In the second section, structural studies performed by X-ray diffraction (XRD) are presented. A thorough analysis of the samples was performed via a variety of measurements, namely out-of-plane $\theta/2\theta$ scans, in-plane $\varphi/2\theta_\chi$ scans, ω scans (rocking curve) and pole figure scans. The third section covers the structural characterization by transmission electron microscopy (TEM). Again, a variety of measurements were performed, which includes plan-view TEM, cross-section TEM and atomic-resolution scanning TEM. The last section summarizes the main results of the extensive structural characterization performed in this work.

3.1 Structural properties of IrMn

In polycrystalline exchange biased bilayers, the quality of the exchange bias (EB) depends mostly on the microstructural properties of the antiferromagnetic (AF) layer, such as grain size, crystallographic structure and texture, structural defects and interface roughness [O'Grady, 2010]. Since the introduction of IrMn as an AF material for EB in 1996 [Hoshino, 1996], the dependence of the magnetic properties of exchange biased bilayers on the crystalline structure of the IrMn has been object of many studies. At first, the attention was focused on the variation of the exchange bias field with the exact composition of the IrMn. Both Hoshino et al. and Fuke et al. showed that the maximum value for the exchange bias is obtained at around 20 at. %-Ir concentration [Hoshino, 1996; Fuke, 1997]. Similarly, Tsunoda et al. confirmed that the unidirectional anisotropy constant J_k reaches a maximum in the range of 22-32 at. %-Ir [Tsunoda, 2006]. Hence, this compositional range for IrMn has been taken as the standard composition for both research and technological applications based on exchange bias.

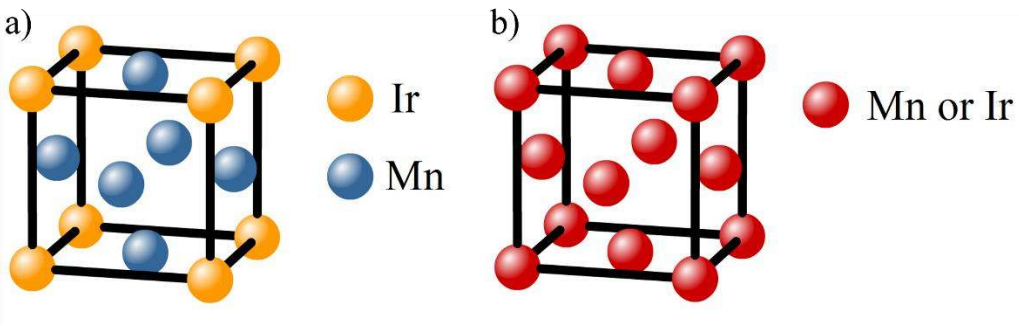

Figure 3.1: Schematic representation of the atomic structure of a) $L1_2$-phase and b) γ-phase of IrMn.

A detailed phase diagram of IrMn as a function of the Mn concentration was outlined in 1955 by Raub et al. [Raub, 1955]. In the range of interest, which is around 25 at. %-Ir concentration, IrMn can assume two crystallographic phases, i.e. chemically-disordered γ-phase and chemically-ordered $L1_2$-phase. A schematic diagram of the two atomic structures is presented in figure 3.1. The γ-phase of IrMn is face centered cubic (fcc), in which Ir and Mn atoms do not have definite lattice-site preferences (figure 3.1b). In the $L1_2$-phase instead, Mn atoms occupy the face-central positions (figure 3.1a), assuming a Cu_3Au-type atomic-ordering. Detailed crystallographic information about the two phases is summarized in table 3.1.

In 1974, Yamaoka et al. studied the magnetic character of Ir_xMn_{1-x} ($0.05 < x < 035$) as a function of Ir concentration and crystallographic structure, by magnetic susceptibility and X-ray diffraction measurements [Yamaoka, 1974]. As can be seen in figure 3.2, which reproduces the magnetic phase diagram elaborated by Yamaoka et al., both phases of IrMn are antiferromagnetic, with the ordered $L1_2$-phase having a higher Néel temperature, T_N. On the other hand, Kohn et al. showed, by studying IrMn/Fe bilayers deposited by molecular beam epitaxy, that the exchange bias induced by the two phases of IrMn has different characteristics, which depend largely on the crystallographic structure of the IrMn itself [Kohn, 2013].

Phase Name	**Crystal Family**	**Bravais lattice**	**Space Group symbol**	**Space Group number**	**Strukturbericht symbol**	**Phase Prototype**	**Lattice constant (nm)**
γ-IrMn	Cubic	Face-centered	$Fm\bar{3}m$	225	A1	Cu	0.378
$L1_2$-$IrMn_3$	Cubic	Primitive	$Pm\bar{3}m$	221	$L1_2$	Cu_3Au	0.3772

Table 3.1: Crystallographic information about the two phases of IrMn at around 25 at. %-Ir concentration [Kohn, 2013].

Tsunoda et al. studied the structural properties of IrMn grown by magnetron sputtering, as a function of the substrate temperature during the deposition. They showed that deposition of IrMn in standard conditions, i.e. at room temperature, generally leads to polycrystalline disordered γ-phase [Tsunoda, 2006]. They also managed to promote the formation of the ordered $L1_2$-$IrMn_3$ phase, by increasing the substrate temperature up to 520 K during the deposition of the IrMn layer. Another way to induce the formation of the $L1_2$ ordered phase is by annealing alloys with at least 20 at. %-Ir concentration at temperatures of about 1000 K, as observed by Yamaoka et al. and Raub et al. [Yamaoka, 1974; Raub, 1955]. However, such a high temperature annealing is not viable from a technological point of view. In fact, IrMn alloys are mainly employed in thin film multilayers, such as spin valves, and the effects of interdiffusion of Mn at temperatures higher than 570 K are detrimental for technological performances [Samant, 2000; Cardoso, 2000; Yoo, 2002].

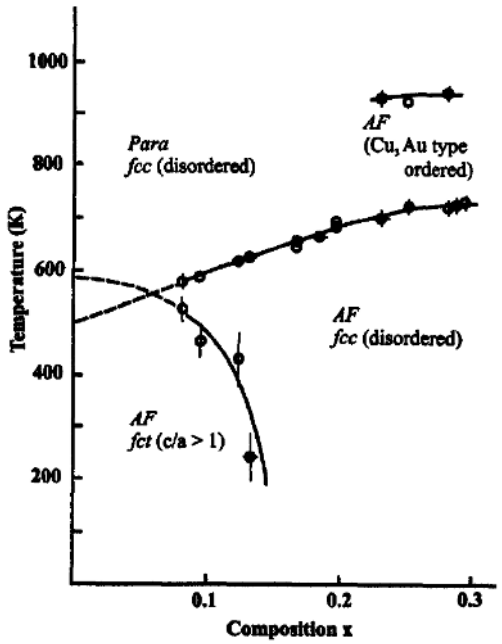

Figure 3.2: Magnetic phase diagram of Ir_xMn_{1-x} as a function of Ir concentration, after [Yamaoka, 1974].

When dealing with the structural characterization of IrMn, it is important to note that the lattice constant of the two phases is nearly the same, as shown in table 3.1. Therefore, the exact phase identification of deposited IrMn is not trivial. However, the main structural difference of the two phases, consisting in the Mn positioning, influences directly the diffraction properties of the material. In fact, in the disordered γ-phase, diffraction is allowed only for some lattice plane families. This is due to the random position of Ir and Mn atoms in the fcc cell. In ordered $L1_2$-phase, instead, the "superlattice" atomic-ordering allows the diffraction for those lattice plane

families forbidden in the γ-phase. Hence, the identification of the two phases can be achieved through diffractometry measurements, by verifying the absence or presence of these additional superlattice diffraction reflections, which are the result of the perfect atomic-ordering of $L1_2$-phase. In this work, such a characterization was performed by X-ray diffractometry and TEM diffraction analysis.

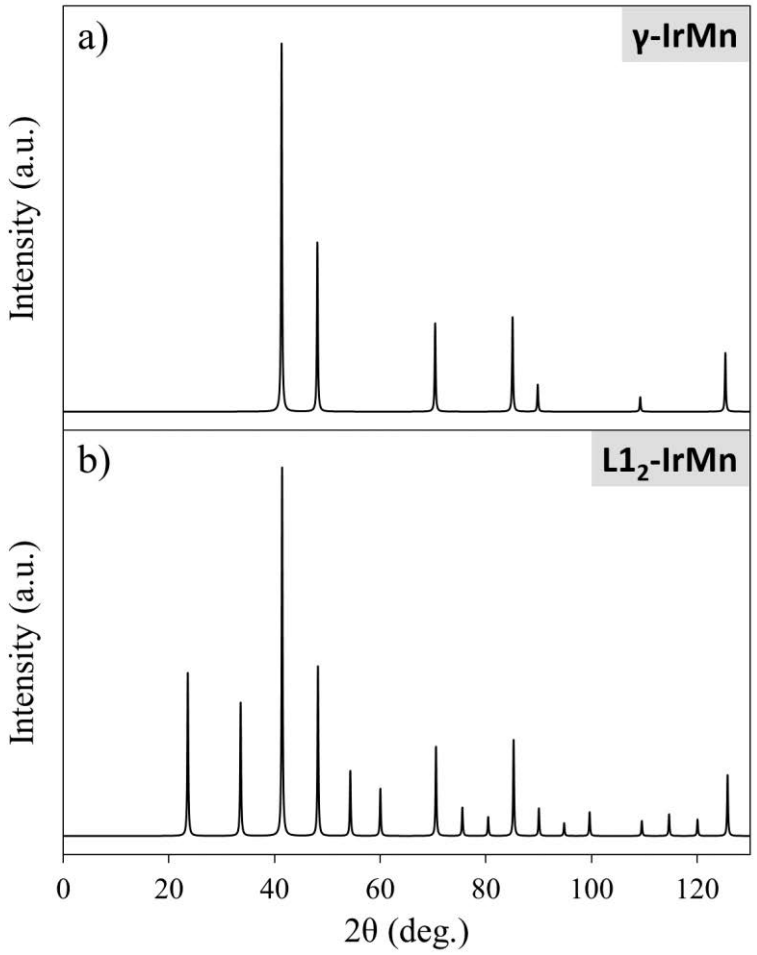

Figure 3.3: Calculated X-ray powder diffractograms of a) γ-phase and b) $L1_2$-phase of IrMn.

The X-ray powder diffractograms of the two phases of IrMn, theoretically calculated from their crystallographic structures, are presented in figure 3.3. The wavelength of a Cu *Kα* radiation source was employed for the calculation. It can be observed that the $L1_2$-phase has a much richer diffractogram than the γ-phase. In fact, the comparison between the two diffractograms shows that $L1_2$-IrMn generates several additional peaks, which are the result of the superlattice reflections due to the Mn ordering. Thus, phase identification of IrMn by XRD can be achieved by verifying the presence of the superlattice reflections of ordered $L1_2$-IrMn. However, in case of sputtered materials the phase identification is not trivial. In fact, the diffractograms presented in figure 3.3 are theoretically calculated for powder samples, which consists of a large number

of randomly oriented grains, where all possible reflections are present in a single scan. Polycrystalline thin films, instead, are often textured, i.e. the crystalline grains tend to align in the same direction. In such samples, the superlattice reflections are unlikely to be visible with standard scans and proper structural characterization requires advanced knowledge of both the material structure and the XRD technique. Imakita et al. and Tsunoda et al. showed that cautious characterization by XRD can lead to phase identification of sputtered IrMn or, in case of both phases present in the sample, to quantitative evaluation of the degree of order of the material [Imakita, 2004; Imakita, 2005; Tsunoda, 2006].

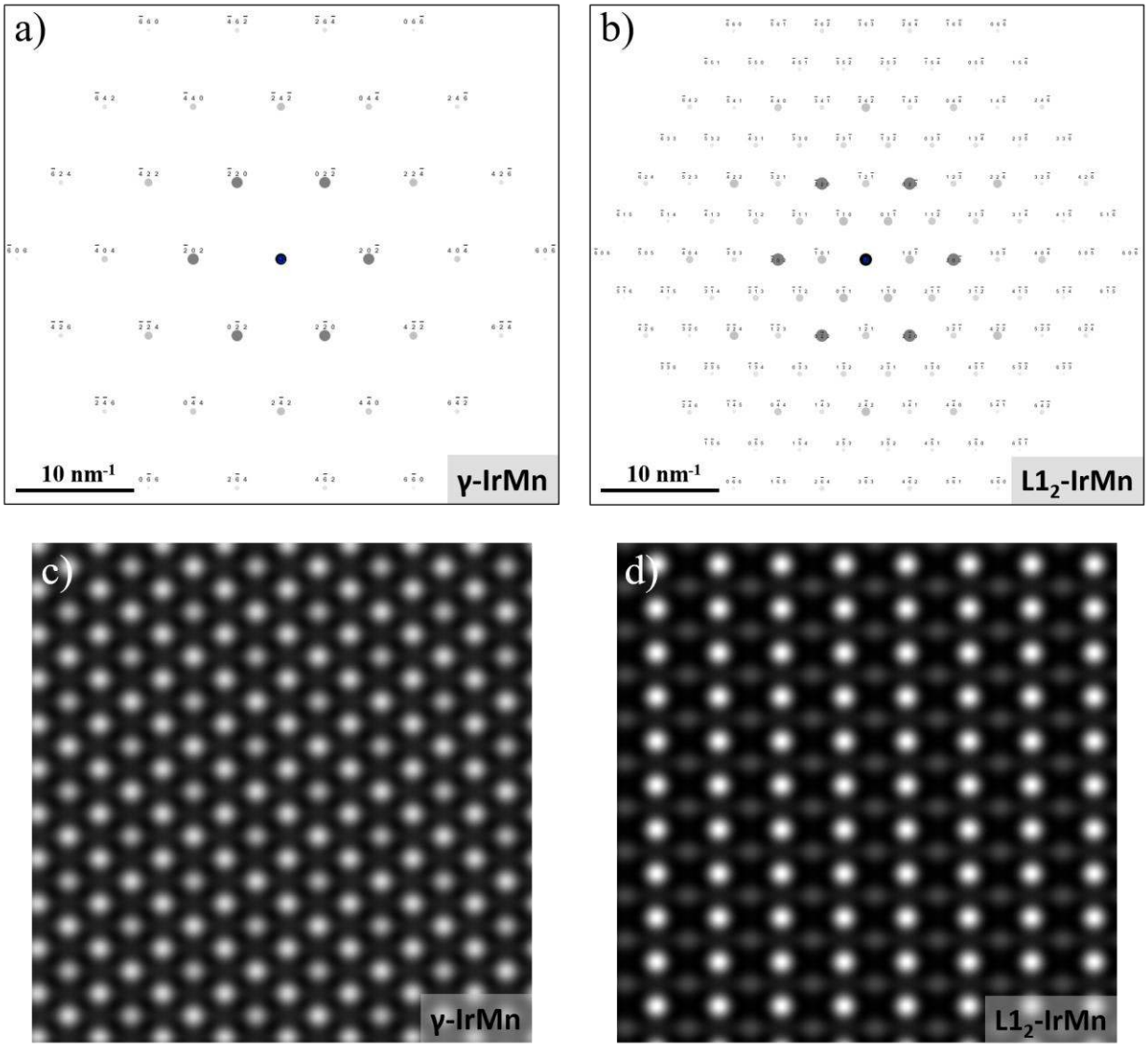

Figure 3.4: Calculated TEM diffraction patterns of a) γ-phase and b) $L1_2$-phase of IrMn in the (111) zone axis; calculated HAADF-STEM images of c) γ-phase and d) $L1_2$-phase of IrMn in the (110) zone axis [JEMS-SAAS software].

The same superlattice diffraction signal can be detected by transmission electron microscopy. For illustration purposes, figure 3.4 shows the simulated diffraction pattern of the two phases of IrMn in the (111) zone axis (i.e. the view is parallel to the (111) lattice plane). In the same view range, the γ-phase generates 36 reflections against the 126 reflections of the $L1_2$-phase, 90 of which being superlattice reflections due to the perfect Mn-ordering. Once again, phase identification is achieved by checking the presence of the additional reflections of the ordered $L1_2$-phase. In addition to the TEM diffraction analysis, one can determine the phase of IrMn by high-angle annular dark-field (HAADF) imaging with a scanning transmission electron microscope (STEM). This imaging technique permits to reach atomic resolution and provides elemental contrast, which consequently allows to distinguish between Ir and Mn atoms. If the material is in the disordered γ-phase, the atoms will be randomly positioned and the HAADF image will show no atomic contrast (figure 3.4c). In presence of the $L1_2$-phase, instead, the image will show a periodic contrast given by the alignment of the lighter or the heavier atoms (figure 3.4d). Both TEM diffraction analysis and HAADF-STEM imaging were used by Kohn et al. to successfully distinguish between the two phases of IrMn [Kohn, 2013].

3.2 X-ray Diffraction measurements

The extensive structural study of the spontaneous crystallization of IrMn presented here, required a thorough characterization by X-ray diffraction technique of 15-nm-thick films of IrMn deposited by magnetron sputtering. This section summarizes the results of this structural analysis by presenting and discussing the most relevant XRD measurements. The first three subsections are part of a detailed XRD study performed on IrMn/FeCo bilayers, which are commonly used in magneto-resistive devices. The first subsection covers the structural transformation of the IrMn by presenting out-of-plane $\theta/2\theta$ and grazing incident diffraction scans. In the second subsection, a study of the mosaicity of the IrMn layer is performed via rocking curve and pole figure measurements. In the third subsection, the identification of the crystallographic phase assumed by the crystallized IrMn is achieved by the analysis of in-plane $\varphi/2\theta_\chi$ scans, which also led to grain size considerations through the employment of the Scherrer equation. The fourth and final subsection includes relevant results concerning samples with different structures, i.e. without the FeCo layer or the seed layer.

3.2.1 Spontaneous structural transformation in IrMn

Out-of-plane $\theta/2\theta$ scan

Samples with structure SL/IrMn(15nm)/FeCo(5nm)/CL (AF/F-type) were deposited over Si/SiO_2 substrates by magnetron sputtering, for structural characterization purposes. A 3.5-nm-thick Ta seed layer (SL) was used to promote the (111) texture in the IrMn layer, according to the study performed by van Driel et al. [van Driel, 2000]. The capping layer (CL) used was either Cu(7nm)/Pt(1.5nm) or Ta(5nm), depending on the measurements to be performed on the sample. After deposition, the sample was immediately taken to the X-ray diffractometer to perform out-of-plane $\theta/2\theta$ scans. In the first measurement, which was taken within one hour after deposition, no diffraction peaks were observed, besides the ones associated with the crystalline Si substrate. In order to detect structural changes in the IrMn layer, out-of-plane $\theta/2\theta$ scans were repeated periodically every 1.5 hours, around the nominal position of the IrMn (111) peak. The sample was always kept at room temperature during and between measurements. The measured XRD scans are presented as a cascade plot in figure 3.5. The first scan, i.e. the black diffractogram in figure 3.5, shows a flat response which indicates the absence of any IrMn (111) diffraction signal. In the following measurements, the periodic scans show the progressive formation of a diffraction peak at the angle $2\theta = 41.2°$. It is interesting to note that, although most of the peak formation happens during the first 12 hours, as shown by the light blue diffractogram in figure 3.5, a slight but noticeable increase of the peak intensity takes place during the following two days. The angular position of the peak, which is constant during the whole formation, corresponds to the IrMn (111) reflection, whose nominal value is $2\theta_{(111)} = 41.336°$ [Kohn, 2013]. Using the Bragg's law (equation 2.1) introduced in section 2.2.1, the interplanar spacing of the IrMn can be calculated, giving a $d = 2.189$ Å. Hence, the lattice constant a can be derived using the formula for cubic crystals

$$\frac{1}{d^2} = \frac{h^2 + k^2 + l^2}{a^2}$$

where h, k and l are the Miller indices of the plane considered [Cullity, 2014]. This leads to $a = 3.792$ Å, which is 0.31% bigger than the nominal lattice constant $a_{IrMn} = 3.78$ Å [Kohn, 2013]. Note that such a small discrepancy might be due to instrumental offset or misalignment and/or to material strain.

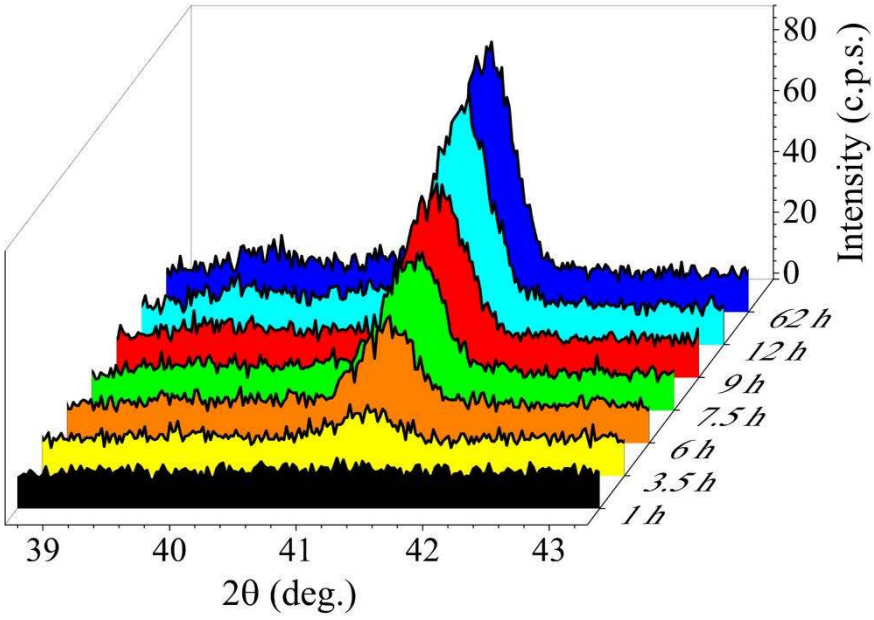

Figure 3.5: XRD out-of-plane $\theta/2\theta$ scans around the position of the IrMn (111) reflection during the structural transformation of IrMn.

An indication of the nature of this structural transformation can be retrieved by observing that only the intensity of the (111) reflection increases during the peak formation, whereas its shape and position are constant. Considering that the out-of-plane $\theta/2\theta$ scan is sensitive only to crystalline planes parallel to the sample surface, the increase in the intensity of a diffraction peak can be explained with two different structural changes, i.e. texture enhancement or crystallinity enhancement. Texture enhancement consists in a partial reorientation of crystalline grains, which tends to align a specific crystalline plane with the sample surface. If this was the case, the as-deposited material should initially be polycrystalline with grains randomly oriented, so that the absence of texture would lead to a flat response in the out-of-plane $\theta/2\theta$ scan. Afterwards, the grains would spontaneously reorient themselves aligning their (111) planes with the sample surface, which would explain the (111) peak formation. Crystallinity enhancement, instead, consists in a structural transformation of the material which improves its crystal order. If this was the case, the as-deposited material should be in a disordered phase which would not produce X-ray diffraction. Then, when the structural transformation triggers, the atoms progressively diffuse to their crystalline positions, promoting the (111) texture, which cause the diffracted signal to increase until the process is complete. The aim of the following structural characterization is to discriminate between these two possibilities.

Grazing Incident Diffraction

In order to distinguish between texture or crystallinity enhancement, a more detailed structural characterization was performed on a newly deposited sample, with the same structure. The structural study consisted in alternating out-of-plane $\theta/2\theta$ scans and grazing incident diffraction (GID) scans, during the structural transformation of the IrMn. GID scans are particularly suitable for studying non-textured polycrystalline thin films, since at low incident angles the large irradiated volume allows to detect the diffracted signal from randomly disordered grains [Guinebretière, 2007]. Figure 3.6 shows the diffractograms taken at an early stage (black curves) and once the structural transformation is complete (red curves). The out-of-plane $\theta/2\theta$ scans of figure 3.6a reveal the same formation of the IrMn (111) peak at $2\theta = 41.2°$ detected in the previous sample. The GID scans presented here were taken with an incident angle $\alpha = 0.5°$. The black diffractogram of figure 3.6b shows a peak at $2\theta = 41.37°$ and a less intense one at $2\theta = 70.37°$. As time passes, the intensity of the former peak decreases progressively until the peak eventually disappears. Concurrently, the latter peak grows in intensity, in parallel with the (111) peak of the $\theta/2\theta$ scan.

The analysis of these data reveals that the peak at $2\theta = 41.37°$ corresponds to the IrMn (111) reflection and it is due to randomly oriented grains which are present in the as-deposited material. As time passes, these grains experience reorientation and align their (111) planes with the sample surface, hence the diffraction peak decreases in the GID scans. The peak at $2\theta = 70.37°$ corresponds to the IrMn (220) reflection whose nominal value is $2\theta_{(220)} = 70.39°$ [Kohn, 2013]. Contrarily to the (111) peak in the GID scan, the IrMn (220) peak is not due to randomly oriented grains. In fact, the relative angle between the two lattice plane families allows to observe the (220) peak in the GID scan when the material is strongly (111) textured [Aley, 2008; Tsunoda, 2006]. Hence, the evolution of the (220) reflection is a consequence of the formation of the (111) peak in the out-of-plane $\theta/2\theta$ scan. In addition to these two diffraction signals from the IrMn, a further broad peak can be observed at $2\theta = 39°$ in the red diffractogram of figure 3.6b, which is likely to correspond to the (110) reflection from the Ta layers. Such a broad peak suggests that the deposited Ta is amorphous. Finally, no diffraction signal from FeCo is observed, probably due to the limited thickness of the FeCo layer. In conclusion, the GID scans indicate that some IrMn grains experience reorientation, which implies some texture enhancement during the structural transformation. However, the low

intensity of the initial (111) peak in the GID scan suggests that this reorientation is not sufficient to explain the structural change detected in the out-of-plane $\theta/2\theta$ scans.

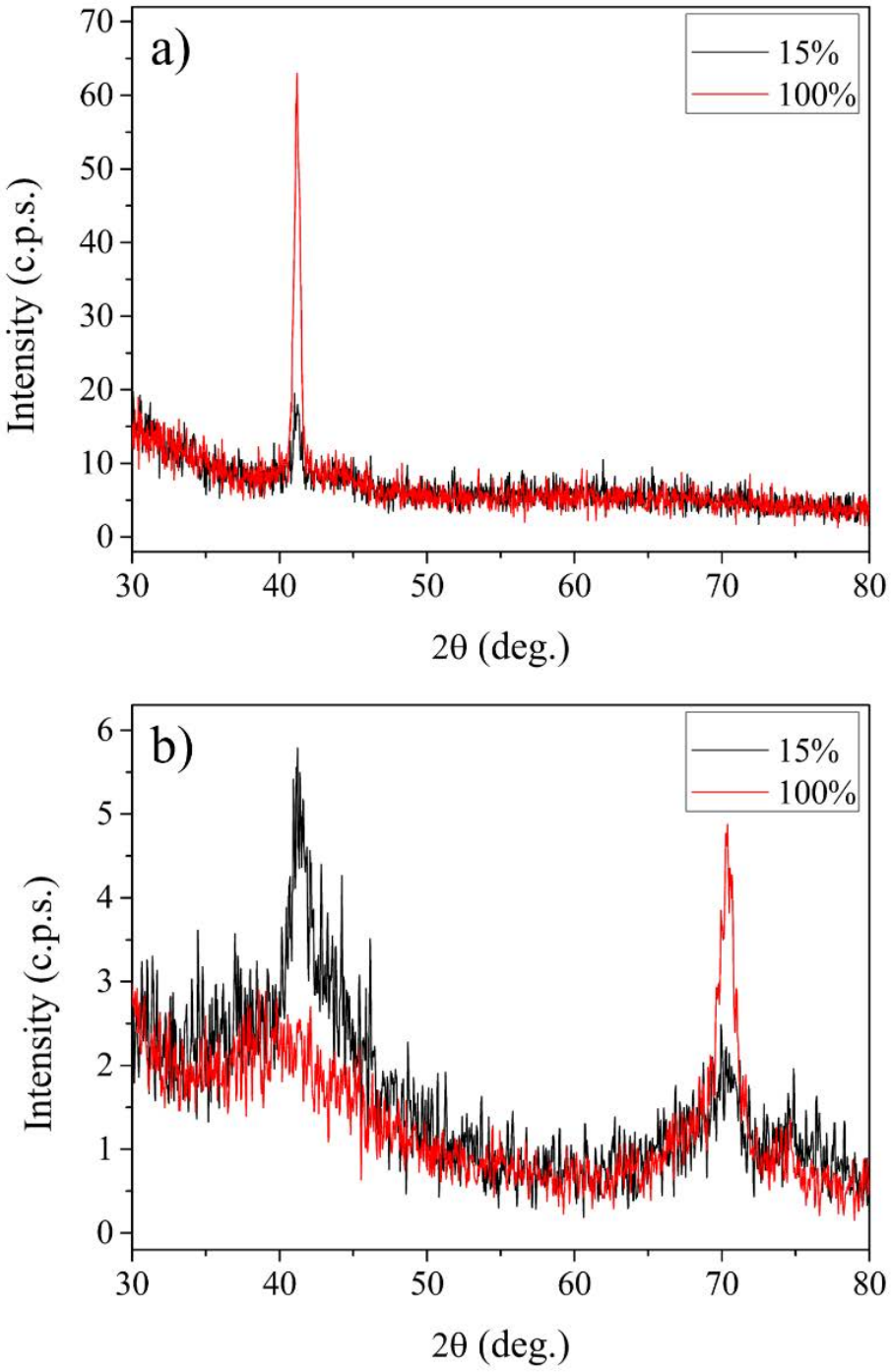

Figure 3.6: XRD a) out-of-plane $\theta/2\theta$ scans and b) GID scans taken at different stages of the structural change experienced by the IrMn.

3.2.2 Texture analysis and Mosaicity

Rocking curve

In order to clarify the nature of the structural change, a study of the mosaicity of the IrMn layer was performed via rocking curve measurements. A rocking curve consists in measuring the intensity of a given diffraction peak, i.e. at a fixed Bragg condition, as a function of rotation ("rocking") ω of the sample. This way, the scan detects the out-of-plane texture dispersion of the grains, which is called out-of-plane mosaicity. The evaluation of the full width at half maximum (FWHM) of a rocking curve indicates the average misalignment of textured grains with the sample surface.

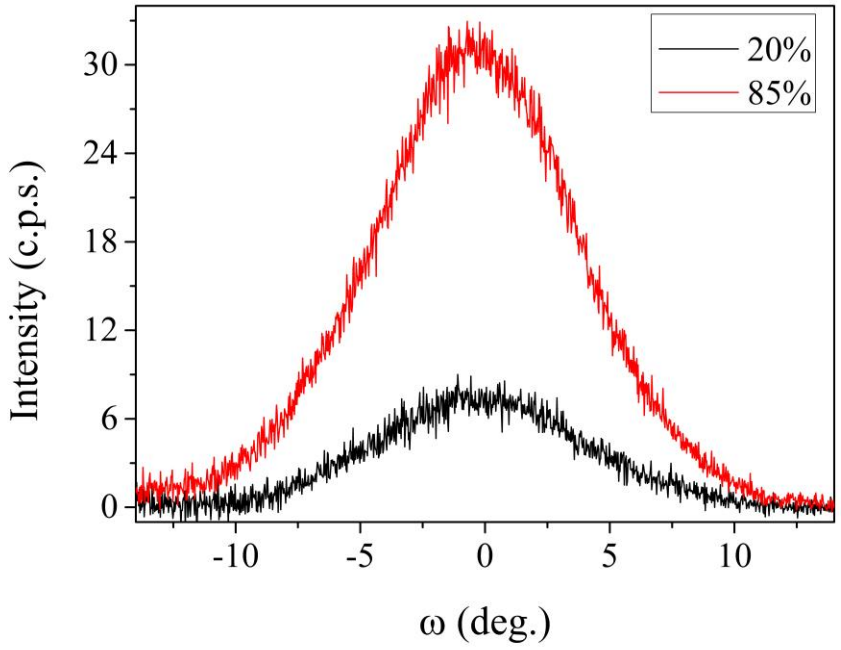

Figure 3.7: XRD ω scans (rocking curves) of the IrMn (111) reflection, taken at different stages of the structural transformation in the IrMn.

Figure 3.7 shows two rocking curves of the IrMn (111) reflection, taken at different stages of the peak formation shown in figure 3.5. For the sake of clarity, in figure 3.7 the background was subtracted from the measured data. Both rocking curves are centered in zero, which confirms the good alignment of the (111) lattice plane with the sample surface. The FWHM is about 9.4° for both curves, which indicates a relatively large texture dispersion of the IrMn (111) reflection. Figure 3.7 also shows that the evolution of the rocking curve consists in an overall increase of its intensity, rather than a change of its shape. The fact that the FWHM is essentially constant with time rules out the possibility of texture enhancement. In fact, it shows

that the reorientation of IrMn grains detected in the GID scans (figure 3.6b) only plays a minor role in the structural transformation. This confirms that the structural change experienced by the IrMn is a phase transformation which improves the crystallinity of the material. The almost total absence of any sign of crystallinity in the as-deposited material suggests that the IrMn layer is initially in a metastable nanocrystalline or amorphous phase, and then it experiences a spontaneous crystallization at room temperature, which progressively enhances the diffraction response from the material.

Pole figure

A more detailed analysis of texture and mosaicity of a few samples was achieved by performing pole figure measurements. A pole figure consists in mapping the diffraction signal intensity at a specific diffraction condition, i.e. at fixed Bragg angle, on the hemisphere surface defined by the variation of the angles φ and ψ, by respectively 360° and 90°. Figure 3.8 shows two pole figures for an IrMn/FeCo bilayer deposited over a Si(111)/SiO_2 substrate. The measurements were taken at fixed $2\theta = 41.2°$ and $2\theta = 69.95°$, which correspond respectively to the IrMn (111) and (220) reflections (figure 3.8a and 3.8b). A schematic representation of the theoretically calculated pole figure for (111) and (220) reflections of a (111) textured fcc perfect crystal is shown in figure 3.8c and 3.8d.

In an fcc crystal, there are four sets of planes of the form {111}, which have the same interplanar spacing but different orientation. A pole figure shows both the orientation of all these planes, which is defined by the texture and the geometry of the crystal, and their diffraction intensity. In a perfect crystal, these reflections appear as small dots at well-defined positions, as represented in the diagrams of figure 3.8. The central spot corresponds to the direction perpendicular to the sample surface, and therefore it defines the texture of the material. In polycrystalline samples, variations from perfect crystallinity, such as out-of-plane and in-plane mosaicity, can be analyzed by pole figure representation. In figure 3.8a, the (111) pole figure shows a broad central spot, which confirms the (111) texture and the large out-of-plane mosaicity detected in the rocking measurements. In addition, it shows a bright uniform ring at $\psi = 70.5°$ due to the other three (111) planes. The fact that the signal from these planes forms a ring instead of three separated spots implies that the crystals are randomly oriented in the angle φ, which is an indication of large in-plane mosaicity.

On the other hand, a perfect (111) textured fcc crystal have three sets of planes of the family {220} located at $\psi = 35.3°$ and six ones located at $\psi = 90°$, as shown in figure 3.8d. The

(220) pole figure (3.8b) shows less intense diffraction signal, which agrees with the fact that the intensity of the (220) reflection is more than ten times lower compared to the (111) diffraction peak. The in-plane random orientation of the crystals is confirmed, as the two sets of {220} reflections at $\psi = 35.3°$ and $\psi = 90°$ produce uniform annular signals instead of single dots. The three bright dots which appear in figure 3.8b correspond to the three Si (400) sets of planes, which have a nominal Bragg angle of $2\theta = 69.15°$ and lay at $\psi = 54.7°$ in Si(111). In conclusion, the texture analysis reveals that the samples are well textured, with a rather large out-of-plane mosaicity of about 9°, and a total in-plane mosaicity of 360°.

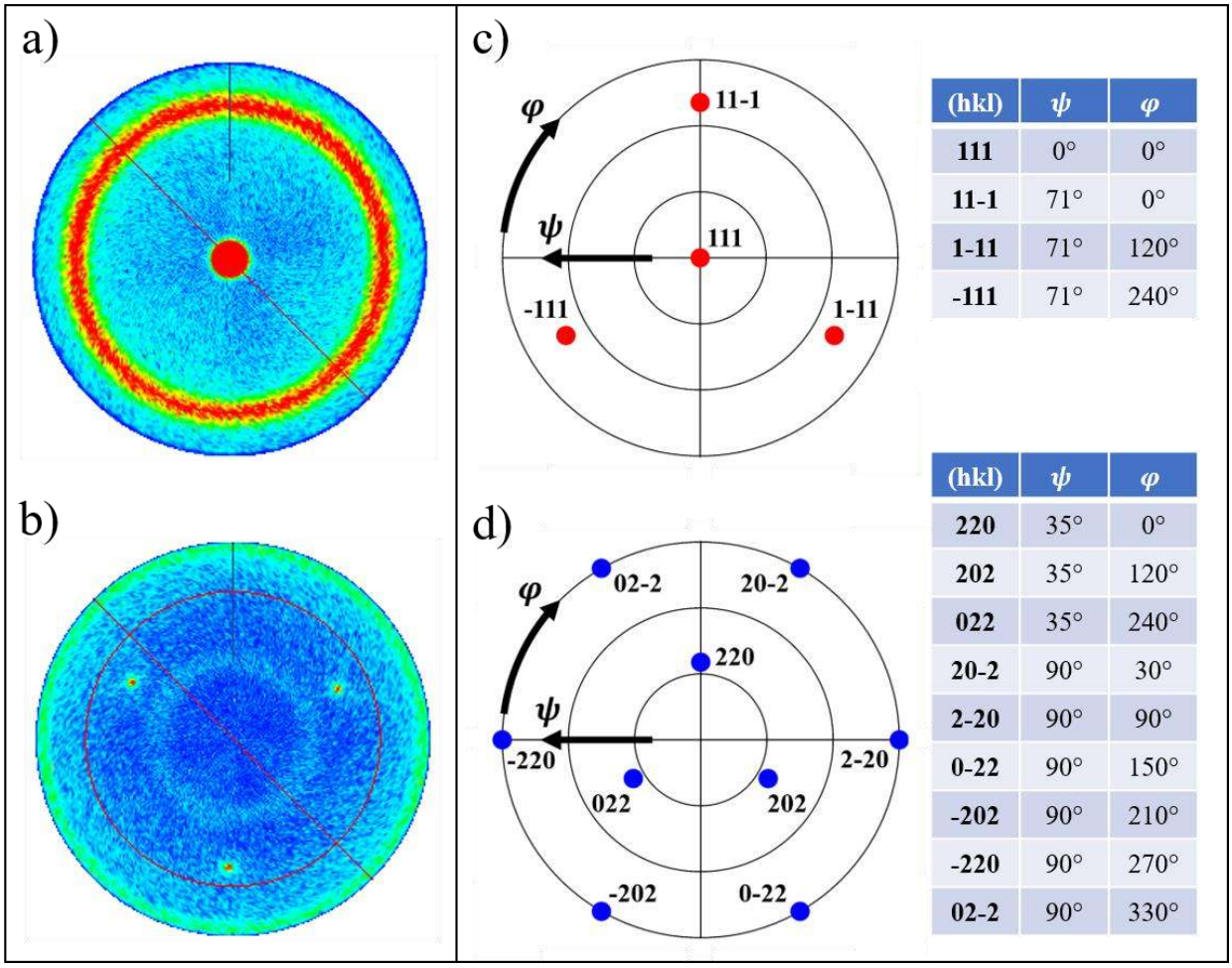

(hkl)	ψ	φ
111	0°	0°
11-1	71°	0°
1-11	71°	120°
-111	71°	240°

(hkl)	ψ	φ
220	35°	0°
202	35°	120°
022	35°	240°
20-2	90°	30°
2-20	90°	90°
0-22	90°	150°
-202	90°	210°
-220	90°	270°
02-2	90°	330°

Figure 3.8: XRD pole figure measurements of a IrMn/FeCo bilayer deposited over a Si(111)/SiO_2 substrate, taken at fixed a) $2\theta = 41.2°$ and b) $2\theta = 69.95°$. Schematic representation of the c) (111) and d) (220) reflections in a pole figure measurement of a (111) textured fcc perfect crystal.

3.2.3 Phase Identification by XRD analysis

In-plane $\varphi/2\theta_\chi$ scan

Once established that the spontaneous structural change consists in the crystallization of an initial amorphous or nanocrystalline phase, the next step involved the identification of the final phase developed in the IrMn. The studies of Imakita et al. and Tsunoda et al. showed that the combination of out-of-plane $\theta/2\theta$ and in-plane $\varphi/2\theta_\chi$ scans allows to discriminate between disordered γ-phase and ordered $L1_2$-phase of IrMn [Imakita, 2004; Imakita, 2005; Tsunoda, 2006]. This is possible because each of the {110}, {220} and {211} families include six lattice planes which are perpendicular to the (111) plane. If the IrMn is (111) textured, i.e. the (111) plane is parallel to the sample surface, these planes lay perpendicular to the sample surface. Hence, it is possible to detect them with an in-plane $\varphi/2\theta_\chi$ scan, i.e. a symmetric XRD measurement with the Bragg plane perpendicular to the sample surface. The total in-plane mosaicity of the IrMn grains confirmed by pole figure measurements implies a 360° dispersion of those planes which lay perpendicular to the surface, and therefore it grants their presence independently of the value of the rotation angle φ (see figure 3.8). Since only the $L1_2$-phase of IrMn generates the {110} and {211} reflections, this type of measurement allows to distinguish between the two phases.

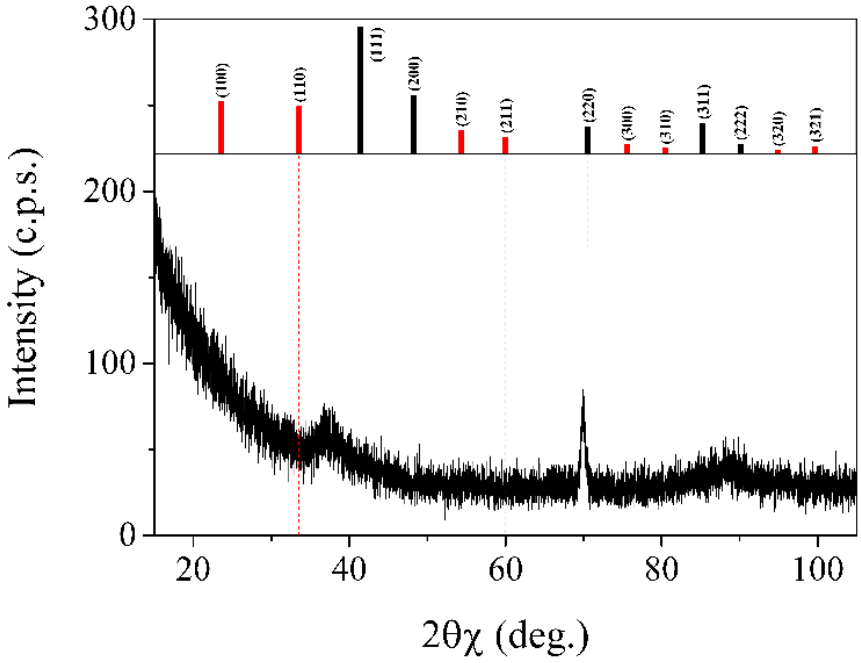

Figure 3.9: XRD in-plane $\varphi/2\theta_\chi$ scan taken after the conclusion of the structural transformation experienced by the IrMn. Upper diagram: calculated reflections of the $L1_2$-phase of IrMn.

An in-plane $\varphi/2\theta_\chi$ scan of an IrMn/FeCo bilayer is presented in figure 3.9. The out-of-plane $\theta/2\theta$ measurement of this particular sample showed only (111) and (222) diffraction peaks, which confirmed that the IrMn is (111) textured (data not shown). The upper diagram of figure 3.9 shows the nominal reflections of the $L1_2$-phase of IrMn, calculated from the lattice constant $a = 0.3772$ nm [Kohn, 2013], the Cu $K\alpha$ radiation of wavelength $\lambda = 0.154184$ nm and using a Lorentz factor of $1/\sin 2\theta$ [Imakita, 2004]. The black lines correspond to those reflections which are generated by both γ-phase and $L1_2$-phase of IrMn. The red lines represent the additional superlattice diffraction peaks which are the result of the atomic-ordering of the $L1_2$-phase. The scan in figure 3.9 reveals the presence of a sharp (220) peak, which confirms the goodness of the measurement. The absence of the (110) and (211) peaks, which are superlattice reflections of the $L1_2$-phase of IrMn, strongly indicates that the IrMn is in its γ-phase. Again, the broad peak that can be observed at $2\theta = 39°$, likely corresponds to the (110) reflection from the amorphous Ta layers.

Scherrer equation

The analysis of the crystallization process can be enriched by using the Scherrer equation, a formula that allows to estimate the mean crystallites dimension. The Scherrer equation is the result of mathematical considerations about the finite periodicity of equally spaced planes and it relates the size of sub-micrometer crystals to the broadening of diffraction peaks in XRD measurements [Cullity, 2014]. The Scherrer equation can be employed to estimate the average grains dimension as

$$t = \frac{K\lambda}{B\cos\theta_B}$$

where t is the mean crystallite size, K is a shape factor whose value is close to unity, λ is the wavelength of the radiation employed, B is the full width at half maximum (FWHM) of the peak and θ_B is the incident angle which satisfies the Bragg condition. The Scherrer equation gives an estimation of the crystallites dimension along the direction perpendicular to the Bragg plane. Hence, it is not correct to employ it with an asymmetric scan, e.g. a GID scan, in which the Bragg plane rotates during the measurement. In addition, the crystallite dimension estimated by the equation depends on the Bragg plane position, i.e. on the type of measurement. Using the Scherrer equation with an out-of-plane $\theta/2\theta$ scan will estimate the grain size along the depth of the film, which is evidently limited by the thickness of the layer. On the other hand, in an in-plane $\varphi/2\theta_\chi$ scan the Bragg plane is perpendicular to the film and the average

lateral grain size of the material can be evaluated using the Scherrer equation. Note that the finite size of crystallites is not the only reason for the broadening of diffraction peaks. In fact, both instrumental inaccuracies, such as divergence or non-monochromaticity of the incident X-ray beam, and sample properties, such as strain or crystalline defects, contribute to the broadening of the diffraction peaks.

Grain size analysis was performed by using the Scherrer equation on the diffractograms measured from multiple samples. The FWHM of the (111) and (220) peaks were evaluated from out-of-plane $\theta/2\theta$ and in-plane $\varphi/2\theta_\chi$ scans respectively. A value of $K = 0.9$ is used for the calculations. In the out-of-plane $\theta/2\theta$ scans, the IrMn (111) peak has a FWHM of 0.55° on average, which gives a longitudinal grain size of $t_{logitudinal} = 19\ nm$. This value is close to the real thickness of the IrMn layer evaluated by TEM (see section 3.3.2), which is about 17 nm. In the in-plane $\varphi/2\theta_\chi$ scans, the IrMn (220) peak can be used to derive the lateral grain size. The FWHM is about 0.65°, so the estimated lateral grain size results to be $t_{lateral} = 37\ nm$. Since the Scherrer equation relates the broadening of a diffraction peak with the crystallite size, it is interesting to observe that the FWHM of the IrMn (111) peak in figure 3.5 is constant during the peak formation. This observation excludes the possibility that the crystallites develop along the depth of the film. Therefore, the structural change must develop in the plane of the film. Confirmation of this fact would involve and analysis of the evolution of the broadening of the in-plane diffraction peaks. Unfortunately collecting a series of in-plane $\varphi/2\theta_\chi$ scan during the phase transition has not been possible so far. However, this observation was confirmed by the TEM analysis presented in section 3.3 and reinforced by the fits using the Avrami model, described in section 5.1.

3.2.4 Additional XRD studies

Samples without FeCo layer

A set of samples with structure Ta(3.5nm)/IrMn(15nm)/Ta(5nm) (AF-type) was produced and studied in order to determine to what extent the FeCo layer is relevant for the spontaneous crystallization process of the IrMn layer. Out-of-plane $\theta/2\theta$ scans were taken immediately after deposition and repeated until the crystallization finished. The results are analogous to the ones obtained for the bilayer with FeCo. The first scan shows no sign of texture in the as-deposited sample, and as time passes, a diffraction peak progressively develops at the angular

position $2\theta = 41.2°$, which corresponds to the IrMn (111) reflection. The peak has a FWHM of $0.48°$, which is only slightly smaller compared to the one obtained for the samples with the FeCo layer. However, a noteworthy difference was detected in the rocking curves, which are represented in figure 3.10. The graph includes two ω scans of the IrMn (111) reflection taken immediately after deposition and once the crystallization was completed. The rocking curve is well centered in zero and the FWHM is about 3°, considerably smaller compared to the samples with the FeCo layer shown in figure 3.7, which indicates a lower out-of-plane mosaicity. Pole figure measurements confirm both the random in-plane orientation of the IrMn grains and improved texture due to the low out-of-plane mosaicity of the samples without the FeCo layer. In conclusion, the structural analysis of samples without the FeCo layer indicates that the structural properties of IrMn are mostly independent of the presence of the FeCo, with the exception of a lower out-of-plane mosaicity. Therefore, the presence of the FeCo layer does not seem to influence the crystallization process experienced by the IrMn, but it may influence its final texture by inducing a larger mosaicity of the crystalized grains.

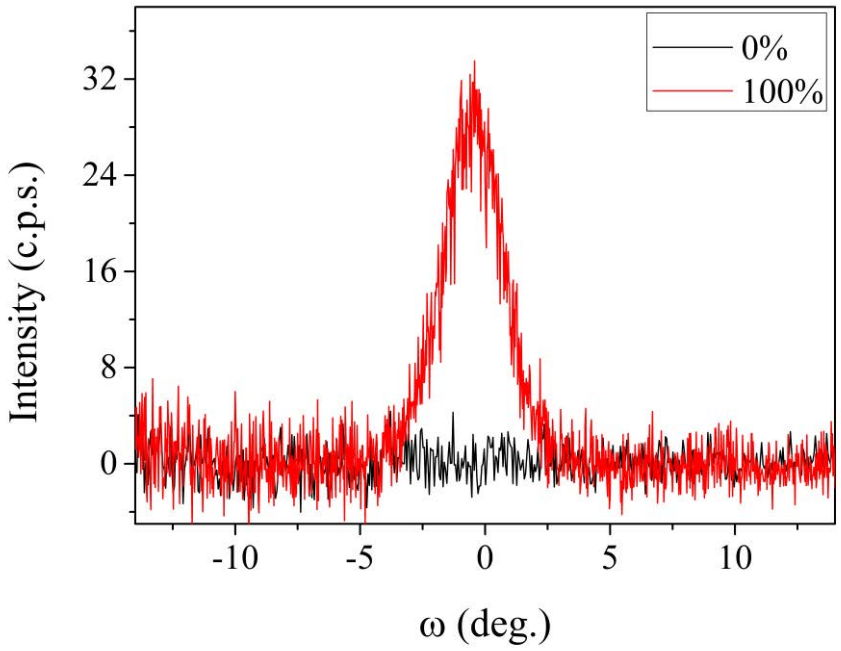

Figure 3.10: XRD ω scans (rocking curves) of the IrMn (111) reflection for a sample without FeCo layer, taken at different stages of the structural transformation in the IrMn.

Samples without Seed Layer

Over the last two decades, the influence of the crystallographic orientation of the AF grains on the exchange bias has been a topic of discussion. In fact, while many studies have confirmed

that the (111) texture of IrMn promotes a stronger exchange bias [Hoshino, 1996; Pakala, 2000; Anderson, 2000], there also are a few studies that indicate that it does not affect the strength of the exchange bias [Devasahayam, 1998; Yagami, 2001]. Nevertheless, the (111) texture of IrMn is considered extremely important for technological applications based on exchange bias. Since deposition by magnetron sputtering generally leads to polycrystalline IrMn with randomly oriented grains, much attention has been focused on the influence of the material used as the seed layer (SL) on the texture of the IrMn layer. Over the last two decades, many materials have been tested and results are sometimes contradictory (e.g. Zr [Hoshino, 1996], Ta [van Driel, 2000], NiFe [Anderson, 2000], NiCr [Aley, 2008]).

As explained in the previous sections, the samples presented in this work generally include a Ta seed layer to promote the (111) texture of IrMn [van Driel, 2000]. Contrary to these studies, in which the orientation of the IrMn grains was set during the sputtering process, in this thesis the IrMn is initially deposited in a metastable amorphous or nanocrystalline phase and it is the crystallization process of the IrMn what leads to the formation of a highly (111) textured polycrystalline phase. In order to understand whether the Ta seed layer plays a role or not in the promotion of the (111) texture during the crystallization of the IrMn, samples with the structure IrMn(15nm)/Ta(5nm) were deposited over oxidized silicon substrates. Thus, the IrMn was grown directly over an amorphous layer of SiO_2 instead of the Ta seed layer. The characterization of these samples showed results equivalent to the ones on samples with a Ta seed layer, and the (111) texture of the crystalized IrMn is comparable. Therefore, the samples studied in this work do not require the presence of a Ta seed layer to develop a high (111) texture. Alternatively, one can state that both a Ta seed layer and an oxidized silicon substrate can promote the (111) texture of IrMn, when this material experiences a slow crystallization at room temperature. Nonetheless, this study introduces the interesting possibility of removing the seed layer from this type of structures, which can be relevant for the design of devices based on exchange bias.

Out-of-plane mosaicity

Few of the IrMn/FeCo bilayers deposited in this thesis, showed a non-expected mosaicity dispersion, as revealed by the unusual rocking curves presented in figure 3.11. This figure shows two ω scans (rocking curves) of the (111) reflection of IrMn, taken in the final stages of the structural transformation. The response in the ω scan is broader than usual and characterized by a peculiar shape, which can be interpreted as the result of the overlap of three

different peaks, respectively at $\omega = -6°, -1°$ and 5°. This would mean that in these samples there are three preferred orientations for the IrMn (111) planes. The effect of this overlap is a large broadening of about 16°, which implies a prominent out-of-plane mosaicity of the IrMn layer. Even though the unusual shape of the rocking curve complicates the evaluation of its FWHM, the average mosaicity seems to be constant with time, which indicates again the absence of a relevant reorientation of IrMn grains. Besides the uncommon out-of-plane mosaicity, these samples showed standard responses to further structural and magnetic studies, which is the general trend in all the other samples.

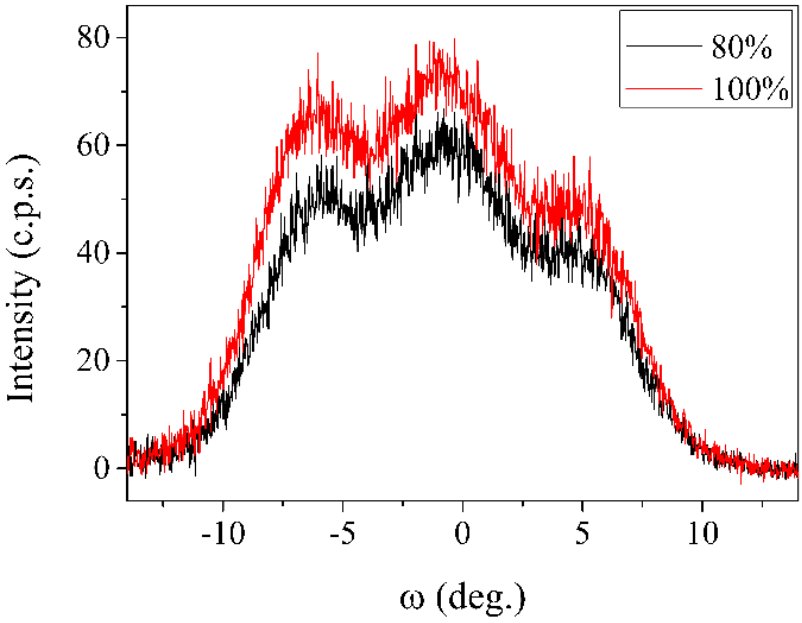

Figure 3.11: XRD ω scans (rocking curve) at the IrMn (111) reflection of one of the few AF/F-type samples which show three preferred texture orientations.

In summary, the structural characterization presented in this section shows a peculiar behavior of the IrMn layer. The as-deposited material is initially in a metastable state, probably amorphous or nanocrystalline with some random oriented grains, and it experiences a phase transformation which lasts a few days. The process seems to consist in a two-dimensional growth crystallization, and it leads to a highly (111) textured γ-phase of IrMn, with rather large lateral grains size (37 nm). The texture analysis also shows large out-of-plane mosaicity and random in-plane orientation of the IrMn grains. Among the other materials used in these multilayers, only a low diffraction signal produced by the amorphous Ta layer is detected. The FeCo layer seems only to influence the out-of-plane mosaicity of the IrMn grains. The Ta seed

layer does not seem to influence the crystallization process, and it is not necessary for the promotion of the (111) texture of the IrMn.

3.3 Transmission Electron Microscopy measurements

The structural information retrieved by the XRD measurements presented in the previous section gives only an average picture of the structural properties of IrMn. In order to provide more detailed structural information, the XRD study was completed with a thorough characterization performed by transmission electron microscopy. In this section, the most relevant results obtained by TEM imaging are presented and discussed, providing additional information about the IrMn structural properties. In the first subsection, the evidence of the crystallization of the as-deposited IrMn is provided through a sequence of plan-view TEM images taken during the structural transformation. In addition, selected area diffraction (SAD) imaging reveals the crystallographic nature of the IrMn before and after crystallization. In the second subsection, both initial and final phases are precisely identified by carefully analyzing SAD patters and HAADF-STEM images, which eventually exclude the presence of the $L1_2$-phase of IrMn. The third subsection contains additional studies, achieved by EDS, EELS and further SAD pattern analysis, which focus on the structural properties of the crystallized IrMn, such as texture, stoichiometry, and grains size.

3.3.1 Crystallization of IrMn

Two types of multilayers were produced by magnetron sputtering for TEM characterization purposes, namely the AF-type with structure Ta(3.5nm)/IrMn(15nm)/Ta(5nm), and the AF/F-type with structure Ta(3.5nm)/IrMn(15nm)/FeCo(5nm)/Ta(5nm). The samples were deposited over three different substrates in the same sputtering run: naturally oxidized Si(100), thermally oxidized Si(111)/SiO_2(400nm) and copper TEM grid. Si substrates were employed for cross-section TEM measurements, as the thin layer of naturally oxidized Si allows to align the cross-section specimen with the crystalline Si underneath it. Si/SiO_2 substrates were used as reference samples, in order to check whether the substrate choice could influence the structural and magnetic properties of the deposited materials. Copper TEM grids were used for plan-view TEM measurements. Overall, the samples showed the same structural behavior regardless of the type of substrate. In addition, the magnetic response of samples deposited over Si and

Si/SiO_2 substrates proved to be equivalent. Magnetic characterization of samples deposited over TEM grids was not performed.

Samples deposited over naturally oxidized Si substrate were properly treated to produce cross section TEM specimens. The specimen preparation consists in cutting one-millimeter thin slices of the sample and polishing both sides, firstly with diamond lapping disks and then by ion milling, thanks to a precision ion polishing system (PIPS). The result is a cross section specimen of a thickness smaller than 100 nm, glued on a copper TEM grid. In this work, the sample preparation was performed by Dr. Balati Kuerbanjiang of the University of York. Since the sample preparation usually takes a few days and it involves treatments at a temperature as high as 400 K, the IrMn present in the cross-section specimens is expected to be totally crystallized.

Plan-view TEM imaging

Plan-view imaging was performed on both types of sample deposited over copper TEM grids. During the measurements, which took place within one day after deposition, the samples were still experiencing the structural change previously detected by XRD. This allowed to analyze the nature of the phase transformation as well as to capture images of the ongoing process. Figure 3.12 shows two plan-view images of an AF-type sample taken at different magnifications. Overall, the sample is characterized by well-defined areas which generate two different types of contrast (a). The bright and dark contrast of the bottom left portion of the sample shown in figure 3.12a is typical of a very ordered crystalline phase. The rest of the sample, instead, is characterized by grey contrast with few small dark spots, which suggests that the as-deposited material has a poorly crystalline structure, mainly amorphous, with some nanocrystalline grains. A magnified image of the area delineated by the yellow square is presented in figure 3.12b. This image shows the boundary between the crystallized portion of the sample on the left and the as-deposited material on the right. Grain size analysis indicates that the crystalline grains present in the as-deposited material are randomly oriented and have an average lateral grain size of about 5-6 nanometers, which can be observed in the four grains visible on the right of figure 3.12b. These randomly oriented grains present in the as-deposited material are likely to be the source of the IrMn (111) reflection signal detected in the early GID measurement of figure 3.6 (black curve).

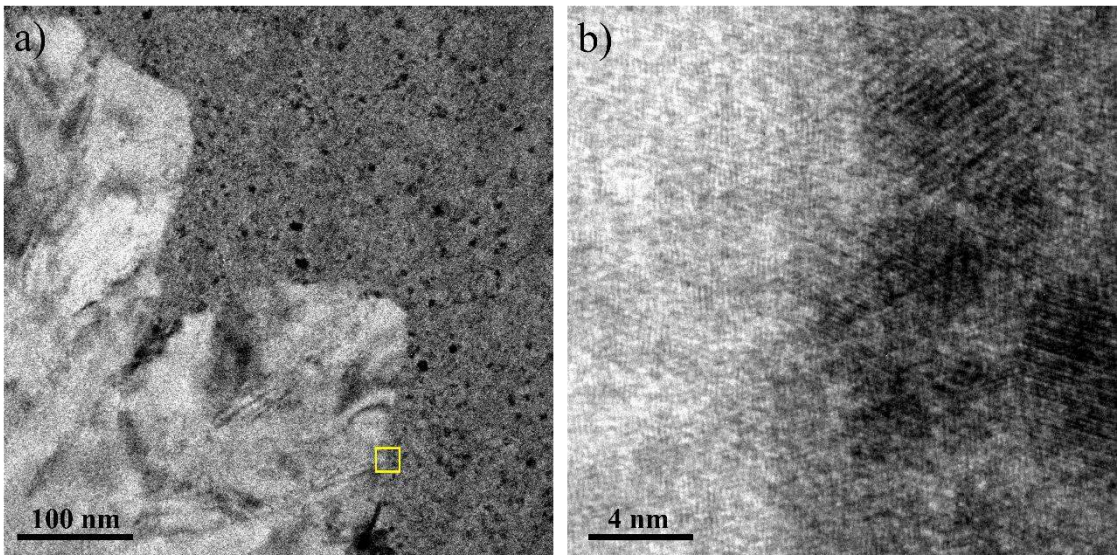

Figure 3.12: Plan-view TEM images of an AF-type sample at different magnifications.

A selection of a series of plan-view TEM images of the same sample, taken during a period of about 10 minutes, are presented in Figure 3.13. These images show the progressive lengthening of the crystalline portion of the sample at the expense of the as-deposited material. This confirms that the structural development detected by XRD measurements consists in a 2-dimensional structural transformation which increases the crystallinity of the sample. The TEM measurement also confirms that this crystallization is spontaneous at room temperature, as various precautions were taken in order to avoid secondary effects due to the exposure to the highly energetic electron beam. Nucleation phenomena induced by the electron beam were never detected, even during prolonged exposure of small areas of as-deposited material. Images were taken every 10 seconds, during which time the electron beam was shuttered, with an exposure time of less than one second. Hence, the possibility of thermal activation induced by local heating during prolonged TEM exposure was minimized. Further imaging with a longer waiting period between captures excluded the possibility that the crystallization rate detected here is influenced by the interaction with the electron beam.

It is interesting to note that the grains present in the as-deposited material vanish once the sample crystallizes. For instance, when observing the sequence e-f-g of figure 3.13, one can notice that the dark crystalline grain outlined by the red circle, which initially lays close to the edge of the crystalline area (e-f), is not present within the newly crystallized part at the end of the sequence (g). This effect recalls the grain reorientation detected by GID measurements and shown in figure 3.6, in which the intensity of the initial IrMn (111) reflection caused by

randomly oriented grains lowered as the structural change progressed. The TEM images indicate that this grain reorientation is caused by the spreading of the crystallization.

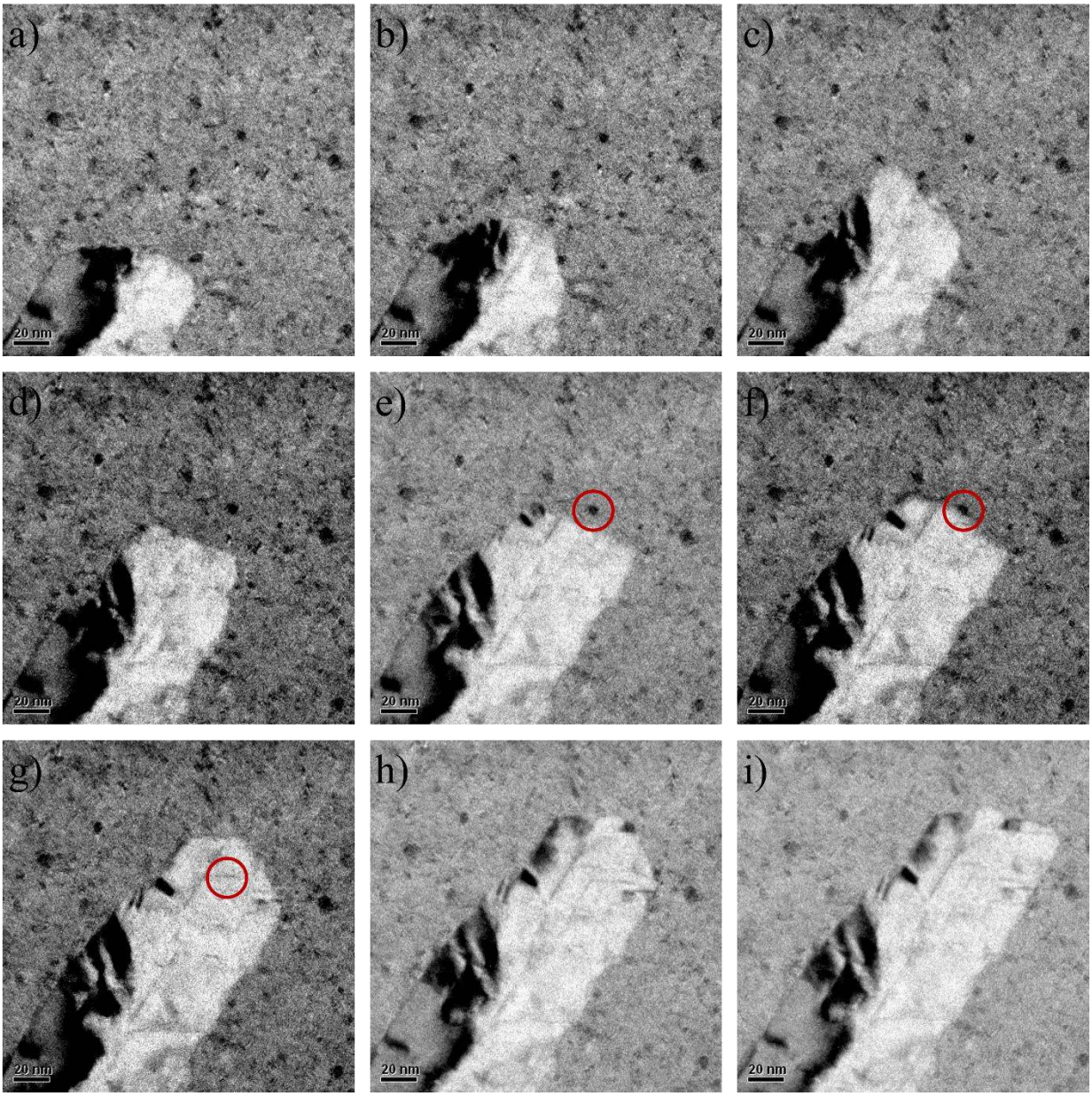

Figure 3.13: Plan-view TEM images of the structural transformation in an AF-type sample. Images are captured every minute.

Plan-view SAD imaging

In plan-view imaging of multilayered samples deposited over TEM grids, the contribution from each layer to the final image is not clearly distinguishable. In this specific case, the samples consist of a 15-nm-thick layer of IrMn, a 5-nm-thick layer of FeCo when present, and two layers of Ta, for a total thickness of 8 nm. Hence, in order to identify which layer is responsible for the crystallization process detected in figure 3.13, TEM selected area diffraction (SAD)

studies were performed on both AF-type and AF/F-type samples. SAD imaging of a specimen produces a diffraction pattern which is directly related to the crystallographic structure of the materials present in the sample. The shape and the dimension of a SAD pattern can be compared with the tabulated values to identify the crystallographic properties of the various materials present in the sample.

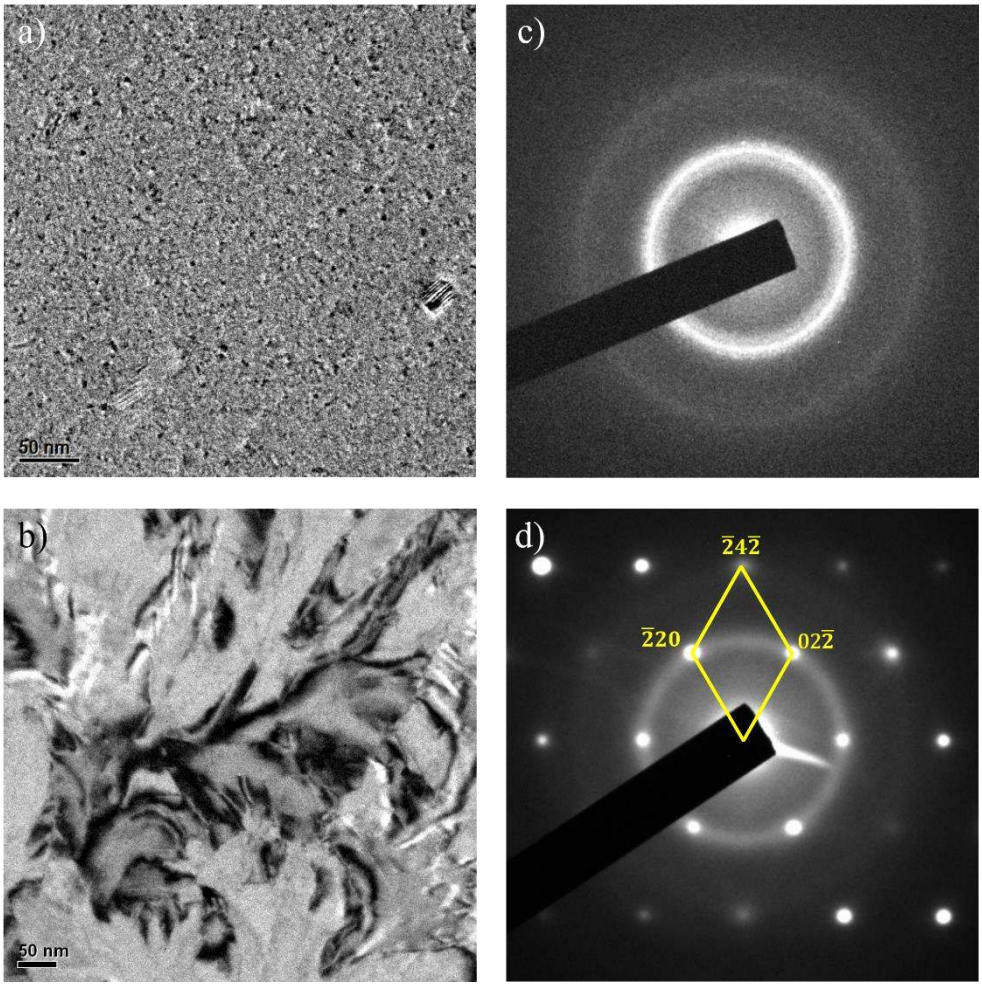

Figure 3.14: Plan-view TEM real and SAD images of as-deposited (a and c) and crystallized (b and d) areas of an AF-type sample.

Figure 3.14 shows plan-view images of two different areas of an AF-type sample (a and b) and their corresponding SAD images (c and d). As shown in the plan-view images, the two areas were chosen to contain mainly the as-deposited and the crystallized phases respectively. Images a and c confirm that the as-deposited material is in a poorly crystalline phase. In fact, the SAD pattern consists in two shaded rings, which is an indication of amorphous/nanocrystalline order. From the analysis of the SAD pattern the interplanar spacing for the two rings results to be about $d = 1.34$ Å and $d = 0.77$ Å, which correspond respectively to the (220) and (422)

reflections of IrMn, according to equation 2.2. Images b and d show that the crystallized phase is highly ordered, almost perfectly crystalline, as confirmed by the dotted pattern in the SAD image. The annular signal, which is still present even though less intense, is probably due to small areas of the sample which had not experienced the phase transformation yet.

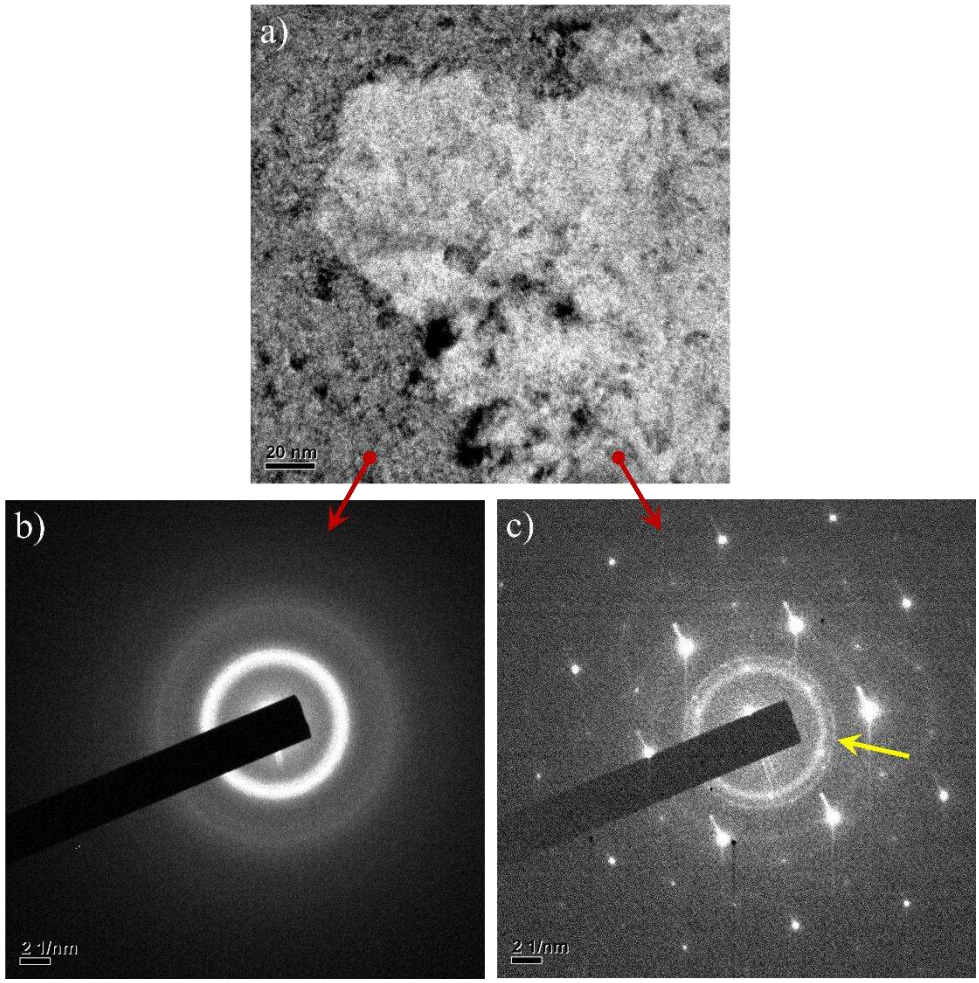

Figure 3.15: a) Plan-view TEM image of an AF/F-type sample, taken at the boundary between as-deposited and crystallized material. SAD images of b) as-deposited and c) crystallized areas.

The analysis of the diffraction pattern provides much information about the crystalline phase developed after the structural transformation. Firstly, the first and second closest reflections (yellow lines in figure 3.14d) lay at the same distances of the two rings of figure 3.14c, therefore they correspond to the (220) and (422) reflections of IrMn. This confirms that the structural transformation shown in figure 3.13 takes place in the IrMn layer only, as previously indicated by XRD characterization. Secondly, the identification of these reflections and their periodicity allow to determine the texture of the material. In fact, the SAD pattern of figure 3.14d corresponds to the (111) zone axis of an fcc crystal, which implies that the crystallized IrMn is (111) textured. Finally, the total absence of in-plane rotation of the diffraction pattern, apart

from the slight annular signal due to the non-crystallized areas, indicates that the IrMn in this portion of the sample is almost single crystalline. In both SAD images, no signal due to Ta is detected, probably because of the small thicknesses and poor crystalline order of the Ta layers.

Plan-view and SAD images were also taken for AF/F-type samples, i.e. with a 5-nm-thick FeCo layer deposited on top of the IrMn (figure 3.15). The images confirm that the IrMn experiences the same crystallization process detected in AF-type sample, as shown in figure 3.15a. SAD images of as-deposited and crystallized material are respectively presented in figure 3.15b and figure 3.15c. As for the AF-type sample, the as-deposited material is poorly crystalline, mainly amorphous or nanocrystalline, and produces shaded rings in the SAD image (b). Once again, the final phase of the IrMn is highly ordered as confirmed by the dotted pattern in the SAD image (c). The analysis of the diffraction pattern leads to the same results for both types of sample, i.e. the IrMn is almost perfectly crystalline and it is (111) textured. Besides the pattern due to the IrMn, the thin annular signal pointed out by the yellow arrow in figure 3.15c has an interplanar spacing of about $d = 1.16$ Å, which corresponds to the (211) reflection of FeCo, according to equation 2.2. This implies that the FeCo layer is in a polycrystalline phase, with randomly oriented grains.

3.3.2 Phase Identification by TEM analysis

As introduced in section 3.1, deposition of IrMn by magnetron sputtering generally leads to polycrystalline disordered γ-phase [Tsunoda, 2006]. However, in the previous sections it was shown that the sputtering conditions employed in this work lead to a metastable state for the as-deposited IrMn, which consists in an amorphous/nanocrystalline phase. As time passes, the IrMn experiences a 2-dimensional crystallization at room temperature, which leads to a highly ordered and very well textured IrMn phase. According to Raub et al. [Raub, 1955], in this range of composition, i.e. $Ir_{25}Mn_{75}$ nominally, the crystallized IrMn could be in the disordered fcc γ-phase or in the $L1_2$ ordered phase. As shown by Kohn et al., the exchange bias induced by the two phases of IrMn is largely different [Kohn, 2013]. Hence, it is crucial to exactly identify which phase the IrMn assumes when it crystallizes. As shown in section 3.2.3, the XRD characterization suggests that the crystallized IrMn is in a disordered γ-phase. In order to further clarify this point, phase identification of the crystallized IrMn was achieved using three types of TEM analysis, namely SAD imaging of plan-view and cross-section specimens and HAADF at atomic resolution.

Plan-view SAD imaging

As explained in section 3.1, phase identification of deposited IrMn can be achieved by comparing the diffraction pattern of the specimen with the tabulated ones for the two phases and verifying the absence (or presence) of the superlattice reflections induced by the perfect atomic-ordering of the $L1_2$-phase. Such a comparison with a plan-view SAD image of an AF-type sample deposited over a TEM grid is presented in figure 3.16. As explained in the previous section, the diffraction pattern shown in the plan-view SAD image (a) belongs to IrMn in the (111) zone axis (i.e. the view is parallel to the (111) lattice plane). Hence, the SAD image is compared with the calculated SAD patterns in the (111) zone axis for the γ-phase (b) and the $L1_2$-phase (c) respectively. The absence of the superlattice diffraction spots, e.g. the (110) and the (211) reflections indicated with red circles in figure 3.16a, confirms that the IrMn is in its γ-phase.

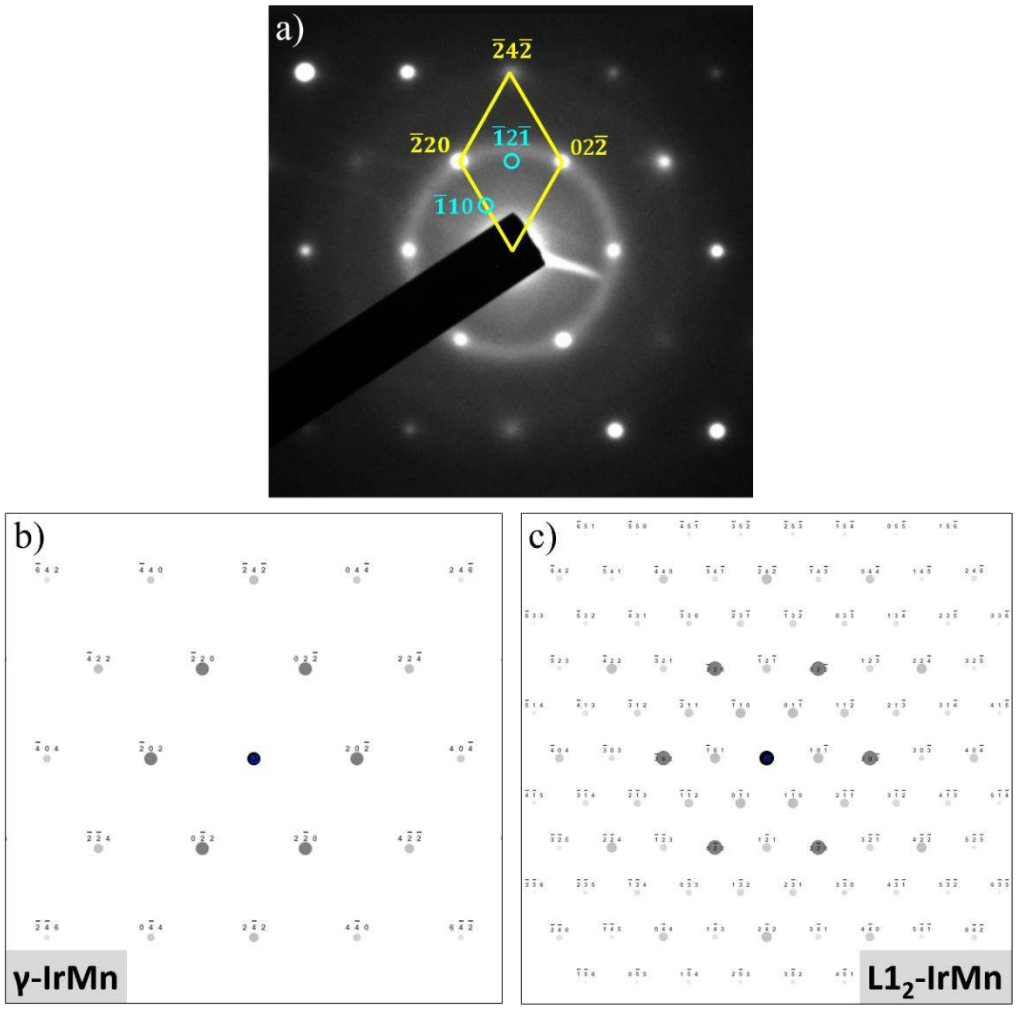

Figure 3.16: a) Plan-view SAD image of crystallized IrMn and calculated SAD patterns for b) γ-phase and c) $L1_2$-phase of IrMn in the (111) zone axis.

Cross-section SAD imaging

The same analysis for a cross-section specimen is presented in figure 3.17. Besides the diffraction signal due to the IrMn, the SAD image (a) now includes the diffraction pattern of the substrate, which for cross-section specimens is naturally oxidized Si(100). The dashed blue lines in figure 3.17a indicate the first and second closest reflections from the substrate, whose interplanar spacing results to be about $d = 3.13$ Å and $d = 2.71$ Å. According to equation 2.2,

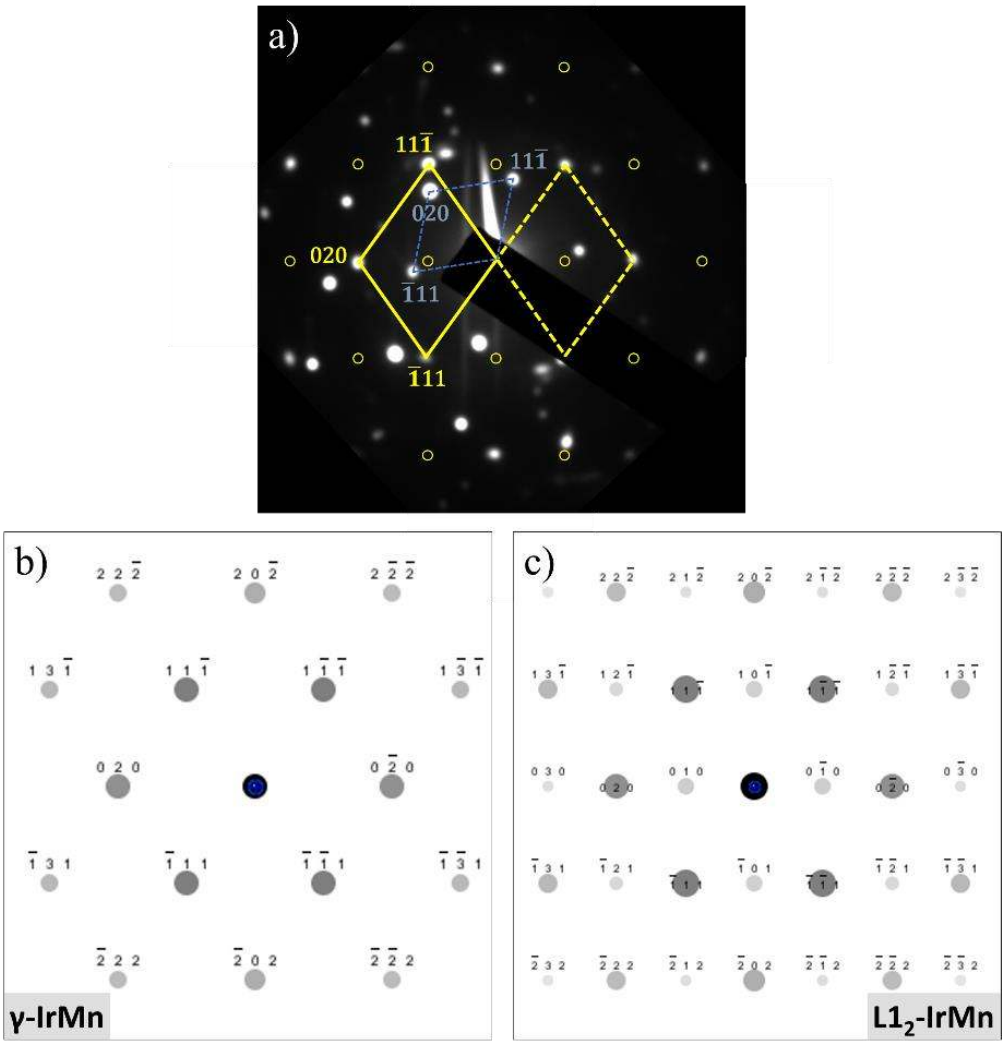

Figure 3.17: a) Cross-section SAD image of crystallized IrMn and calculated SAD patterns for b) γ-phase and c) $L1_2$-phase of IrMn in the (110) zone axis.

these values correspond respectively to the (111) and (200) reflections of Si, which confirms that the Si is in the (110) zone axis with the (020) lattice plane parallel to the surface of the original sample. The yellow lines, instead, indicate the first and second closest reflections from the IrMn, whose interplanar spacing results to be about $d = 2.18$ Å and $d = 1.89$ Å. According to equation 2.2, these values correspond respectively to the (111) and (200) reflections of IrMn,

which confirms that the IrMn is in the (110) zone as well. The good alignment between the (111) reflection of the IrMn and the (020) reflection of the Si confirms that the IrMn is very well textured in the (111) direction. The SAD image is compared with the calculated SAD patterns in the (110) zone axis for the γ-phase (b) and the $L1_2$-phase (c) respectively. The absence of any of the superlattice diffraction spots, which are indicated with yellow circles in figure 3.17a, confirms that the IrMn is in its γ-phase.

Cross-section high resolution HAADF-STEM imaging

As explained in section 3.1, phase identification can be achieved also by high resolution STEM measurements of a cross-section specimen, using a high-angle annular dark-field (HAADF) detector [Kohn, 2013]. This type of detector collects electrons scattered at relatively large angles, allowing the possibility to produce atomic-number contrast. In order to achieve atomic resolution, a series of STEM images of the same portion of the specimen are collected, aligned and merged together. A high resolution HAADF-STEM image of the IrMn of a cross-section specimen is presented in figure 3.18a. In agreement with the previous structural characterization, the atomic arrangement shown in the image corresponds to the (110) zone axis of the IrMn, with the (111) lattice plane parallel to the surface of the original sample. On the right of figure 3.18, the schematic atomic structures in the (110) zone axis and the corresponding HAADF-STEM simulations for the two phases of IrMn are presented. In case of γ-phase, Mn and Ir atoms are randomly positioned within the crystal lattice (d), hence the simulated HAADF-STEM image shows no atomic-number contrast (b). In case of $L1_2$-phase instead, the Cu_3Au order implies that some Mn atoms line up (central white spheres in figure 3.18e) and, being Mn lighter than Ir, produce a dimmer contrast in the simulated HAADF-STEM image (c). As no atomic-number contrast is detected in the HAADF-STEM image, the comparison with the simulations indicates once again that the crystallized IrMn is in the disordered fcc γ-phase. The same conclusion can be drawn by analyzing the 2-dimensional Fourier transform, calculated with a Fast Fourier Transform (FFT) algorithm, of the HAADF-STEM image. The FFT image, shown in figure 3.18f, can be compared with the calculated diffraction patterns in the (110) zone axis of the two phases (g and h). The random atomic positioning of the γ-phase is confirmed by the absence of the superlattice spots indicated with red circles in figure 3.18f.

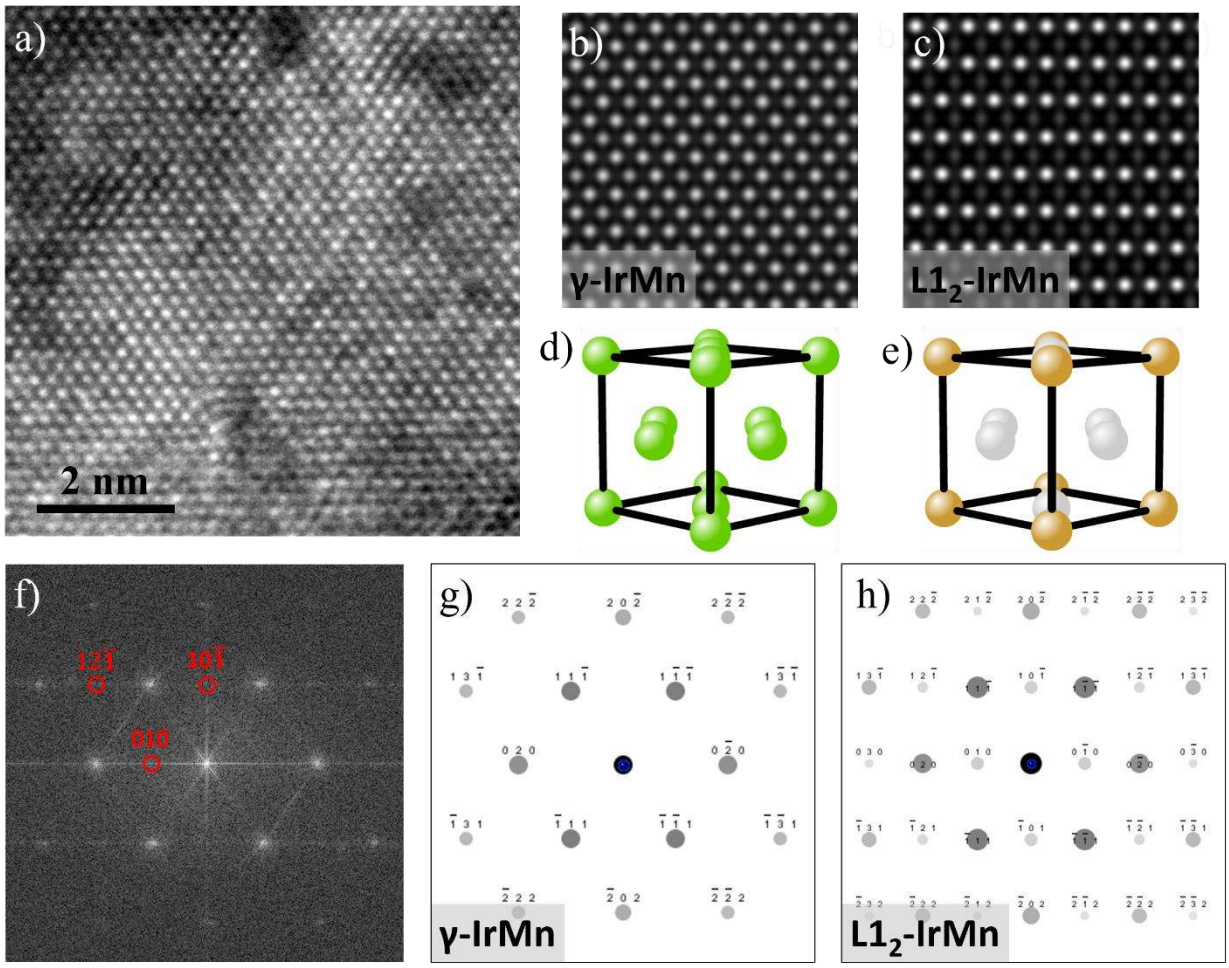

Figure 3.18: a) HAADF-STEM image at atomic resolution of the IrMn layer and simulations for b) γ-IrMn and c) $L1_2$-IrMn in (110) zone axis; schematic model of d) disordered fcc and e) Cu_3Au-type structures in the (110) zone axis; f) FTT of the HAADF image calculated by GMS 2; tabulated SAD patterns for g) γ-phase and h) $L1_2$-phase of IrMn in the (110) zone axis.

3.3.3 Structural properties of crystallized IrMn

Energy dispersive X-ray spectrometry

Since the exact composition of the deposited IrMn likely plays a role in the spontaneous crystallization studied in this work, energy dispersive spectrometry (EDS) measurements of various samples were performed, using the EDS detector mounted on the transmission electron microscope. The compositional analysis involved all the samples produced for plan-view TEM imaging, whose structure is either Ta/IrMn/Ta or Ta/IrMn/FeCo/Ta, deposited over copper TEM grids. EDS spectra of both AF/F-type and AF-type samples are presented in figure 3.19. Note that the peak identified as chromium (Cr) at about 5.4 keV was confirmed to be due to

contamination of the sample holder. Contamination from cobalt (Co) and iron (Fe) was also detected. For compositional analysis purpose, the EDS measurement of each sample was repeated at different positions. Since the L lines of Ir overlap with the K lines of Cu, which is largely present in the TEM grid, the compositional analysis was performed using the M lines of Ir and the K lines of Mn. All the samples showed an average composition of $Ir_{30}Mn_{70}$, which is richer in Ir than the sputtering target, whose nominal is $Ir_{25}Mn_{75}$. The EDS measurements also confirmed that the deposited FeCo has a composition of $Fe_{39}Co_{61}$, close to the nominal one.

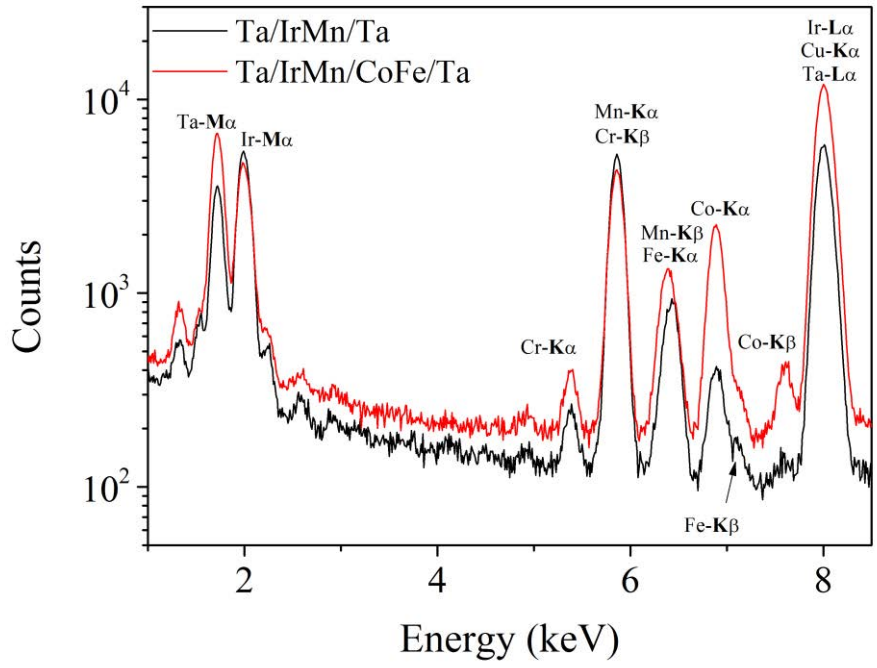

Figure 3.19: EDS spectra of AF-type (black) and AF/F-type (red) samples deposited over copper TEM grids.

Electron energy loss spectrometry

Figure 3.20 shows cross-section images of an AF-type (a) and an AF/F-type (b) samples. The effective thickness of the layers is consistent with the expected one, having 17 ± 1 nm of IrMn and 4 ± 0.4 nm of FeCo. The interface between different materials is well defined and mostly smooth all along the sample, with the exception of the IrMn/FeCo interface, which is characterized by a more prominent roughness as shown in figure 3.20c. Such a roughness might be caused by the sputtering conditions, which involves highly energetic FeCo clusters accelerated toward the soft amorphous/nanocrystalline phase of IrMn. On the other hand, the

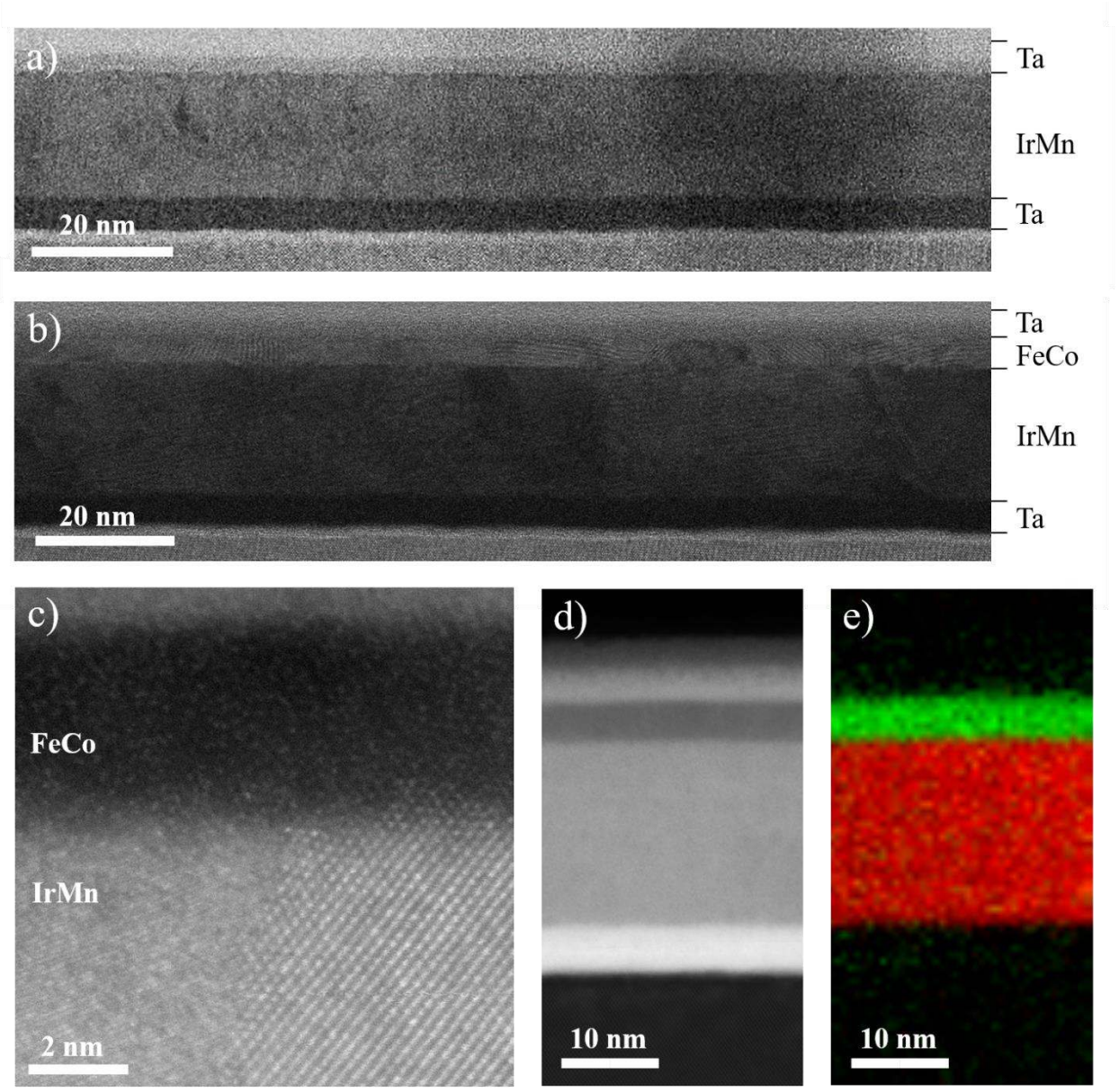

Figure 3.20: Cross-section TEM images of a) AF-type and b) AF/F-type samples; c) magnified view of the interface between IrMn and FeCo layers; d) HAADF and e) EELS images of the same area of an AF/F-type sample.

roughness might be a consequence of the spontaneous crystallization of IrMn, which could allow energetically favorable repositioning of Co, Fe, Ir and Mn atoms at the interface between the two layers. In order to define whether the sample preparation for cross-section TEM, which involves annealing at temperature as high as 130° C, caused atomic interdiffusion among layers, local electron energy loss spectrometry (EELS) measurements were performed. During scanning TEM (STEM) imaging of a small portion of the cross-section specimen (d), the local EELS spectrum was collected. By comparing the features of the EELS spectra related to each element present in the specimen with the STEM image, a chemical map of the sample can be

outlined. The result is presented in figure 3.20e, where the red contrast corresponds to the EELS signal produced by Mn and Ir atoms and the green contrast corresponds to Co and Fe atoms. Since the two areas are well defined and do not overlap, EELS analysis indicates that no interdiffusion occurred between the IrMn and FeCo layers.

Cross-section dark-field imaging

As explained in section 2.2.2, the complex system of lenses and apertures of a transmission electron microscope allows to filter the transmitted electrons according to the diffraction properties of the specimen. By controlling the objective aperture, it is possible to select a specific area of the SAD image so to allow the transmission of the electrons scattered in that specific direction. This measuring setup is called dark-field imaging (DF) and it permits to map the origin and the intensity of the selected diffracted signal. Figure 3.21a shows the SAD pattern of a cross-section AF/F-type specimen. The brightest spots in the diffraction image are due to the reflections of the Si (100) substrate, which are indicated with blue dashed lines. The Si is in the (110) zone axis, with the (200) reflection pointing toward the surface of the original sample. The spot indicated by the yellow circle corresponds to the (111) reflection of IrMn, whose direction is represented by the dotted yellow line and results to be rotated by about 7° from the (200) direction of the Si substrate, confirming that the material is (111) textured. The IrMn (111) diffraction spot consists in an elongated dot, which confirms the important out-of-plane mosaicity detected in the rocking curve analysis (see section 3.2.2).

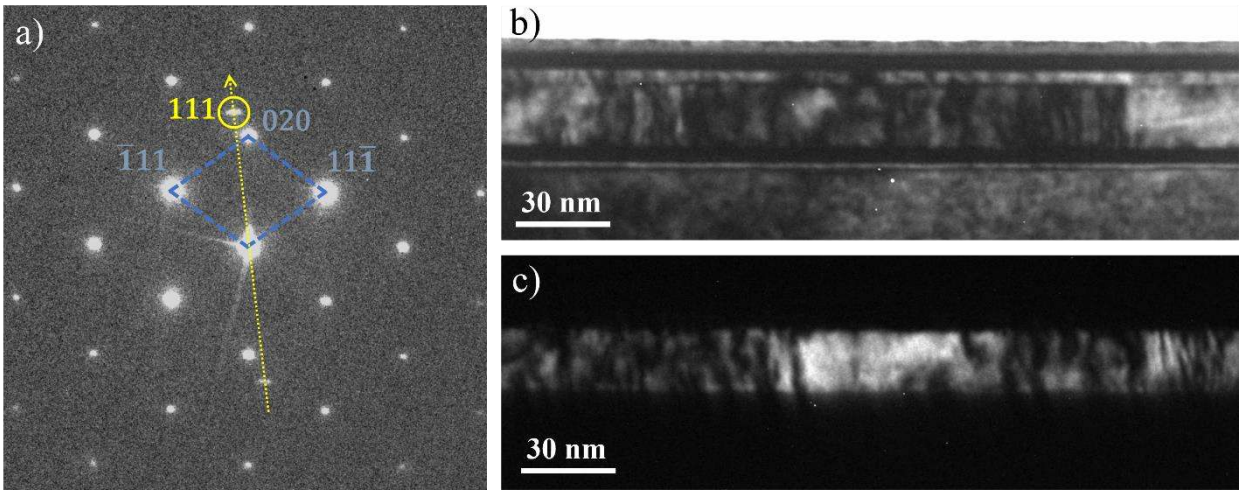

Figure 3.21: a) SAD pattern of a cross-section AF/F-type specimen; b) standard cross-section image; c) dark-field image of the same region, obtained by using the (111) reflection of IrMn, which is pointed out by the yellow circle in (a).

When the objective aperture is completely open, all the transmitted electrons, scattered and un-scattered, are allowed to reach the detector, and the conventional TEM image of the cross-section specimen is formed (b). By reducing and displacing the objective aperture over the IrMn (111) diffraction spot (yellow circle), all the electrons but the ones scattered in that direction are filtered out. The result is a dark-field image (c) where the bright contrast corresponds to the diffracted intensity due to the (111) lattice planes of IrMn. The analysis of the DF image indicates that the IrMn layer consists of single crystal grains, larger than 100 nm, with extended defects, represented as dark contrast, that propagate through its entire thickness. In section 3.2.3, a lateral grain size of about $t_{lateral} = 37\ nm$ was estimated by using the Scherrer equation on an in-plane $\varphi/2\theta_{\chi}$ scan. The fact that this value is considerably smaller than the effective lateral grain size extracted by DF imaging, which exceeds the 100 nm, can be explained by the presence of several transversal defects which break the crystal order and, therefore, lower the estimation of the Scherrer analysis. Nonetheless, such a large value of lateral grain size in materials deposited by magnetron sputtering is uncommon and it is likely the effect of the slow crystallization of the as-deposited amorphous/nanocrystalline IrMn.

In summary, the TEM characterization presented in this section adds relevant structural information to the previous analysis performed by XRD. Plan-view TEM imaging confirms that the crystallinity improvement detected by XRD is due to the crystallization of the IrMn layer, which happens by two-dimensional growth of very ordered crystallites. The as-deposited IrMn is initially in a poorly crystalline phase with some random oriented grains, as shown by plan-view SAD imaging. Multiple techniques analysis clearly indicates that, after crystallizing, the final phase of the IrMn is that of a disordered fcc γ-phase, with very large lateral grains size (over 100 nm). Additional characterization by EELS and EDS reveals the absence of interdiffusion and the low quality of the IrMn/FeCo interface, as well as the exact stoichiometry of the sputtered alloys which is relatively close to the nominal values. The TEM analysis also confirms that the deposited Ta is amorphous, whereas the FeCo is polycrystalline, with small randomly oriented grains.

3.4 Conclusions

In order to give the reader a comprehensive vision over the structural properties of sputtered IrMn, the most relevant results of this extensive structural characterization are summarized here. The samples studied in this section are multilayers deposited by magnetron sputtering,

with generic structure SL/IrMn(15nm)/FeCo(5nm)/CL. The 15-nm-thick IrMn layer is deposited by RF magnetron sputtering at a high deposition rate from a target of nominal composition $Ir_{25}Mn_{75}$. EDS measurements show that the actual composition of the sputtered material is $Ir_{30}Mn_{70}$ (figure 3.19). At this Ir concentration, IrMn can assume two crystallographic phases, i.e. chemically-disordered γ-phase and chemically-ordered $L1_2$-phase (figure 3.1 and table 3.1), which are both antiferromagnetic but induce exchange bias with different characteristics. The two phases have nearly the same lattice constant but can be distinguished by diffraction analysis.

Although deposition by magnetron sputtering generally leads to polycrystalline materials, in this work as-deposited IrMn results to be poorly crystalline, mainly amorphous with some randomly oriented nanocrystalline grains. This is confirmed by the shaded annular pattern detected by plan-view SAD imaging (figure 3.14c) and by plan-view TEM imaging (figure 3.12), which show randomly oriented nanocrystalline grains, with an average grain size of about 5-6 nm. The presence of these nanocrystalline grains is also detected by GID measurements (figure 3.6b) as a relatively small peak at the (111) reflection of IrMn.

During a few days after deposition, the IrMn undergoes a spontaneous crystallization at room temperature, which happens by nucleation and growth of crystallites. The crystallization process is recorded in a sequence of plan-view TEM images (figure 3.13), which show the two-dimensional growth of the crystallites. Since the crystallized IrMn results to be (111) textured, the structural change is also detected by consecutive out-of-plane $\theta/2\theta$ XRD scans (figure 3.5), which reveal a progressive development of the (111) diffraction peak. Since the FWHM of the peak is constant during the crystallization of the IrMn, the possibility that the crystallites develop also along the depth of the film is excluded. As the crystallization propagates among the IrMn layer, the randomly oriented nanocrystalline grains reorient themselves, as shown by plan-view TEM imaging (figure 3.13) and confirmed by the decrease of the IrMn (111) peak in the GID measurements (figure 3.6b).

At the end of the structural transformation, the crystallized IrMn results to be in a chemically-disordered γ-phase, as confirmed by diffraction analysis performed via multiple techniques, namely in-plane $\varphi/2\theta_\chi$ XRD scan (figure 3.9), plan-view SAD imaging (figure 3.16), cross-section SAD imaging (figure 3.17) and HAADF-STEM imaging (figure 3.18). Dark-field imaging of cross-section specimens (figure 3.21) shows grains larger than 100 nm, with extended defects that propagate through the entire thickness of the IrMn layer. The value of 37

nm, estimated using the Scherrer equation on the (220) peak from the in-plane $\varphi/2\theta_\chi$ scan (figure 3.9), is probably due to the presence of these transversal defects which break the crystal order. The crystallized IrMn is strongly textured in the (111) direction, as shown by out-of-plane $\theta/2\theta$ XRD scans (figure 3.5) and both plan-view and cross section SAD imaging (figure 3.14, 3.16, 3.17 and 3.21). XRD rocking curves (figure 3.7) and pole figure measurements (figure 3.8) indicate a rather large out-of-plane mosaicity of about 9°, and a total in-plane mosaicity of 360°.

From the analysis of in-plane $\varphi/2\theta_\chi$ XRD scans (figure 3.9), the Ta seed layer results to be amorphous. XRD characterization of samples without the Ta seed layer, i.e. with the IrMn layer deposited over amorphous Si, shows results equivalent to the generic case. Therefore, when the IrMn crystallizes from an amorphous phase, the Ta seed layer is not necessary for the appearance of a strong (111) texture. The annular signal from the (211) reflection of FeCo present in the plan-view SAD pattern (figure 3.15) indicates that the FeCo layer is polycrystalline with randomly oriented grains. Although the EELS study (figure 3.20) shows that there is no interdiffusion between the sputtered materials, it also detects a prominent roughness at the IrMn/FeCo interface, which might affect the strength of the exchange bias. Structural characterization by XRD and TEM measurements shows that the presence of the FeCo layer does not affect the crystallization of the IrMn, except for the out-of-plane mosaicity (figure 3.10), which is lower in samples without the FeCo layer.

Chapter 4: Magnetic Characterization

The structural characterization presented in chapter 3 showed that, at the deposition conditions employed in this work, the as-deposited IrMn is initially amorphous/nanocrystalline, and it subsequently undergoes a spontaneous crystallization at room temperature, which leads to a highly crystalline γ-phase. In this chapter, the implications of this spontaneous crystallization on the exchange bias of IrMn/FeCo bilayers are studied. The chapter is organized in four sections. The first section includes fundamental information about the phenomenology of the exchange bias, a summary of the theoretical model which is commonly used to predict the effects of exchange bias in polycrystalline samples and a brief description of the measurement protocol employed in this work. In the second section, the magnetic properties of as-deposited samples during the development of the crystallization in the IrMn are studied. The magnetic characterization is performed by combined use of vibrating sample magnetometry (VSM) and magneto-optic Kerr microscopy. The third section focuses on the study of the magnetic properties of the crystallized IrMn/FeCo bilayers. In order to determine the effects of the highly ordered IrMn on the exchange bias, a series of experiments, which combine magnetic characterization by VSM and rigorous annealing and cooling procedures, was performed. The last section summarizes the main results of the extensive magnetic characterization performed in this work.

4.1 Exchange Bias in IrMn/FeCo bilayers

The discovery of exchange bias goes back to 1956, when Meiklejohn and Bean reported for the first time the experimental evidence of this novel magnetic phenomenon [Meiklejohn, 1956]. In 1957, they already elaborated a first theoretical model to explain the existence of the exchange bias, whose predictions were imprecise, but whose fundamentals are still at the basis of the most recent theories [Meiklejohn, 1957]. After more than 60 years, a multitude of exchange-biased systems have been studied and various theories have been elaborated, but a unique theoretical model is still missing. In this scenario, the study presented here is focused on a very specific exchange-biased system, which showed several novel behaviors. The contents of this section are therefore limited to the most relevant information necessary to understand and to interpret the experimental results. A more transversal and detailed

description of exchange bias can be found in the accurate reviews elaborated by Nogués et al. and Berkowitz et al. [Nogués, 1999; Berkowitz, 1999]

4.1.1 Phenomenology of the Exchange Bias

Exchange Bias (EB) is a magnetic interaction which arises when a ferromagnetic (F) and an antiferromagnetic (AF) material are brought in direct contact with each other. This interaction is caused by the direct exchange coupling between spins at the AF/F interface, which induces a unidirectional anisotropy in the magnetic response of the F material [Meiklejohn, 1956]. This phenomenon, whose complexity has prevented the success of a universal theoretical model able to describe all the aspects of this interaction, is characterized by several features. In this section, the main phenomenological properties of the exchange bias are summarized. A schematic diagram of the magnetic response of an exchange-biased system is represented in figure 4.1.

Exchange bias field. The most important phenomenological consequence of the exchange bias consists in the lateral displacement of the ferromagnetic hysteresis loop by an amount called exchange bias field, H_{eb}. In figure 4.1, the exchange bias field is represented by a red arrow. This phenomenon can be intuitively understood assuming a perfect ferromagnetic coupling at the AF/F interface, which aligns the F spins with the next AF spins, as represented in the inset (i) of figure 4.1. As the AF material is affected only by very high magnetic fields, when reversing the external field, the interaction with the rigid AF spins at the interface exerts a torque on the F spins, trying to keep them in their original direction (inset (ii) of figure 4.1). Hence, the external field necessary to completely reverse the F material is increased by the value of the exchange interaction at the interface (inset (iii) of figure 4.1). When inverting the external field to the original direction, the torque exerted by the AF spins promotes the switching of the F spins, therefore the reversal of the F material requires a lower external field (inset (iv) of figure 4.1).

Coercivity enhancement. The coercivity, H_c, of a magnetic material is defined as the half width of its hysteresis loop when the magnetization is zero, as shown by the green arrow in figure 4.1. In an exchange-biased system, the hysteresis loop is characterized by a higher coercivity compared to the sole F material. This effect can be explained by assuming that only some of the AF spins at the interface are strongly pinned and therefore contribute to the loop shift during the reversal, while the majority of them can rotate with the F layer [Ohldag, 2003;

Wu, 2010; Zhou, 2015]. The irreversible switching of these rotatable spins is likely behind the increased coercivity in exchange-biased systems [Fulcomer, 1972b].

Reversal asymmetry. In most of the studies on exchange-biased systems, the ascending and descending branches of the hysteresis loop are not symmetric. This asymmetry is the result of different magnetization reversal processes which take place in the exchange-biased F layer when cycling the external magnetic field. Camarero et al. showed that the non-symmetric reversal of the hysteresis loop is intrinsic to exchange-biased systems and it arises when the alignment of the external field with the sample anisotropy is not perfect [Camarero, 2005]. In addition, reversal asymmetry can be caused by various factors such as easy axis dispersion or non-perfect collinearity between uniaxial and unidirectional anisotropy in the F layer.

Training effect. Variations of the hysteresis loop upon repeated field cycling in exchange-biased systems are commonly referred as training. This magnetic aftereffect is particularly significant in polycrystalline samples and it has been object of many studies in the last decades [Nogués, 1999]. The term "training effect" usually includes two different types of aftereffect, which can be referred as athermal and thermal training [Fernandez-Outon, 2006]. The athermal training consists in an important variation of the loop shape which takes place between the first and the second field cycle. An evident consequence of this variation is a considerable lowering of both the exchange bias field and the coercivity after the first loop cycle. The athermal training is suspected to be due to irreversible changes in the AF microstructure during magnetization reversal [Hoffmann, 2004] and it can be removed by cycling the external field before measuring. The thermal training, instead, consists in the progressive decrease of the exchange bias field upon field cycling. This decrease was found to scale with $1/\sqrt{N}$, where N indicates the number of field cycles [Paccard, 1966; Nogués, 1999]. This type of training is believed to be caused by thermal activation of the AF grains during field cycling [Fernandez-Outon, 2006] and it can be removed by measuring at sufficiently low temperatures [Polisetty, 2007].

Blocking temperature. The lateral displacement induced by the exchange anisotropy depends strongly on the temperature at which the hysteresis loop is measured. In fact, the exchange bias field, H_{eb}, decreases as the temperature is increased and it eventually reaches zero at a value called the blocking temperature, T_B, which is often lower than the Néel temperature, T_N, of the AF material [Nogués, 1999]. The origin of this effect is found in the thermal fluctuation of the antiferromagnetic grains, which can reorient their magnetic orientation upon increasing the

temperature. Since this thermal effect depends on the volume of the AF grains present in the sample, systems with large grain size generally have $T_B \sim T_N$, while typical polycrystalline systems can show very low T_B [O'Grady, 2010].

Interfacial exchange energy, J_K. The interfacial exchange energy represents the strength of the exchange bias and can be evaluated using the phenomenological formula

$$J_K = M_s d_F H_{eb}, \qquad (4.1)$$

where M_s and d_F are respectively the saturation magnetization and the thickness of the F material, and H_{eb} is the exchange bias field [Berkowitz, 1999]. The interfacial exchange energy is commonly used for comparisons of the effectiveness of exchange bias among samples with different materials and thicknesses.

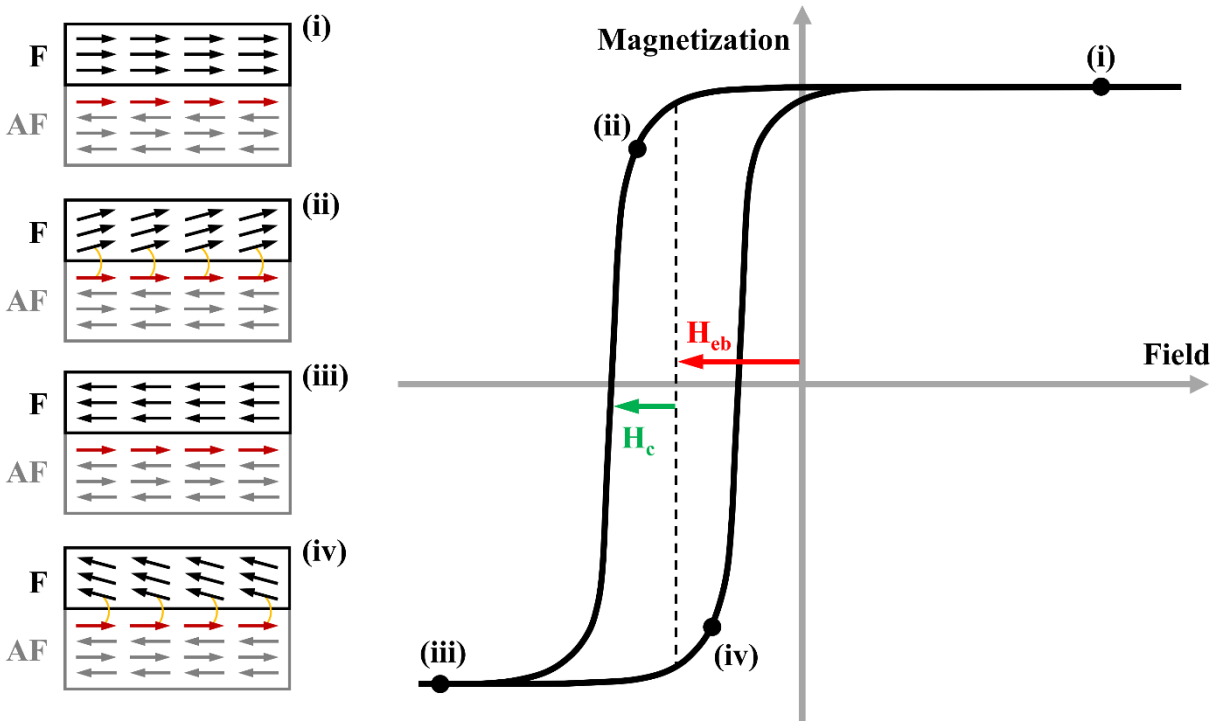

Figure 4.1: Schematic diagram of the hysteresis loop of an exchange-biased system.

Exchange bias setting. To exhibit exchange bias, AF/F bilayers must undergo a thermal treatment which is generally called the exchange bias setting. This setting process consists in either field cooling from above the Néel temperature of the AF material, or field annealing at temperatures above T_B [Nogués, 1999]. The presence of the external field during the EB setting is not a necessary condition to produce exchange bias. In fact, it is the exchange interaction between the F and the AF spins at the interface what induces the exchange bias during the setting, and not the external field [Takahashi, 1980]. However, it is well known that the

exchange bias field increases considerably upon setting the exchange bias in presence of a high magnetic field, as shown by Fernandez-Outon et al. [Fernandez-Outon, 2008]. In most systems, including IrMn/FeCo bilayers, the loop shifts in the opposite direction to the setting external magnetic field. Nonetheless, a shift in the same direction of the setting field has also been observed in some systems [Nogués, 2000].

4.1.2 Theory of the Exchange Bias: the granular model

Since its discovery in 1956 [Meiklejohn, 1956], exchange bias has been detected in a large variety of systems, including nanoparticles [Vasilakaki, 2015], core-shell nanowires [Proenca, 2013], bulk Heusler alloys [Sharma, 2015], epitaxially grown materials [Zhang, 2016] and polycrystalline thin films [Meinert, 2015], and in many different combinations of AF and F materials [Nogués, 1999; Sharma, 2017]. Over more than 60 years, much effort has been made to explain and predict the complexity of the phenomenon, and several models have been proposed. However, a unique theory valid for different systems that can account for all the features of the exchange bias has not been found yet. This is mainly due to the fact that direct observation of the spins arrangement of an antiferromagnetic material in a multilayered system is extremely challenging, and therefore theoretical models must rely on a priori assumptions most of the times. Examples of these assumptions are the grade of compensation of the AF spins at the AF/F interface [Néel, 1967], the formation of domains in the AF material [Nowak, 2002], a spin-flop coupling at the AF/F interface [Koon, 1997], and the presence of partial domain walls in the AF, either parallel [Mauri, 1987] or perpendicular to the sample surface [Malozemoff, 1987]. A brief description of the most successful theories proposed over the years can be found in ref. [O'Grady, 2010].

The complexity of this phenomenon is enhanced by the intrinsic differences of the systems under consideration. For instance, while one can expect the formation of domains in an epitaxially deposited AF thin film, polycrystalline samples are more likely to be formed by small, single-domain AF grains. On the other hand, the interface roughness, which depends on the deposition technique, is likely to affect the grade of compensation of the AF spins. It is therefore evident that the elaboration of a theory that can account for all these study cases is not an ordinary challenge. Hence, the attempts to predict or explain the behavior of exchange-biased systems, both qualitatively and quantitatively, must rely on the most appropriate theoretical model, depending on the type of structure, the deposition technique, the materials

used and the crystallography of the system. As this work is focused on the IrMn/FeCo system deposited by magnetron sputtering, which is known to be polycrystalline with small IrMn grains [O'Grady, 2010], the initial interpretation of the magnetic results given in this chapter is based on the granular model of the exchange bias.

The first model for the exchange bias was developed in 1957 by Meiklejohn and Bean to describe the magnetic behavior of fine particles of cobalt covered by an AF cobaltous oxide shell [Meiklejohn, 1957]. According to their model, when the system is cooled below the Néel temperature of the AF material, T_N, the AF spins at the interface align ferromagnetically with the F spins, driven by direct exchange coupling. This implies the formation of a perfectly uncompensated AF spin structure at the interface, which remains rigidly aligned along its easy axis when the F layer is reversed by a saturating external field (see figure 4.1). Although such a simple model is able to explain the typical loop shift present in exchange-biased systems, it fails to predict the right magnitude of the exchange bias field, which is overestimated by two orders of magnitude. More importantly, being based on the rigid pinning of the AF spins below T_N, the model of Meiklejohn and Bean ignores possible thermal fluctuations in the system and therefore it failed to predict the temperature dependent behavior of exchange bias.

Early after the discovery of the exchange bias, the experimental studies of Jacobs and Kouvel revealed the presence of magnetic aftereffects in mixed manganites showing exchange bias [Jacobs, 1961]. A magnetic aftereffect consists in a delayed change in the magnetization of the sample after the application of a magnetic field, according to the definition given by Chikazumi [Chikazumi, 1997]. In their work, Jacobs and Kouvel showed that the magnitude of the exchange bias field depends on the duration of the measurement. They observed differences in the hysteresis loops measured dynamically and quasi-statically and they addressed this behavior to thermal fluctuation aftereffects in the AF material. In addition to this, the temperature dependent studies of Hagedorn on oxidized FeNi films [Hagedorn, 1967] and Schlenker on oxidized Co films [Schlenker, 1968] revealed that the exchange bias field decreases with increasing temperature, and eventually vanishes at a blocking temperature, T_B, lower than T_N. These temperature dependent properties of the exchange bias in polycrystalline materials highlighted the necessity of a theoretical treatment which considered thermal fluctuations in the AF material.

Such a theoretical treatment was developed in 1972, when Fulcomer and Charap published two studies in which they proposed the first granular model for the exchange bias [Fulcomer, 1972a;

Fulcomer, 1972b]. The first article reported their experimental studies on exchange bias in partially oxidized FeNi thin films, obtained by exposing vacuum deposited FeNi to acid vapor [Fulcomer, 1972a]. The progressive oxidation of the nickel in the FeNi alloy produced isolated antiferromagnetic NiO grains, ideal for the comparison of the experimental results with the granular model for the exchange bias developed in the second study. The experiments consisted in measuring the dependence of the exchange bias field and coercivity of the hysteresis loop on the temperature and field cycling frequency, i.e. the time of measurement, while varying the grade of nickel oxidation, i.e. the size of the AF grains. In agreement with the studies of Hagedorn and Schlenker, they found that the loop displacement decreases with increasing temperature and that the blocking temperature, T_B, depends on the amount of film oxidation. They also showed that the loop displacement increases, whereas the coercivity decreases, with increasing field cycling frequency. These experiments unequivocally demonstrated a relation between the AF grains volume and the temperature dependent properties of exchange bias.

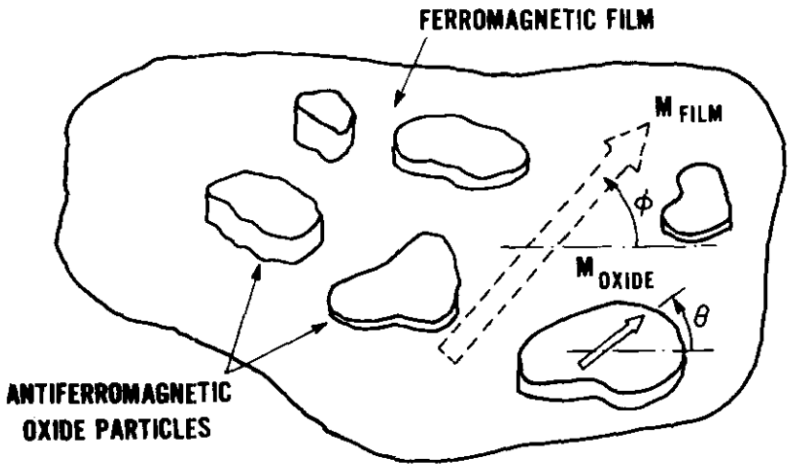

Figure 4.2: Schematic diagram of the isolated antiferromagnetic particles coupled to the underlying ferromagnetic film, after [Fulcomer, 1972b].

In Fulcomer and Charap's theoretical study [Fulcomer, 1972b], the exchange-biased system is modelled as an assembly of non-interacting single-domain AF particles, which are exchange coupled to a F film. A schematic representation of the Fulcomer and Charap's model is presented is figure 4.2. Each AF grain is assumed to have an uncompensated net surface moment, **m**, at its interface with the F film. The AF particles have uniaxial anisotropy and the angle between **m** and the AF easy axis is indicated with θ. The F film has uniaxial anisotropy as well, and its magnetization makes an angle φ with the F easy axis. Since the field is applied

along the F easy axis, φ is assumed to be either 0° or 180°. Hence, assuming that the easy axes of an AF particle and the F film coincide, the total energy for such a particle can be written as

$$E_{AF} = K_{AF}V_{AF}\sin^2\theta - J_{ex}S_{AF}^{eff}\cos(\theta - \varphi), \qquad (4.2)$$

where K_{AF} is the uniaxial anisotropy constant for the antiferromagnet, V_{AF} is the volume of the AF particle, J_{ex} is the interface exchange coupling constant, S_{AF}^{eff} is the effective surface involved in the exchange interaction, which also depends on the grade of compensation of the spins at the interface. The first term of equation 4.2 represents the uniaxial anisotropy energy for the AF particle. This energy term implies two equivalent stable levels for the system, which correspond respectively to the energy minima at $\theta = 0°, 180°$. The second term represents the exchange energy given by the coupling with the F film. The direction of magnetization of the F film, indicated by the value of φ, determines the sign of the cosine in the exchange coupling term in equation 4.2, and therefore promotes one of the two levels by lowering its energy value with respect to the other one. When the condition $2K_{AF}V_{AF} > J_{ex}S_{AF}^{eff}$ is satisfied, equation 4.2 describes an asymmetric two-energy-levels system, whose energy E_{AF} is plotted as a function of θ and φ in figure 4.3.

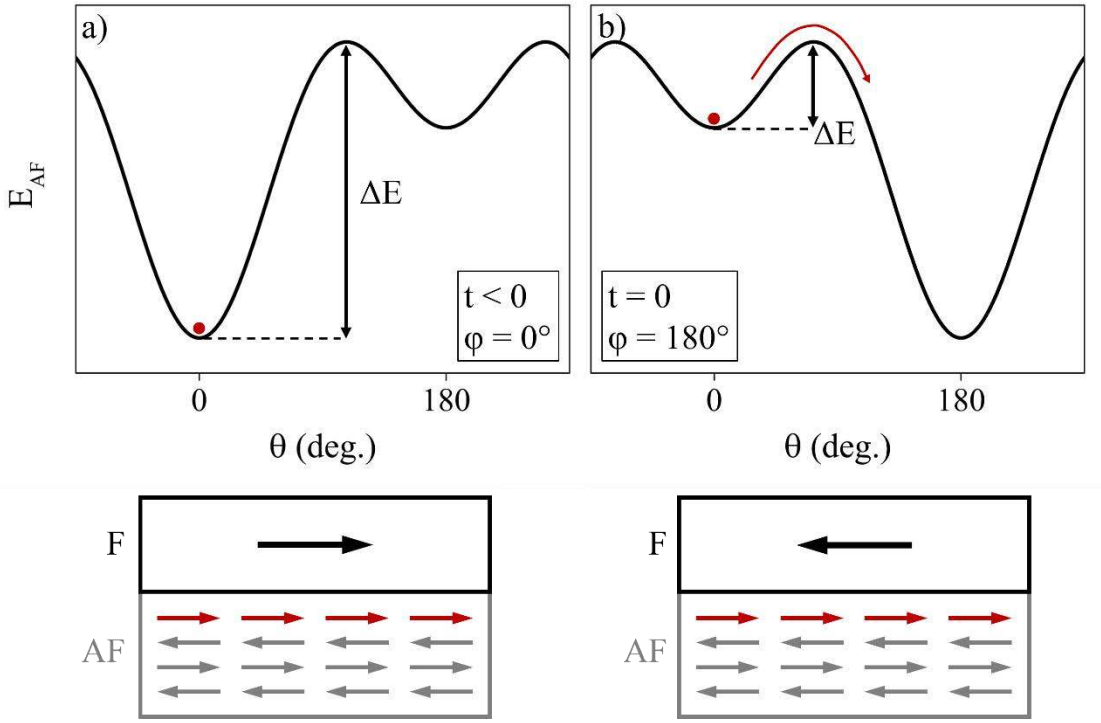

Figure 4.3: Schematic diagram of the asymmetrical two-energy-levels system described by equation 4.2, for a) $\varphi = 0°$ and b) $\varphi = 180°$.

According to the Fulcomer and Charap's theory, when the F magnetization is switched, the AF particles can reverse their magnetic orientation, driven by the exchange interaction between the surface moment, **m**, and the F magnetization. Figure 4.3 shows the energy state E_{AF} as a function of θ for a single AF particle described by equation 4.2, before and after the reversal of the F magnetization. For $t < 0$, the surface moment of the particle, **m**, represented by the red arrows, is oriented so that $\theta = 0°$. The F magnetization is parallel to **m**, so that $\varphi = 0°$. Therefore, the particle lays at the global energy minimum, as shown by the red dot in figure 4.3a. At time $t = 0$, the F magnetization is reversed, i.e. $\varphi = 180°$, and the potential energy of the particle changes (figure 4.3b). Now the particle lays at a local energy minimum, and if it is provided with a sufficient amount of thermal energy, $k_B T$, it can switch its surface moment, **m**, to the more favorable energy state at $\theta = 180°$ by overcoming the energy barrier, ΔE.

This simplified description allowed Fulcomer and Charap to treat the problem through a statistical approach, by considering the thermal fluctuation of the AF particles. Considering an ensemble of non-interacting identical AF particles, when the magnetization of the F film is reversed, the thermal fluctuation of the particles leads to the progressive reversal of the total surface moment of the AF material, described by

$$m(t) = m_0[2\exp(-t/\tau) - 1], \qquad (4.3)$$

where m_0 represents the initial surface moment, t is the time and τ is the characteristic relaxation time, which can be described as a function of the energy barrier, ΔE, by the Néel-Arrhenius law

$$\tau^{-1} = f_0 \exp\left[-\frac{\Delta E}{k_B T}\right], \qquad (4.4)$$

with f_0 being the characteristic attempt frequency, k_B being the Boltzmann constant and T being the temperature. Hence, the relaxation time of the AF material depends exponentially on T, which explains the behavior of the exchange bias field as a function of the temperature. In fact, at high temperatures, for which the relaxation time is very small, the AF surface moment could relax faster than the experiment itself, resulting in a centered hysteresis loop. The blocking temperature, T_B, is therefore defined as the temperature at which the relaxation time equals the experimental time. Also, it is evident that at a fixed temperature, changing the experimental time would result in different magnetic response, which explains the dependence of the exchange bias on the field cycling frequency. The calculations performed by Fulcomer and Charap, considering a distribution of particle sizes and shapes, fitted well to the collected

data, which grants the goodness of the granular model for the description of exchange bias in polycrystalline films.

The Fulcomer and Charap's theory was also used to explain the reversal of the exchange bias reported by van der Heijden et al. in their work about the thermal stability of FeMn- and NiO-based exchange-biased bilayers deposited by magnetron sputtering [van der Heijden, 1998]. They studied the progressive relaxation of the exchange bias field as a function of time, during a forced antiparallel alignment of the magnetization of the F layer and the net uncompensated moment of the AF layer, which induces the exchange bias. This relaxation, which was shown to be faster at higher temperatures, eventually led to an inversion in the direction of the exchange bias. Van der Heijden et al. successfully explained the results obtained by applying the granular model for the exchange bias developed by Fulcomer and Charap.

4.1.3 The York Protocol

An important consequence of the thermal activation of polycrystalline AF materials, also predicted by the Fulcomer and Charap's theory, is the possibility to establish a strong exchange bias at temperatures below T_N. This is crucial for technological applications, as exchange bias can be set in materials with high Néel temperature without causing atomic interdiffusion within the multilayers, that would adversely affect the performance of the devices. It is the case of IrMn, the material of choice for all current applications based on EB, which has a Néel temperature of 690 K, but can be set to induce a strong exchange bias by field annealing at temperatures of about 500 K. On the other hand, the study performed by Fulcomer and Charap revealed a scenario in which the loop displacement caused by the exchange bias depends not only on the structural and magnetic properties of the AF material, but also on a series of additional factors such as the temperature and the duration of the measurement, the magnetic history of the samples, the conditions at which the EB is set, the AF grains size distribution, the thickness and the anisotropy of the AF layer, the density of uncompensated spins at the AF/F interface and its roughness. Such complexity entails a series of non-controllable variables when performing magnetometry measurements, which prevents the effective comparison between experimental studies based on different characterization procedures. It is in this scenario that the research group led by Prof. O'Grady from the University of York, published a series of studies in which they established a protocol to perform magnetic measurements on exchange-biased bilayers, which grants the reproducibility of the results [O'Grady, 2010].

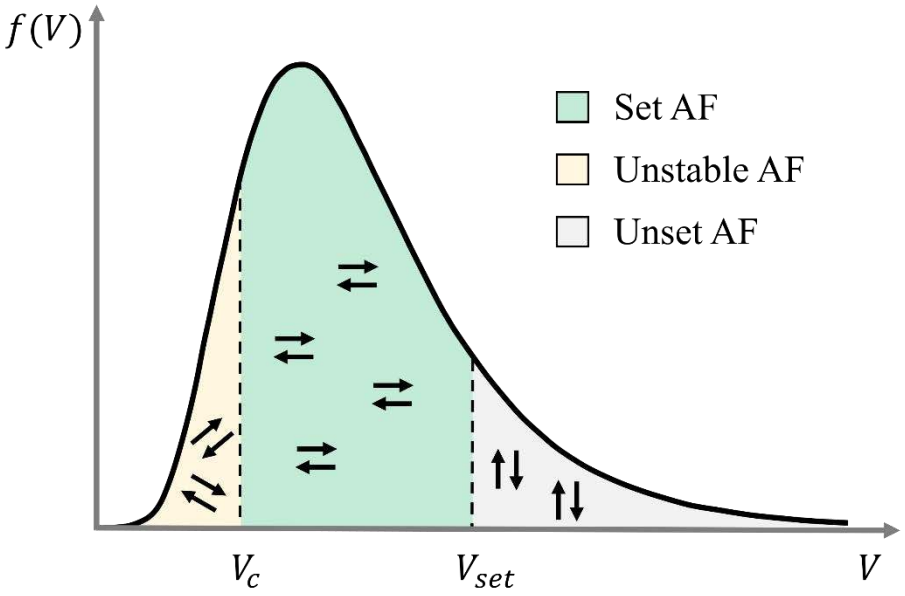

Figure 4.4: Schematic diagram of the volume distribution of IrMn grains in sputtered polycrystalline material; the two critical volumes determine the fraction of the material which contributes to the EB.

The York Protocol consists in a precise sequence of magnetic measurements combined with a specific procedure of field annealing and cooling, which allows to control the state of order in the AF layer. It is based on considerations about the energy barrier distribution of single-domain AF grains, according to the granular model of Fulcomer and Charap. They showed that for thin F layers, the energy barrier, ΔE, in equation 4.4 can be approximated to the product $K_{AF}V_{AF}$, with K_{AF} being the uniaxial anisotropy constant for the antiferromagnet and V_{AF} the volume of the AF grain [Vallejo-Fernandez, 2008a]. Hence, the energy barrier distribution reflects the volume distribution of the AF grains, which they managed to measure by TEM characterization and to control by depositing their samples with a sputtering equipment which allows to vary the grain size of the deposited thin film [Vopsaroiu, 2005]. A schematic representation of the typical lognormal distribution for the grains volume in a sputtered polycrystalline material is shown in figure 4.4. They identified two critical volumes for the AF grains in exchange-biased samples [Vallejo-Fernandez, 2008b]. The critical setting volume, V_{set}, corresponds to the largest grain volume that can be magnetically reoriented by thermal activation during an initial field annealing of duration t_{set}, at temperature T_{set}. The AF grains with $V > V_{set}$ are not aligned with the F layer and therefore do not contribute to the exchange bias. The critical activation volume, V_c, corresponds to the largest grain volume that can be magnetically reoriented by thermal activation during the magnetometry measurement, taken at temperature T_{ms} in a time t_{ms}. The AF grains with $V < V_c$ are thermally unstable and therefore change their magnetic orientation during the measurement, giving no net contribution to the

exchange bias. Hence, only the AF grains with volume between V_c and V_{set}, indicated by the green area in figure 4.4, are responsible for the exchange bias field. It is evident that the choice of both temperatures and timescales affects the amount of AF volume which actively contributes to the exchange bias, and consequently influences the value of H_{eb}.

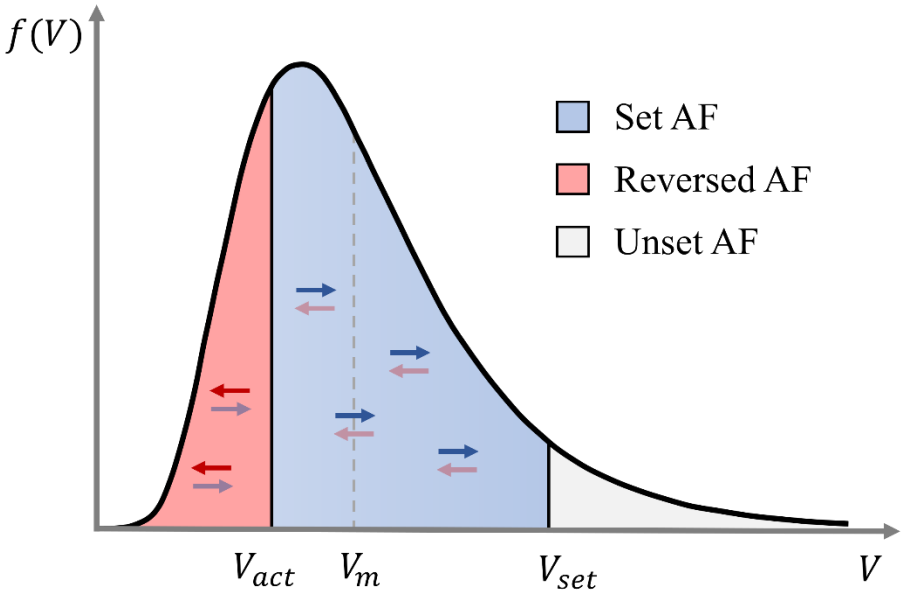

Figure 4.5: Schematic diagram of the volume distribution of IrMn grains in sputtered polycrystalline material; the two colored areas delimited by V_{act} contribute oppositely to the exchange bias; the median of the distribution is indicated by the gray dashed line.

The York Protocol aims to remove any experimental ambiguity from the results and to maximize the amount of AF volume which contributes to the exchange bias. The measurement procedure involves four steps, whose effects are shown in figure 4.5 [O'Grady, 2010]. Firstly, the sample undergoes the initial setting of the exchange bias, which consists in a field annealing of duration t_{set} = 90 min, at the maximum temperature T_{set} which does not result in interfacial diffusion. Then, the hysteresis loop is measured at the non-activation temperature, T_{NA}, which is the highest temperature at which there is no thermal activation of the AF grains, so that the measurements are not subject to timescale effects. These first two conditions grant that the fraction of the AF volume which contributes to the exchange bias is the highest achievable (colored area in figure 4.5). The third part consists in the controlled activation of the AF layer, which is achieved by a field annealing of duration t_{act} = 30 min at increasing temperature T_{act}, in presence of a saturating reversed magnetic field. The consequence of this activation is that the AF grains with volumes $V < V_{act}$ reverse their magnetic orientation and therefore contribute to the exchange bias in the direction opposite to the original setting (red area in figure 4.5). Then, the hysteresis loop is measured again at T_{NA} and the resulting exchange bias field

corresponds to the difference between the contributions from the AF grains with $V > V_{act}$ (blue area in figure 4.5) and the ones with $V < V_{act}$ (red area in figure 4.5). The procedure is repeated for various values of T_{act}, and the resulting exchange bias field, H_{eb}, is then plotted as a function of T_{act}.

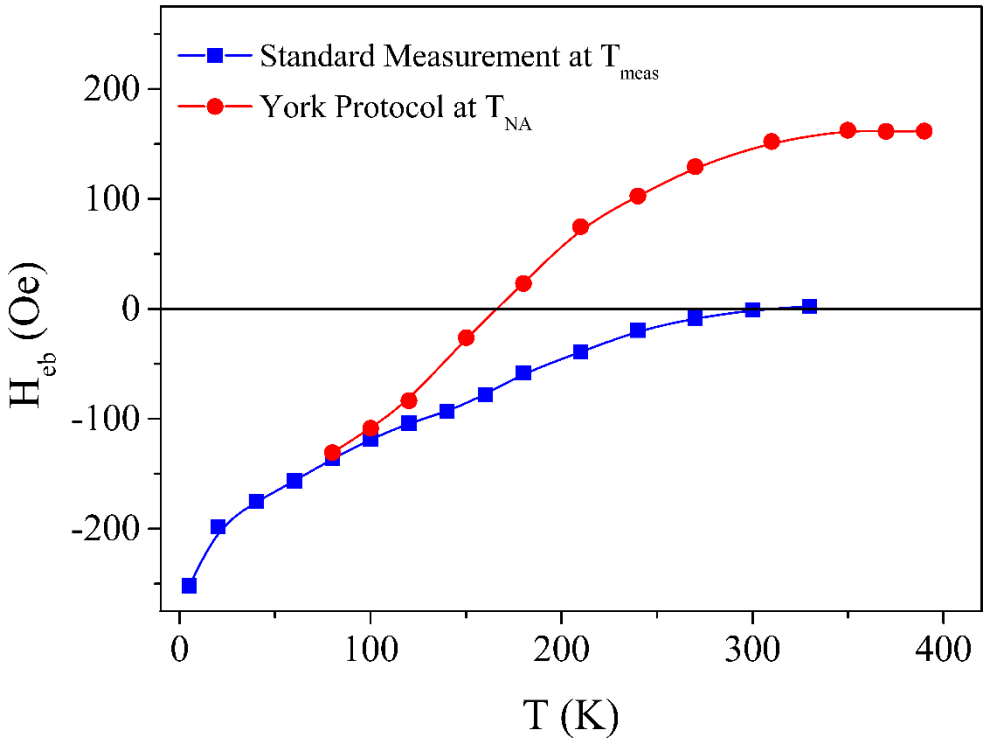

Figure 4.6: Exchange bias field measured following the York Protocol and measured via standard procedure. Solid lines are a guide to the eye. After [O'Grady, 2010].

This procedure to evaluate the effects of the thermal activation of AF volumes on the exchange bias is intrinsically different from the conventional measurement of the blocking temperature. A comparison between the blocking temperature curves measured by the York Protocol (H_{eb} vs T_{act}) and the traditional method (H_{eb} vs T_{ms}) is shown in figure 4.6. The conventional blocking temperature curve is derived by measuring the hysteresis loop at increasing temperature, T_{ms}. The value of the exchange bias field decreases with increasing T_{ms}, until it eventually reaches zero at the blocking temperature, T_B. Hence, the conventional blocking temperature is defined as the temperature at which all the AF grains with volume $V < V_{set}$ are thermally active during the measurement time t_{ms}. On the other hand, when following the procedure defined by the York Protocol, the system is free of thermal activation during the measurement and the value of the exchange bias field can be controlled by increasing T_{act}, and

eventually reversed completely [Fernandez-Outon, 2004], in agreement with the studies performed by van der Heijden et al. [van der Heijden, 1998]. The activation temperature at which the exchange bias field goes to zero is called the median blocking temperature, $<T_B>$, and it corresponds to the situation in which the contributions to the exchange bias from the set AF volume and the reversed AF volume cancel out, i.e. when V_{act} equals the median volume, V_m [Vallejo-Fernandez, 2007].

The introduction of the concept of median blocking temperature allowed Vallejo-Fernandez et al. to determine the value of the anisotropy of the antiferromagnetic layer, K_{AF}, directly from the measurements performed following the York Protocol [Vallejo-Fernandez, 2007]. In fact, the controlled thermal activation of the AF layer for a time t_{act} at the median blocking temperature, $<T_B>$, reverses a fraction of the AF volume corresponding to the median of the volume distribution, V_m. Since the volume distribution can be measured by TEM characterization, all these three variables, t_{act}, $<T_B>$ and V_m, can be known and, according to the approximation $\Delta E = K_{AF}V_{AF}$, the anisotropy of the antiferromagnetic layer, K_{AF}, can be derived by rearranging equation 4.4 as

$$K_{AF}(\langle T_B \rangle) = \frac{\ln(t_{act} \cdot f_0)}{V_m} k_B \langle T_B \rangle. \qquad (4.5)$$

As its origin is magneto crystalline, K_{AF} is temperature dependent and the dependency is assumed to follow a relation of the form

$$K_{AF}(T) = K_{AF}(0) \cdot (1 - T/T_N). \qquad (4.6)$$

From these considerations, Vallejo-Fernandez et al. could determine the value of $K_{AF}(T)$ for their samples. Finally, they could rearrange again equation 4.4 to find a generic expression for the critical volume

$$V(T,t) = \frac{\ln(tf_0)}{K_{AF}(T)} k_B T, \qquad (4.7)$$

which depends only on a set of time and temperature, (T, t). Therefore, the critical volumes defined in figure 4.4 can be found as $V_{set}(T_{set}, t_{set})$ and $V_c(T_{ms}, t_{ms})$. Since the exchange bias field is proportional to the integral of the volume distribution between V_{set} and V_c, they could successfully predict the dependence of the exchange bias on both the grain size and the thickness of the AF layer.

4.2 Exchange Bias formation

The structural characterization of as-deposited IrMn/FeCo bilayers presented in chapter 3 showed the spontaneous crystallization of the IrMn layer, without the need of post-deposition treatments. This section covers the study of the magnetic behavior of as-deposited IrMn/FeCo bilayers, during the development of the crystallization in the IrMn. The magnetic characterization presented in this section shows that the exchange bias, which is initially absent in as-deposited samples, progressively develops as the crystallization of the IrMn propagates. This peculiar formation of the EB was studied by combined use of vibrating sample magnetometry and magneto-optic Kerr microscopy.

4.2.1 Magnetometry

In order to study the effect of the phase transformation of the IrMn on the magnetic behavior of IrMn/FeCo bilayers, magnetic characterization was performed by vibrating sample magnetometer (VSM). Magnetometry measurements of the same AF/F-type sample whose XRD out-of-plane $\theta/2\theta$ scans are presented in figure 3.5, were taken before and after performing the structural characterization. Figure 4.7 shows the results for both the magnetic and structural measurements. The red curve in figure 4.7a is the hysteresis loop of the as-deposited sample, taken within half an hour after the sample deposition. The sample was then taken to the diffractometer for immediate structural characterization. The red diffractogram of figure 4.7b shows that at this stage the crystallization of the IrMn layer had not triggered yet. The magnetometry response is characterized by a perfectly centered hysteresis loop with a coercivity of about 20 Oe, whose value agrees with the soft magnetic properties of FeCo thin films with small mean grain size (i.e. less than 10 nm) [Vopsaroiu 2005]. The absence of both loop shift and coercivity enhancement indicates that the FeCo layer is not exchange biased with the amorphous/nanocrystalline IrMn.

Once the crystallization of the IrMn was completed, as confirmed by the blue diffractogram in figure 4.7b, the sample was taken to the VSM for further magnetic characterization. The magnetic response, represented by the blue curve in figure 4.7a, shows that during the structural characterization the sample developed an exchange bias characterized by a loop shift of the order of 600 Oe and a coercivity of about 75 Oe. Assuming a saturation magnetization $M_s = 1.7\ emu/cc$ for the $Fe_{40}Co_{60}$ layer [Lahtinen, 2012], the interfacial exchange energy can be

calculated using equation 4.1, which gives $J_K = 0.51\ erg/cm^2$ for $d_F = 5\ nm$ and $H_{eb} = 600\ Oe$, which agrees with the values found by Tsunoda et al. for IrMn/FeCo bilayers with chemically disordered γ-IrMn [Tsunoda, 2006]. The combined results of the magnetic and structural characterizations summarized in figure 4.7 suggest that the development of the exchange bias is caused by the phase transformation of the IrMn.

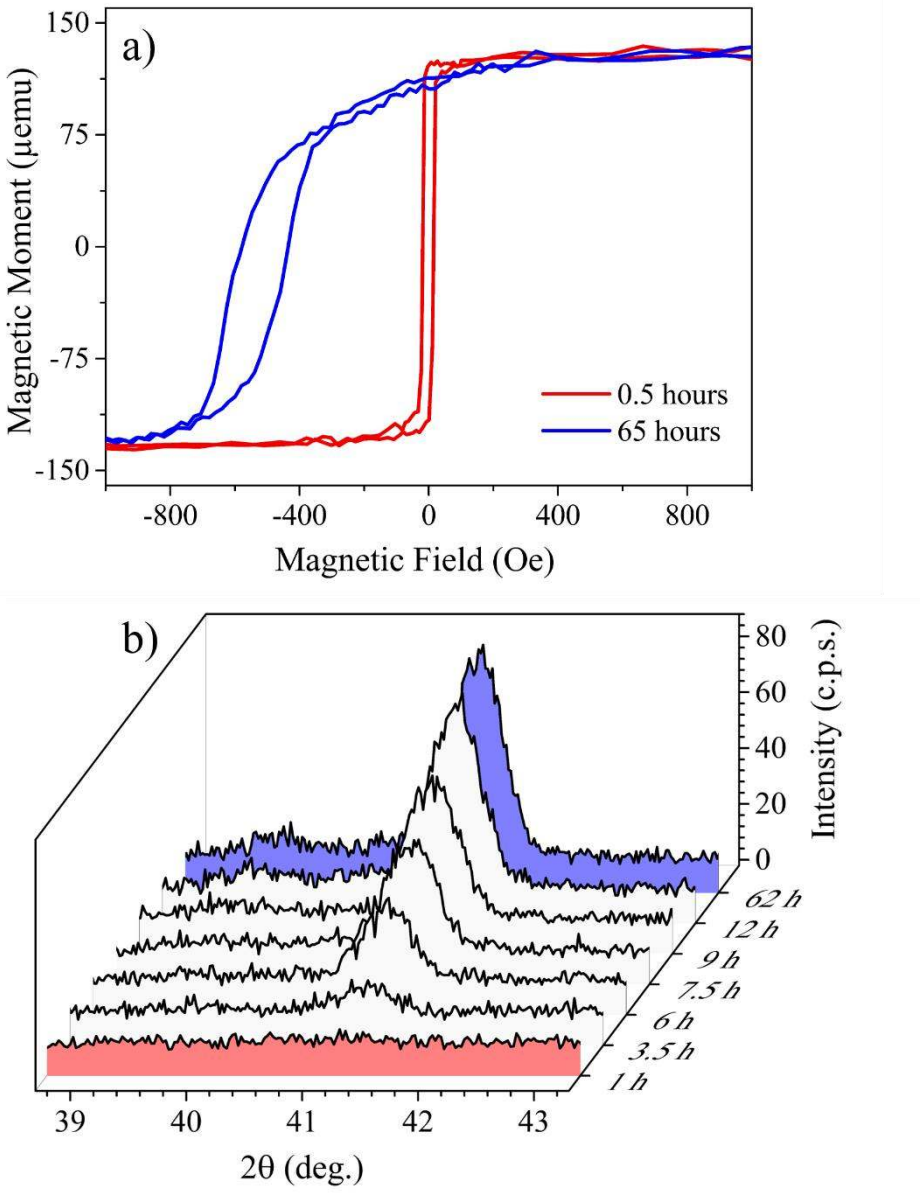

Figure 4.7: a) Magnetometry measurements performed before and after the structural characterization; b) XRD out-of-plane $\theta/2\theta$ scans during the structural transformation of the IrMn.

To our knowledge, there are only two cases of spontaneous increase of the exchange bias field at room temperature reported in the scientific literature. Both the works of Paetzold et al. and Thomas et al. showed the spontaneous increase of the exchange bias field in NiO/NiFe bilayers

[Paetzold, 2002; Thomas, 2003]. Their as-deposited samples showed small or none exchange bias, but very large coercivity (40-120 Oe) with respect to the value of soft FeNi films (2-3 Oe). At room temperature and in absence of applied field, the samples showed a progressive shifting of the entire hysteresis loop towards higher values of exchange bias field, according to the direction of the remanent magnetization of the FeNi layer. The increase of the exchange bias field was logarithmic with time and it was temperature dependent, which suggests that this self-developing exchange bias is the result of a thermal activation process in the AF layer. However, the absence of structural information does not allow to rule out the possible role of structural transformations in the as-deposited samples.

In order to characterize the development of the exchange bias during the crystallization of the IrMn, an AF/F-type sample with structure SL/IrMn(15nm)/FeCo(5nm)/CL, i.e. equivalent to the one of figure 4.7, was deposited and immediately taken to the VSM for magnetic characterization. Magnetometry measurements were repeated every 2 hours over a period of a few days, during which time the sample was always kept at room temperature. Since no external field was applied between consecutive measurements and considering that each measurement took about 20 minutes, the sample was magnetically unperturbed for about 85% of the time. The result of this magnetic characterization is presented in figure 4.8, where a selection of the hysteresis loops measured at different times are superimposed.

The evolution of the hysteresis loop, which describes the progressive development of the exchange bias, is peculiar and intrinsically different from the two cases of room temperature developing exchange bias studied in the past [Paetzold, 2002; Thomas, 2003]. In fact, instead of a progressive shifting of the entire hysteresis loop toward higher values of exchange bias field, the development of the exchange bias seems to be the result of two different processes. Initially, the hysteresis loop experiences a peculiar deformation in which part of the loop remains centered and unaltered, whereas the remaining part is laterally shifted. This bifurcated loop indicates that a well-defined portion of the FeCo layer is exchange biased, whereas the remaining part can switch freely with the external field. As time passes, the amount of the hysteresis loop which shows exchange bias increases, while the centered part of the loop decreases proportionally. This evolution of the hysteresis loop seems to be the result of a progressive expansion of the exchange-biased portion of the FeCo layer, at the expenses of the non-exchange-biased part. Concurrently, the portion of the hysteresis loop which shows exchange bias shifts laterally with time, increasing the exchange bias field. This increase,

which is particularly evident between the blue and the green curves in figure 4.8, continues for few days after the exchange bias is completely developed.

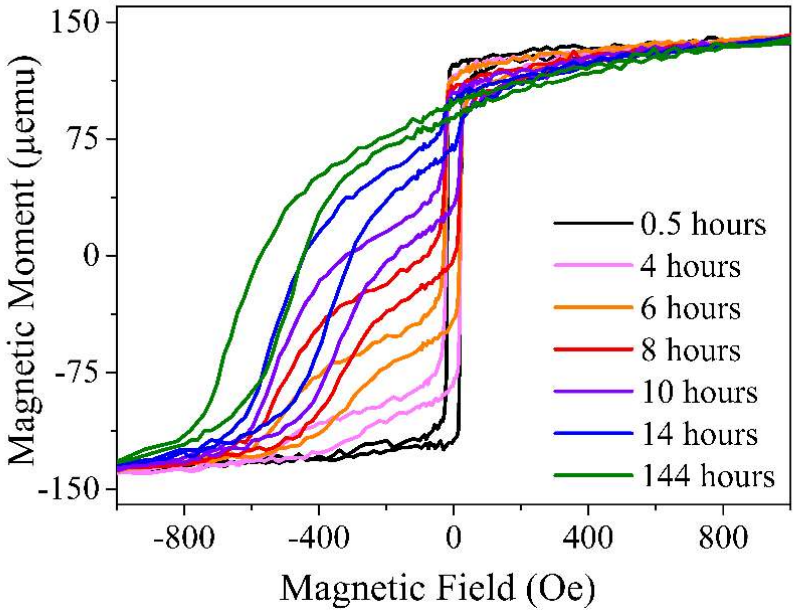

Figure 4.8: Evolution of the hysteresis loop during the structural transformation of the IrMn

The formation of the exchange bias shown in figure 4.8 can be directly related to the crystallization of the IrMn, whose structural characterization is presented in chapter 3. In the as-deposited sample, the initially amorphous/nanocrystalline IrMn induces no exchange bias on the ferromagnetic FeCo. Hence, the FeCo layer is initially free to switch and no loop shift nor enhanced coercivity are detected in the magnetometry measurement. When the crystallization triggers, the FeCo which lies directly above the crystalline IrMn becomes exchange biased, while the remaining part of the FeCo layer is still free to switch with the external field. As the crystalline phase propagates across the IrMn layer, it induces exchange bias on an increasing portion of the FeCo layer, until it eventually covers the entire surface. As introduced in section 4.1.1, it is the direction of magnetization of the F layer what defines the direction of the exchange bias upon setting. In the experimental batch which led to the data shown in figure 4.8, at the end of every measurement the external field was brought to zero from positive values, so that the sample was always left in its positive remanent state between measurements. Accordingly, figure 4.8 shows that, as the crystallization develops, the FeCo layer gets progressively exchange biased in the same direction. On the other hand, the increase of the exchange bias field with time seems to be independent of the formation of the exchange

bias driven by the phase transformation in the IrMn and might be influenced by several factors. A detailed discussion about this phenomenon can be found in section 5.3.

4.2.2 Kerr Microscopy

To further characterize how the exchange bias develops during the crystallization of IrMn, magneto-optic Kerr microscopy measurements were taken at different stages during the formation of the exchange bias. Kerr microscopy is sensitive to the Kerr rotation induced by the local magnetic moment of the sample on the polarization of the reflected light, therefore it is capable to detect the magnetic domains of ferromagnetic materials. With the use of Kerr microscopy, it was possible to characterize the exact development of the exchange bias induced by the crystallization of the IrMn.

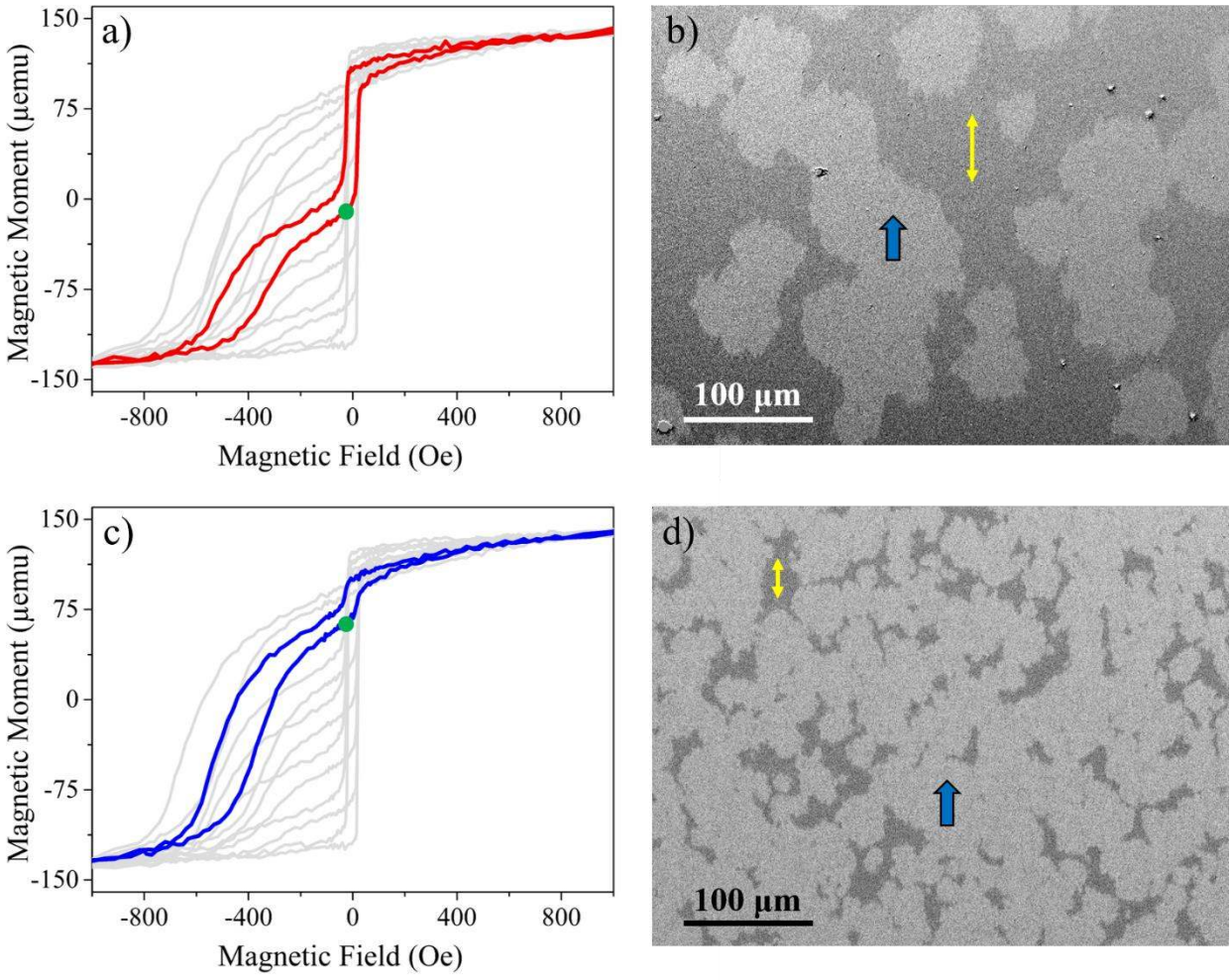

Figure 4.9: Magnetometry measurements and corresponding Kerr images taken at different stages of the exchange bias formation.

Figure 4.9 shows paired magnetometry measurements and Kerr images taken at two different stages of the exchange bias formation, respectively 50% and 80% of the process completion. Both Kerr images (b and d) are taken in presence of an external magnetic field of about -50 Oe, as indicated by the green dot in the magnetometry measurements (a and c), so that the magnetization of the exchange-biased and non-exchange-biased portions of the FeCo layer point toward opposite directions. Cycling the external field between positive and negative values reveals that the areas with dark contrast are free to switch, as indicated by the yellow double arrows, whereas the zones with light contrast are exchange biased to the IrMn, as indicated by the blue thick arrows. Comparison between the two Kerr images confirms that, as time passes, the areas of the exchange-biased FeCo (light contrast) grow and merge with each other, leaving only few small portions where the FeCo is still free (dark contrast). This is another indication that the spontaneous formation of the exchange bias is indeed driven by the crystallization in the IrMn, which is a two-dimensional growth process.

The fact that the formation of the exchange bias reflects the two-dimensional phase transition in the IrMn, as shown in figure 4.9, allows the interesting possibility of microscopically control the direction of the exchange bias by changing the F magnetization during the crystallization process. In fact, as the crystalline phase spreads across the IrMn layer, the free part of the FeCo layer gets exchange biased according to the direction of its remanent magnetization. Figure 4.10 shows a false-colored Kerr photograph of a sample in which the direction of the remanent magnetization of the FeCo layer was switched 180º twice during the phase transformation of the IrMn. The result is a “patterning” of the direction of the exchange bias that reflects the dimensionality of the crystallization process. In figure 4.10, the portion of the sample represented in blue and green has already undergone crystallization, during which the magnetization of the FeCo layer was switched direction twice. Hence, the exchange bias of the blue and green regions points toward opposite directions. The yellow regions, instead, represent the free portion of the sample, which is still unaffected by the crystallization.

The detailed sequence of the experimental procedure which led to such patterning of the EB direction is also described in figure 4.10, with magnetometry measurements and representative illustrations of false-colored Kerr images. The procedural sequence to generate the pattern shown in the Kerr image of figure 4.10 can be described by considering four different stages.

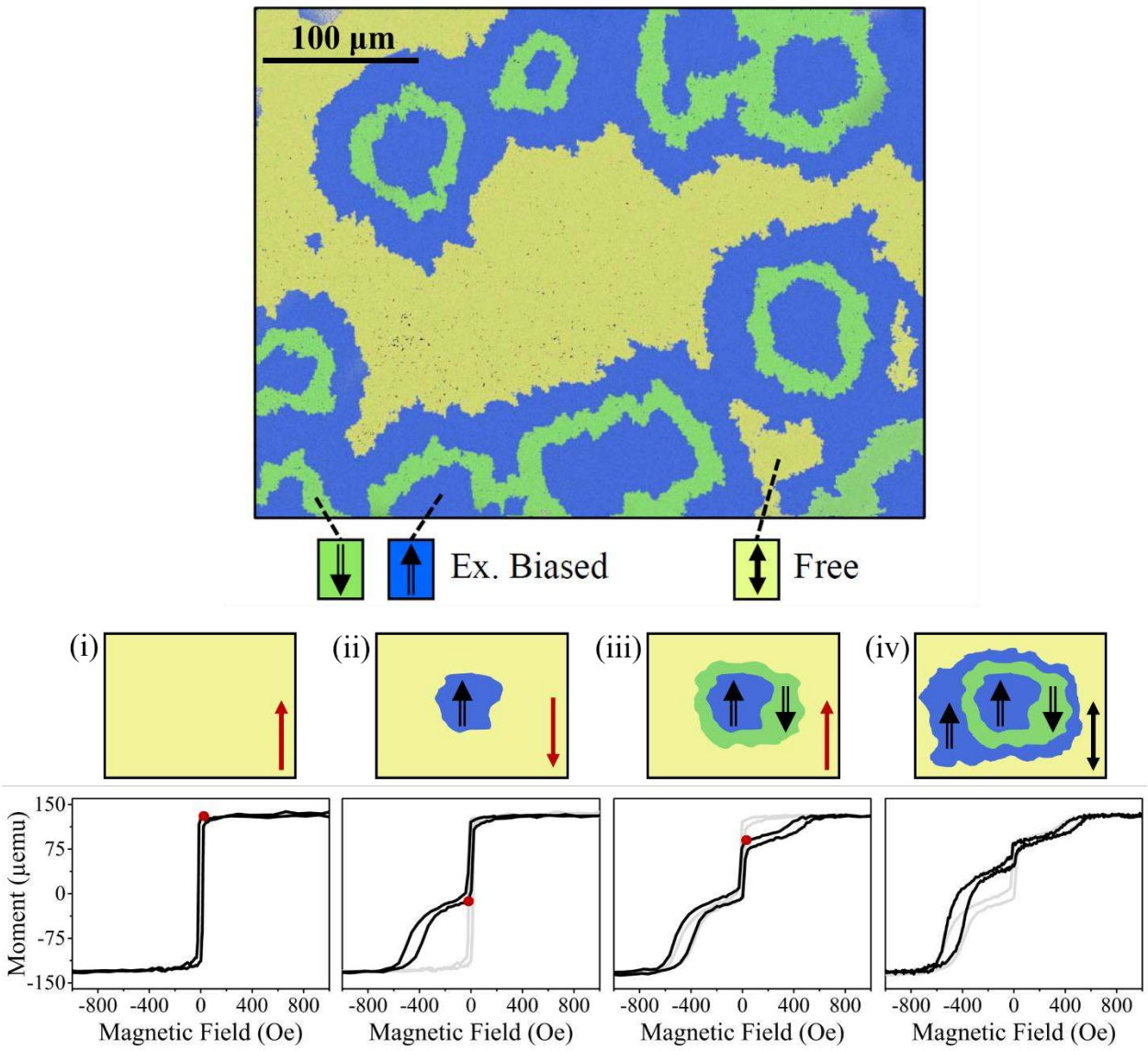

Figure 4.10: Microscopic patterning of the exchange bias direction as a result of switching the remanent magnetization in the FeCo layer as the crystalline phase of the IrMn layer propagates.

i. In the initial state, the as-deposited IrMn is amorphous/nanocrystalline and the magnetometry measurement shows no exchange bias. After the measurement, the FeCo layer is left in its positive remanent magnetization, as indicated by the red dot on the hysteresis loop and the red arrow in the illustration.

ii. When the crystallization triggers and the crystalline phase begins to spread, the FeCo on top of it gets exchange biased according to the direction of its magnetization, as shown by the blue area in the illustration. Since the FeCo remanent magnetization is positive, the exchange-biased part of the loop is shifted toward negative field. After the measurement, the free portion of the FeCo layer is left at negative remanence, as indicated by the red dot in the magnetometry measurement and the red arrow in the

illustration, so that the magnetization of the exchange-biased and free portions of the FeCo point toward opposite directions.

iii. As the crystalline phase continues to spread, newly crystallized portions of the sample, represented by the green area in the illustration, are exchange biased in the direction opposite to the portions set in (ii). Hence, the exchange-biased part of the loop formed in this stage is shifted toward positive fields, as shown in the magnetometry measurement. As phase transformation in the IrMn proceeds by two-dimensional growth, the newly formed exchange-biased portion consists in the annular region around the previously exchange-biased area, represented respectively with green and blue colors in the illustration. After the measurement, the free portion of the FeCo layer is left at positive remanence, as indicated by the red dot on the hysteresis loop and the red arrow in the illustration.

iv. Finally, the newly crystallized area is exchange biased in the direction opposite to the areas set in (iii), but parallel to the ones formed in (ii). Consistently, this portion of the sample is represented as the external blue annular region in the illustration. The exchange-biased part of the loop formed in this stage is shifted toward negative fields and its contribution can be observed in the increase of the amount of the exchange-biased loop formed in (ii), as shown in the magnetometry measurement. At this point, the sample was taken to the Kerr microscope and the image of figure 4.10 was taken.

The intermediate measurements performed during the experimental procedure just described showed no variations of the growth rate or the shape of the exchange-biased domains as a function of the direction of the remanent magnetization, which suggest that the crystalline phase of the IrMn grows unaffected by the direction of magnetization of the FeCo layer. This experiment demonstrates that it is possible to pattern the direction of the exchange bias by changing the magnetization of the F layer during the phase transition in the IrMn. Such microscopic control of the EB direction is generally not possible unless the sample is locally treated with laser or ion radiation [Mougin, 2001; Ueltzhöffer, 2015].

In order to study the magnetization dynamics of the patterned exchange bias shown in figure 4.10, a series of Kerr images was taken while cycling the external magnetic field. Figure 4.11 presents a selection of these images, which summarizes the magnetic response of the FeCo layer during half a cycle of the external field. The magnetometry measurement taken by VSM is repeated in figure 4.12, where the labelled red dots indicate the position on the loop at which

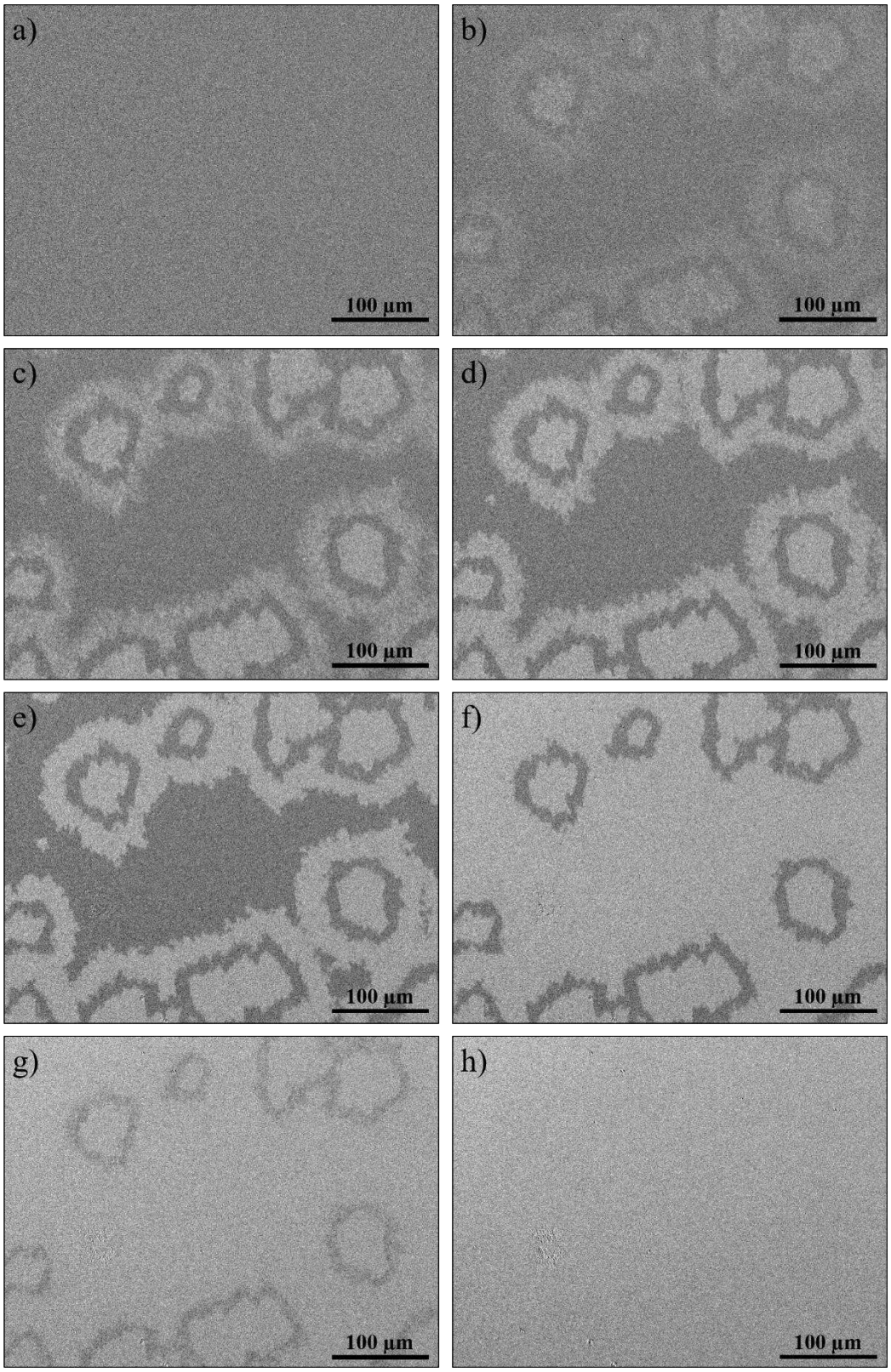

Figure 4.11: Series of Kerr images taken while cycling the external field from negative to positive saturation.

the Kerr images are taken. The comparison between Kerr images and magnetometry confirms the correctness of the interpretation of the magnetic patterning shown in figure 4.10. In fact,

the left-shifted exchange-biased part of the hysteresis loop corresponds to the areas with white contrast in figure 4.11e, whereas the smaller right-shifted part of the loop corresponds to the dark contrast in figure 4.11f. The remaining portion of the FeCo is not exchange biased and switches freely at low values of the external magnetic field.

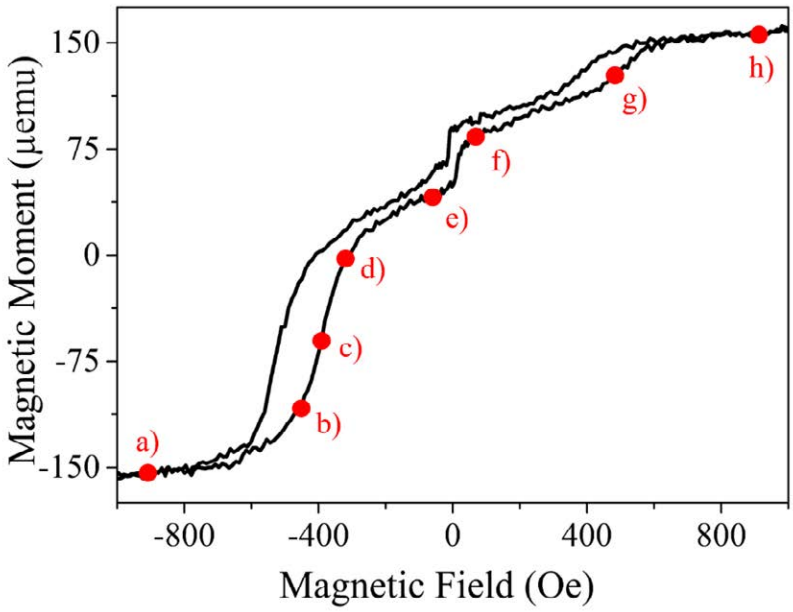

Figure 4.12: Magnetometry measurement of a sample whose remanent magnetization has been inverted twice during the EB formation. The labelled red dots indicate the position on the loop at which the respective Kerr images of figure 4.11 were taken.

These Kerr images allow to observe the magnetization dynamics of the sample. As expected, the non-exchange-biased part of the FeCo switches from negative to positive by rapid propagation of ferromagnetic domain walls (F-DWs), which leads to a quick reversal of the whole area (figures 4.11e-f). On the other hand, the reversal of the exchange-biased portions of the FeCo is gradual, as shown by the different gray tones that these areas assume as the external field cycles (e.g. figures 4.11b-e). The gradual reversal of the exchange-biased areas is likely to be due to a combination of angular dispersion of the EB direction and exchange bias field dispersion. Another interesting feature is that the most recently formed exchange-biased portions have weaker contrast in the images and therefore a lower value of exchange bias field. This can be observed in figure 4.11b-c, where the white annular external areas have a darker contrast compared to the white inner areas, i.e. the formers switch at lower external field. This is consistent with the progressive increase of the exchange bias field during and after the crystallization of the IrMn detected in figure 4.8.

4.3 Exchange Bias Relaxation

In the previous section, it was shown that once the spontaneous crystallization of the IrMn is completed, the FeCo layer is completely exchange biased, with a loop shift and a coercivity of about 700 Oe and 70 Oe respectively. This process to exchange bias a ferromagnetic material differs largely from the usual EB setting procedures, which is achieved by either field-cooling or thermal activation of the AF layer (see section 4.1.2). In order to study the magnetic properties and the thermal stability of these peculiarly set exchange-biased bilayers, a series of magnetic measurements was performed, and the results are organized in two subsections. The first subsection includes magnetic measurements performed at room temperature, in which the magnetic behavior of crystallized samples was tested before performing the standard setting of the exchange bias. The second subsection, instead, covers the temperature dependent experiments, designed according to the York Protocol (see section 4.1.3), which includes the standard setting of the exchange bias.

4.3.1 Room Temperature Experiments

The magnetic properties and the thermal stability of the exchange bias induced by the crystallization of the IrMn was studied by performing magnetometry measurements at room temperature. IrMn/FeCo bilayers were monitored for several days after the completion of the spontaneous formation of the exchange bias, so to guarantee that their structural and magnetic properties were stable. In the first experiment, possible aftereffects induced by repeatedly cycling the external field were investigated.

The experiment consisted in performing consecutive magnetometry measurements by cycling the external magnetic field between -14 kOe and 14 kOe, which is the highest field that can be applied in the VSM of the ISOM-UPM. A selection of the resulting hysteresis loops is presented in figure 4.13a. The measurements show that the loop progressively shifts toward more positive values upon cycling the external field. The values of coercivity, H_c, and exchange bias field, H_{eb}, are plotted as a function of the number of cycles in figure 4.13b. While the coercivity results to be stable with the cycling of the external field, the exchange bias field decreases of about 7% after 32 cycles. The decrease of H_{eb} with the number of consecutive measurements, known as training effect (see section 4.1.1), is mostly associated with partial spin reorientation in the AF layer [Nogués, 1999] and thermal activation of the AF grains

during field cycling [O'Grady, 2010]. Although it is often found that the training effect scales with $1/\sqrt{N}$, where N indicates the number of field cycles [Paccard, 1966; Nogués, 1999], in this case the inset of figure 4.13b shows that the decrease of H_{eb} is linear with $\ln(N)$. This indicates that the weakening of the exchange bias with the number of cycles is due to thermal activation of the IrMn layer during the room temperature measurements.

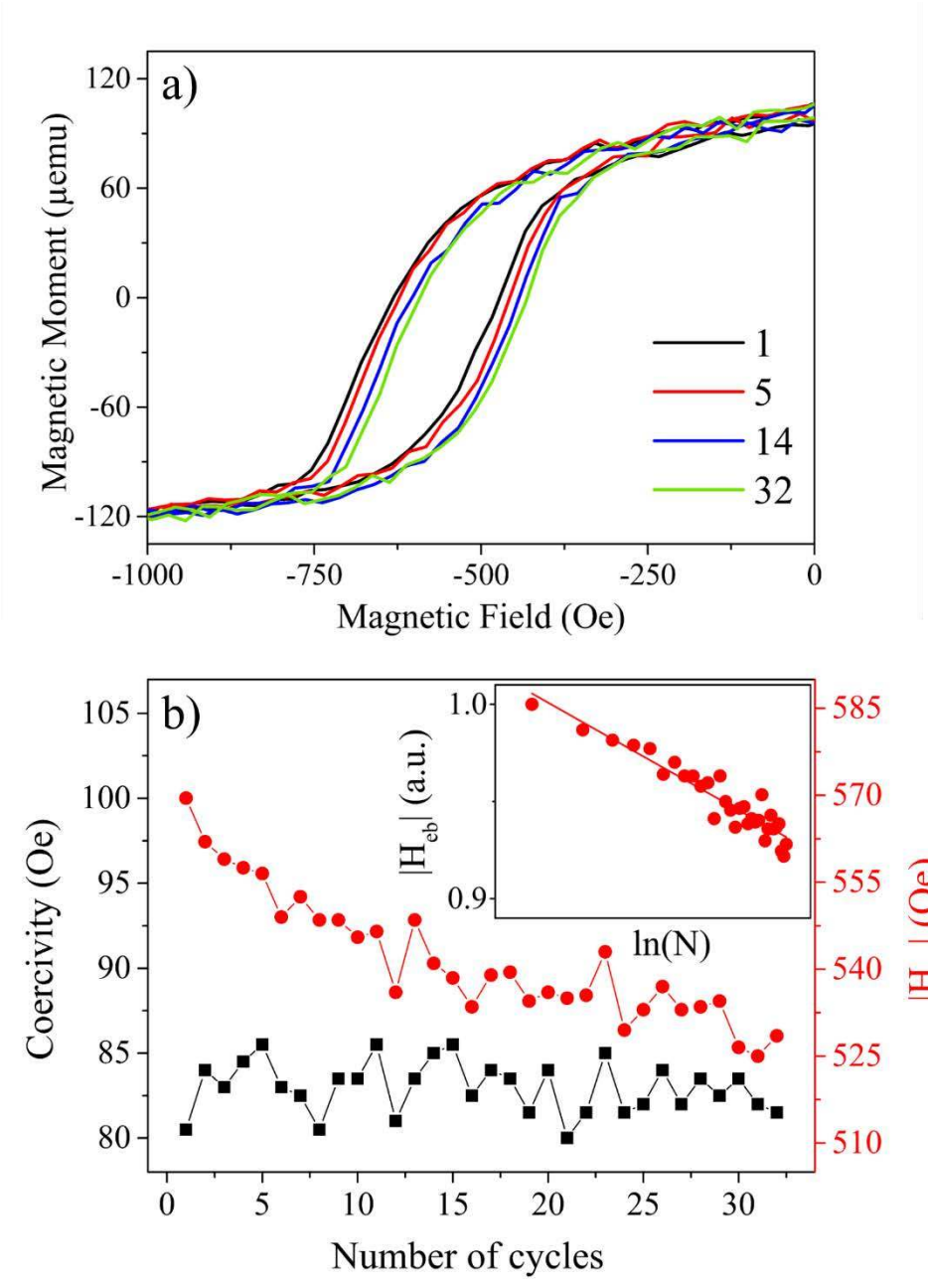

Figure 4.13: a) Series of consecutive magnetometry measurements with high saturation field (14 kOe); b) H_{eb} and coercivity of the hysteresis loop as a function of the number of cycles.

The second experiment focused on testing the thermal stability of the exchange bias at room temperature. The experiment is analogous to the reversal of the exchange bias first performed

by van der Heijden et al. [van der Heijden, 1998] (see section 4.1.2), which consisted in evaluating the relaxation of H_{eb} caused by thermal activation of the IrMn grains, when the sample is kept in a negative saturation field. The experimental procedure is summarized in the diagram on the right of figure 4.14. The sample is held under the effect of a negative magnetic field of -1500 Oe, which is large enough to saturate the biased FeCo. This way, the magnetization in the FeCo layer is reversed 180º with respect to the direction favored by the exchange interaction with the antiferromagnetic IrMn (see configuration (iii) in figure 4.1). The negative saturating field is applied for a period of time of 3 hours, after which the external field is ramped to 1500 Oe and back to -1500 Oe. During this field cycle, magnetometry data are collected. At the end of the measurement the external field is back to -1500 Oe, and the experimental sequence is repeated. Note that the procedure described here does not consider the possible thermal activation of the AF during the time of measurement, as, according to the York Protocol terminology, the non-activation temperature, T_{NA}, of the system is unknown. Nonetheless, since each measurement takes about 20 minutes, during the experiment the sample is kept at negative saturation for 89% of the time. In addition, later measurements performed following the York Protocol showed that samples with this same structure have a T_{NA} of 300 K.

A selection of the measured hysteresis loops is presented in figure 4.14a and shows that the loop progressively shifts toward more positive values. Both the shape of the hysteresis loop and its coercivity are virtually constant during the experiment. The value of the exchange bias field, H_{eb}, is plotted as a function of time in figure 4.14b, which shows the slow lowering of H_{eb} from 740 Oe to 370 Oe in almost 35 days. This relaxation of H_{eb} is the result of the thermal activation of the AF layer, whose grains reorient their magnetic configuration to minimize the exchange energy at the interface with the F layer [Fulcomer, 1972b]. The measurements confirm that the self-developed exchange bias of these samples is quite stable compared, for instance, with the study of Paetzold et al., in which they reported a change of sign of the exchange bias field after 150 hours of a reversal experiment at room temperature [Paetzold, 2002].

The inset shows that the relaxation of H_{eb} plotted against a $\ln(t)$ scale deviates from linear behavior. The non-logarithmic relaxation of H_{eb} can be explained by recalling two theoretical studies about the influence of the energy barrier distribution on time dependence of magnetization in fine particle systems. O'Grady et al. first showed that the reverse time dependence of magnetization follows a logarithmic law when the distribution function of

energy barriers is constant [O'Grady, 1981]. Subsequently, El-Hilo et al. derived the reverse time dependence of magnetization considering a lognormal distribution of particle volumes, as a function of the applied field. They showed that the magnitude of the non-linearity in the ln(t) law depends on the slope of the distribution function of energy barriers over the range of time considered [El-Hilo, 1992]. Hence, according to El-Hilo et al., the non-logarithmic relaxation of H_{eb} of figure 4.14 is probably the result of having a non-constant distribution of activation energy in the AF layer, whose slope is positive in the range of time of the experiment. Nevertheless, an alternative interpretation of the non-logarithmic response is provided in section 5.3.2, when discussing the mechanism which establishes the exchange bias.

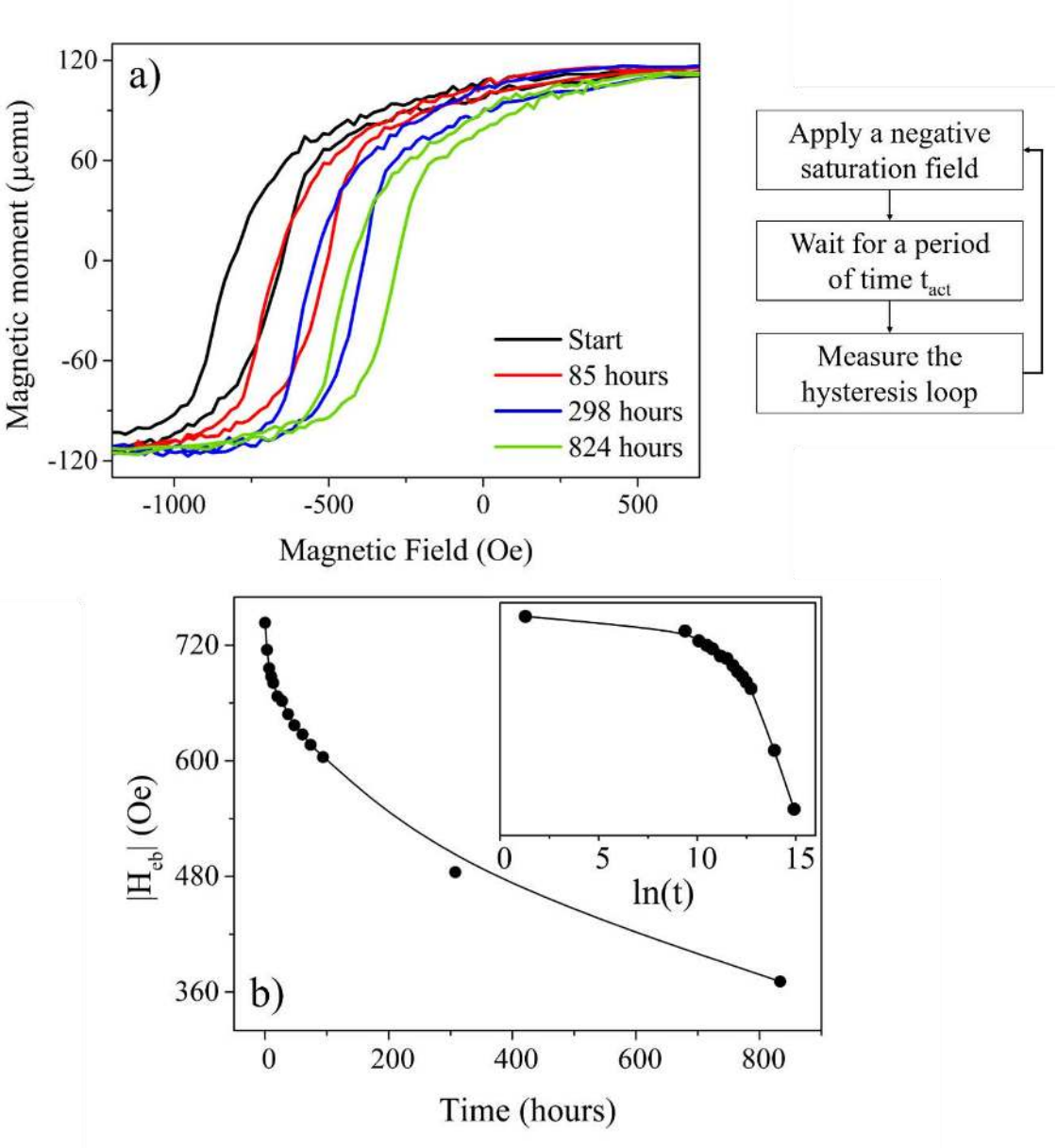

Figure 4.14: a) Selection of magnetometry measurements taken during the room temperature EB relaxation experiment; b) decay of H_{eb} as a function of time; inset: representation of (b) in logarithmic scale.

4.3.2 Temperature Dependent Experiments

As introduced in section 4.1.3, according to the York Protocol the magnetic characterization of exchange-biased bilayers requires the initial setting of the exchange bias and the evaluation of its thermal properties, i.e. the non-activation temperature, T_{NA}, and the median blocking temperature, $<T_B>$. This section describes a series of temperature dependent experiments, based on the experimental procedure defined by the York Protocol, which led to a thorough characterization of structurally stable IrMn/FeCo bilayers. These experiments were all performed with the MicroSense Model 10 Vector magnetometer of the University of York, which allows to control the temperature in a range of 77-700 K and to apply a magnetic field as high as 20 kOe. The values chosen for the main experimental parameters, such as the setting temperature, T_{set}, the setting time, t_{set} and the activation time, t_{act}, are justified in ref. [O'Grady, 2010] where the York Protocol was first described. In order to avoid detrimental oxidation of the FeCo layer during the high temperature annealing, a 5-nm-thick Ta layer was chosen as capping layer in the samples used for temperature dependent experiments.

Before performing any measurement, a preliminary procedure is required to ensure that no thermal activation happens during the measurement time, which is done by evaluating the non-activation temperature, T_{NA}, of the sample. The procedure consists in guessing a plausible T_{NA} and verifying the effect of the thermal activation of the exchange bias at that specific temperature. If the thermal activation is negligible, this guessing temperature is taken as T_{NA}, otherwise a lower temperature must be tried. The detailed experimental procedure used to evaluate T_{NA} is described in ref. [O'Grady, 2010]. In case of structurally stable IrMn/FeCo bilayers, the first guessing temperature used was 300 K and the thermal activation of the AF layer resulted to be negligible. Hence, the temperature 300 K was taken as T_{NA}.

As shown in section 4.2, the development of the exchange bias studied in this work is directly induced by the crystallization of the IrMn. This non-controlled structural process which sets the exchange bias differs largely from the standard EB setting procedure and is likely to induce a variety of defects, dispersions and stresses in the bilayer. Therefore, it is expected that the setting of the exchange bias following the York Protocol would improve the performance of the bilayer, increasing the exchange bias field. Accordingly, the first experiment consisted in monitoring the magnetic response of the sample after performing the setting of the exchange bias at progressively higher temperatures. The experimental procedure is summarized in the diagram on the right of figure 4.15. The sample is held under the effect of a positive magnetic

field of 10 kOe, oriented in the direction favored by the exchange interaction between the F and AF layers (see configuration (i) in figure 4.1). While maintaining the positive magnetic field, the sample is heated up to the setting temperature, T_{set}, whose value will be increased at every iteration of the experiment. Hence, the sample, still in presence of the positive magnetic field, is kept at T_{set} for 90 minutes, during which time the setting of the exchange bias is achieved. After that, the sample is cooled down to T_{NA}, i.e. 300 K, at which temperature two consecutive magnetometry measurements are performed, by cycling the external field to -10 kOe and back to 10 kOe twice. Taking two consecutive measurements at every iteration allows to evaluate the athermal part of the training effect. Further magnetometry measurements are not required, as thermal activation, which is responsible for the thermal component of the training effect, is negligible at T_{NA} [O'Grady, 2010]. At the end of the measurement the external field is back to 10 kOe, and the experimental sequence is repeated.

The setting temperature, T_{set}, was increased 30 K at every iteration, up to a maximum value of 500 K, so to avoid interdiffusion of Mn which is known to happen at temperatures higher than 570 K [Samant, 2000; Cardoso, 2000; Yoo, 2002]. The data showed that the effect of the athermal training is negligible, as the hysteresis loop is virtually unaltered after the first measurement and the descending branch of the loop shifts by only 5 Oe. Hence, for this experiment, only the second magnetometry measurements taken in each iteration is shown here. A selection of the resulting hysteresis loops is presented in figure 4.15a. The data show that upon setting at higher temperatures, the hysteresis loop drastically changes its shape, coercivity and exchange bias field. Although it cannot be appreciated in the figure because of the range chosen for the magnetic field, the saturation magnetization of the sample is unvaried upon heating at increasing temperatures, which means that the 5-nm-thick Ta capping layer efficiently prevented detrimental oxidations of the FeCo layer. The values of coercivity, H_c, and exchange bias field, H_{eb}, are plotted as a function of the setting temperature, T_{set}, in figure 4.15b. The response of the hysteresis loop to the setting of the exchange bias is significantly different at low and high temperatures. In the range from 300 to 410 K, the coercivity quickly drops from 77 to 43 Oe, while the exchange bias field increases of about 30 Oe. This is also the range of temperatures in which the shape of the loop changes the most, as shown by the black and red curves of figure 4.15a. In the range from 410 to 500 K, the coercivity diminishes only a few oersteds while the exchange bias field drastically decreases from 670 to 510 Oe, as shown by the red and blue curves of figure 4.15a.

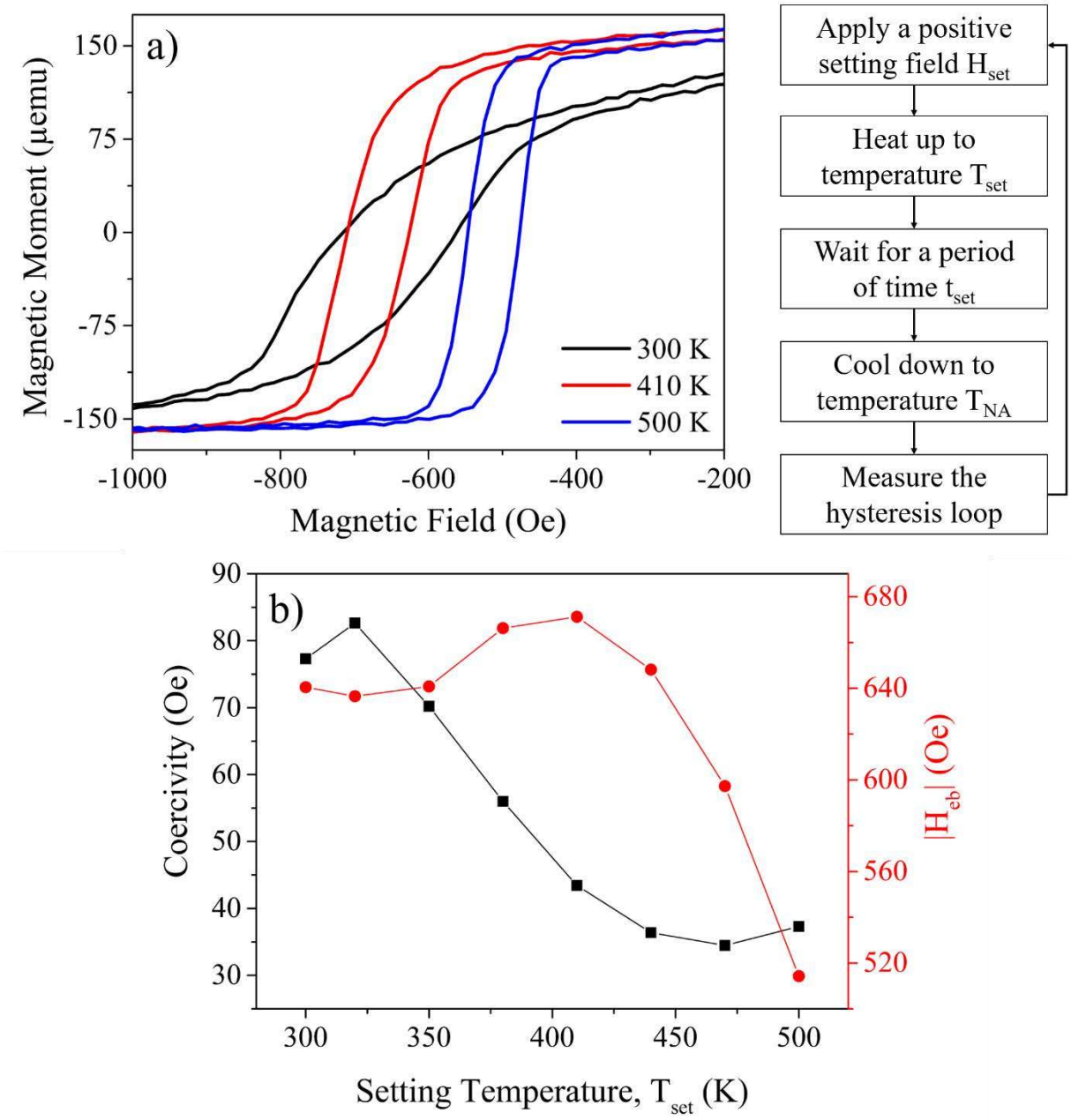

Figure 4.15: a) Magnetometry measurements taken after the EB setting at different temperatures, T_{set}; b) H_{eb} and coercivity of the hysteresis loop as a function of the setting temperature, T_{set}. The solid lines are a guide to the eye.

The behavior of H_c and H_{eb} shown in figure 4.15b can be best understood by analyzing the variation of the two branches of the hysteresis loop separately. The definition of H_1 and H_2, i.e. respectively the values of the external field at which the magnetic moment goes to zero during the descending and ascending branches of the loop, is made explicit in figure 4.16a. The variation of H_1 and H_2 as a function of the setting temperature, T_{set}, is plotted in figure 4.16b. In the range from 300 to 410 K, the data show that it is mostly the ascending part of the loop, represented by H_2, what varies, with an increase of 66 Oe. According to the definition of H_{eb}

and H_c (see section 4.1), an increase of the sole H_2 implies an increase of H_{eb} and a decrease of H_c of half the amount of the variation of H_2, i.e. 33 Oe in this case. As in this range of temperature both the increase of H_{eb} and the decrease of H_c are about 30 Oe (figure 4.15b), these variations seem to be exclusively due to the shift toward higher negative field of the ascending branch of the loop. In the range from 410 to 500 K, instead, both H_1 and H_2 progressively decrease of almost the same amount, as a result of the progressive reduction of H_{eb} for temperatures above 410 K (figure 4.15b). This reduction of H_{eb} is counterintuitive because, in absence of structural changes and sample damaging, such as oxidation or interdiffusion, field annealing should optimize the exchange bias in samples with polycrystalline IrMn. After the EB setting shown in figure 4.15, the sample was checked by XRD and no structural changes were observed. A possible explanation for this peculiar result, based on the idea that the large IrMn grains are broken in smaller antiferromagnetic domains, is proposed in section (5.3.2).

As explained in section 4.1.1, it is the exchange interaction between the F and the AF spins at the interface what drives the magnetic reorientation of the AF grains during the EB setting, and not the external field. However, the study performed by Fernandez-Outon et al. on IrMn/FeCo bilayers showed a high dependence of the exchange bias field with the value of H_{set} [Fernandez-Outon, 2008]. Therefore, the second temperature dependent experiment consisted in evaluating the effect of setting the exchange bias at fields higher than 10 kOe. Firstly, the sample was annealed at a T_{set} of 500 K in presence of a H_{set} of 10 kOe for several hours, in order to completely set the exchange bias and to be sure that no further activation of the AF layer could happen during the experiment. This preliminary annealing was necessary as, even though a setting time of 90 minutes, which is the standard value for the York Protocol, is sufficient to successfully set most of the AF grains [O'Grady, 2010], any small activation during consecutive EB settings at higher fields could lead to possible misinterpretations of the results. The experimental procedure consisted in the iteration of the setting process described in figure 4.15, but at a fixed T_{set} of 500 K, for three setting fields, H_{set}, i.e. 10 kOe, 15 kOe and 20 kOe. Again, two loops were measured at every iteration, and the athermal training resulted to be negligible and independent of the external field. The resulting hysteresis loops are presented in figure 4.17. The data show a clear shift of the descending branch of the loop toward higher negative fields, of about 2.2% at 20 kOe, as well as a slight shift of the ascending branch of the loop, about 0.4%, toward the same direction. The shift of the descending loop causes a consequent increase of the exchange bias field of about 1.4% and an important increase of the

coercivity, of about 18%. This behavior does not agree with the results obtained by Fernandez-Outon et al. on IrMn/FeCo bilayers, which showed that the increase of the H_{eb} at higher H_{set} manifests equally in both branches of the loop, giving a constant value for the coercivity [Fernandez-Outon, 2008].

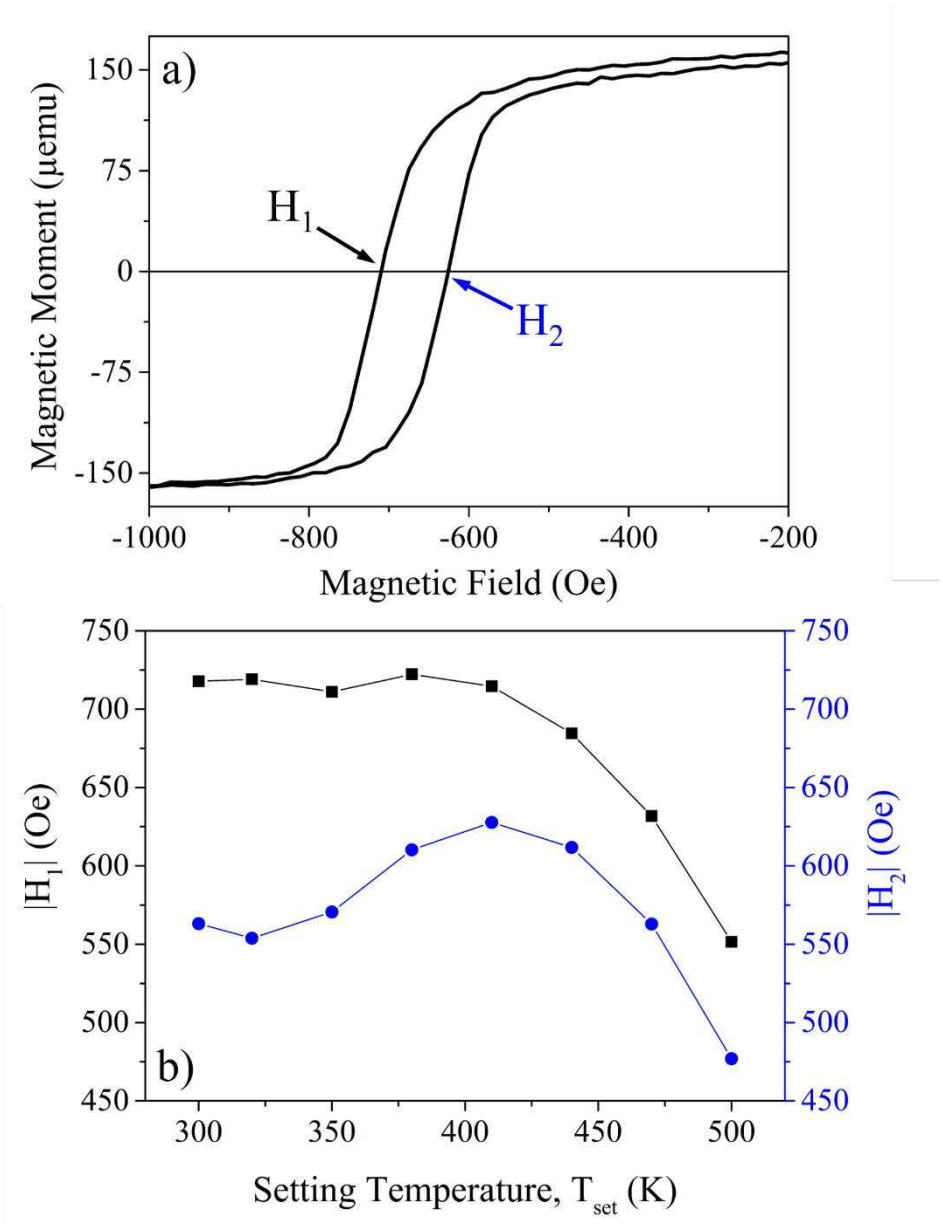

Figure 4.16: a) Example of exchange-biased hysteresis loop where the position of H_1 and H_2 is indicated; b) H_1 and H_2 as a function of the setting temperature, T_{set}. The solid lines are a guide to the eye.

Finally, the thermal stability of a properly set sample was tested by evaluating the median blocking temperature, $<T_B>$. As introduced in section 4.1.3, the median blocking temperature is defined as the activation temperature, T_{act}, at which the controlled activation of the AF layer

makes the exchange bias field goes to zero, as a consequence of having equal fractions of the volume of the AF layer oriented in opposite directions.

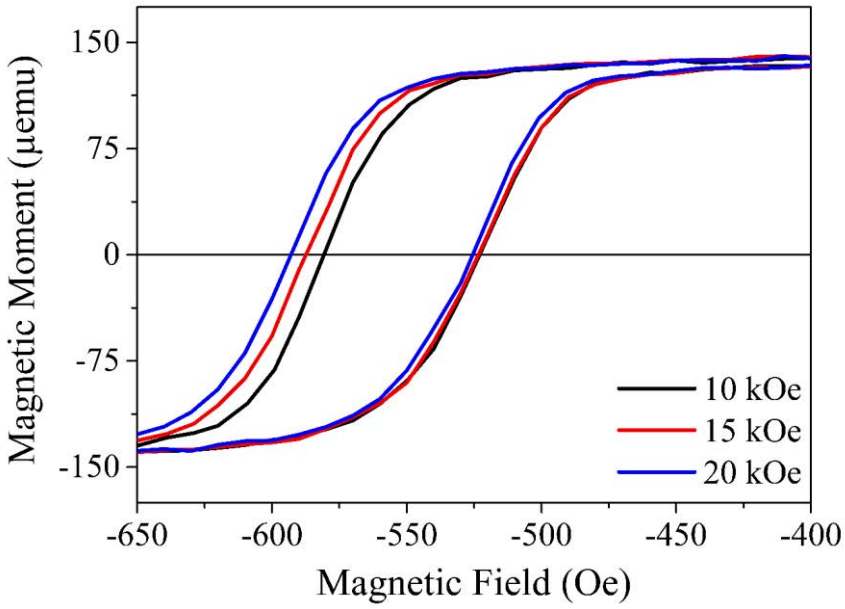

Figure 4.17: Magnetometry measurements taken after the EB setting at different external magnetic fields.

The experimental procedure is summarized in the diagram on the right of figure 4.18. The sample is held under the effect of a negative magnetic field of -10 kOe. This way, the magnetization in the FeCo layer is reversed 180º with respect to the direction favored by the exchange interaction with the antiferromagnetic IrMn (see configuration (iii) in figure 4.1). While maintaining the negative magnetic field, the sample is heated up to the activation temperature, T_{act}, whose value will be increased at every iteration of the experiment. Hence, the sample, still in presence of the negative magnetic field, is kept at T_{act} for 30 minutes, during which time part of the IrMn is thermally activated and reorients its magnetic configuration to minimize the exchange energy at the interface with the FeCo layer. After that, the sample is cooled down to T_{NA}, i.e. 300 K, at which temperature the external field is rapidly reversed from -10 kOe to 10 kOe, so to remove the athermal training effect which takes place in the first reversal of the F layer [O'Grady, 2010]. Then, the magnetometry measurement is performed, by cycling the external field to -10 kOe and back to 10 kOe. At the end of the measurement the external field is rapidly swapped back to -10 kOe, and the experimental sequence is repeated.

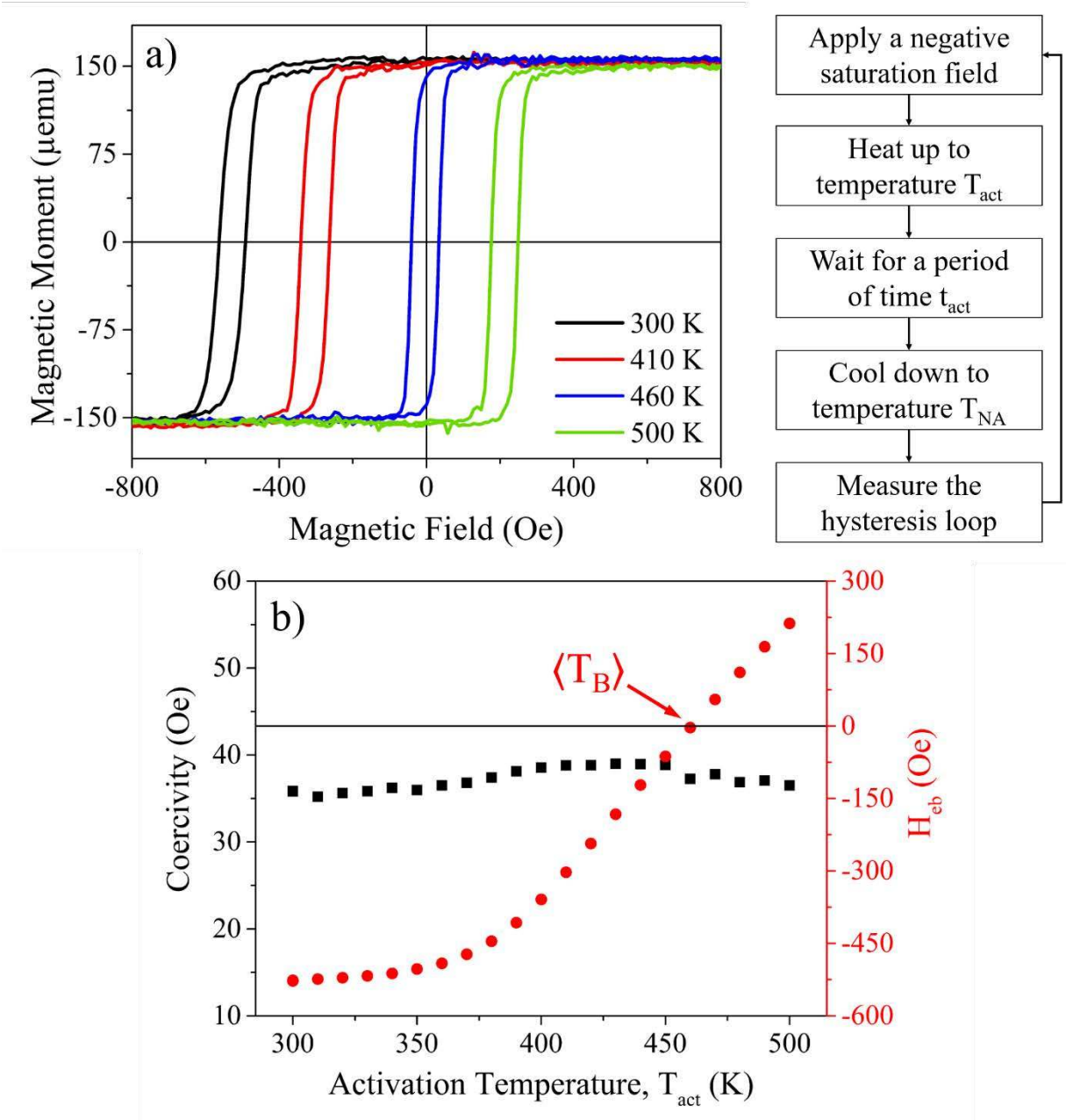

Figure 4.18: a) Selection of magnetometry measurements taken after the temperature dependent EB relaxation experiment at different activation temperatures, T_{act}; b) H_{eb} and coercivity of the hysteresis loop as a function of the activation temperature, T_{act}.

The activation temperature, T_{act}, was raised of 10 K at every iteration, up to a maximum value of 500 K. A selection of the measured hysteresis loops is presented in figure 4.18a. The data show that the hysteresis loop shifts toward positive fields upon increasing the activation temperature, maintaining virtually constant its shape and coercivity. The values of coercivity, H_c, and exchange bias field, H_{eb}, are plotted as a function of the activation temperature, T_{act}, in figure 4.18b. The exchange bias field is mostly stable up to 360 K, above which temperature its variation rapidly accelerates up to a rate of 6 Oe/K, and it reaches zero at an activation

temperature of 460 K. Therefore, the median blocking temperature, $<T_B>$, for this sample is 460 K. On the other hand, the coercivity is only slightly affected by the experiment, as its values increases from 35 Oe up to a maximum of 39 Oe at 430 K, i.e. 11%, before decreasing again. A peak in the coercivity (although much more relevant) at temperatures in the vicinity of the median blocking temperature was previously detected in IrMn/FeCo bilayers by Fernandez-Outon et al. [Fernandez-Outon, 2006].

In section 4.1.3, it was shown how to determine the value of the anisotropy of the antiferromagnetic layer, K_{AF}, directly from the measurements performed following the York Protocol [Vallejo-Fernandez, 2007]. The AF anisotropy can be derived with equation 4.5, when the median blocking temperature, $<T_B>$, and the median grain volume, V_m, are known. Usually, the grain volume distribution in polycrystalline samples can be estimated with precision by TEM characterization [Vopsaroiu, 2005]. This is possible as polycrystalline materials deposited by magnetron sputtering tend to form columnar grains, whose lateral size can be easily measured in TEM imaging, as shown in ref. [Vopsaroiu, 2005]. However, the structural analysis presented in chapter 3 showed that when the IrMn crystallizes, it tends to form highly-crystalline long dendritic grains, which eventually merge together being indistinguishable (see figure 3.14b). This phenomenon prevented to estimate precisely the grain volume distribution in these samples. Nonetheless, the structural characterization indicated that the crystallized IrMn consists of very large grains: in XRD in-plane $\varphi/2\theta_\chi$ scans, the Scherrer equation gave an estimation for the minimum lateral grain size of 37 nm (see section 3.2.3); in-plane TEM imaging showed the formation of dendritic grains hundreds of nanometers long (see figure 3.13); cross-section TEM images showed the presence of grains with a lateral grain size of the order of 100 nm (see figure 3.21).

Assuming a value for the anisotropy of the IrMn of K_{AF} (295 K) = 5.5 erg/cm^3, which was found to be constant with thickness for IrMn layers thicker than 5 nm [O'Grady, 2010], equation 4.6 would give K_{AF} ($<T_B>$) = 3.2 erg/cm^3, for the bulk value of T_N, which is 690 K [Nogués, 1999]. Hence, an estimation for the median grain volume can be found by rearranging equation 4.5 as

$$V_m = \frac{\ln(t_{act} \cdot f_0)}{K_{AF}(\langle T_B \rangle)} k_B \langle T_B \rangle. \qquad (4.8)$$

For $<T_B>$ = 460 K, t_{act} = 30 min and $f_0 = 2.1 \cdot 10^{12}$ Hz [Vallejo-Fernandez, 2010], equation 4.8 gives V_m = 711 nm^3, which, for a 15-nm-thick layer, corresponds to a median lateral grain size

of D_m = 7.8 nm. This value is considerably smaller than the grain size suggested by the structural characterization, and it indicates that the average size of the magnetic volumes that determine the properties of the exchange bias is smaller than the volume of the crystalline grains in the IrMn layer. This would imply that the large IrMn grains are broken in AF domains, which affect the strength and the thermal stability of the induced exchange bias. This hypothesis, for which the simple granular model used here is inadequate, is discussed in the next chapter.

4.4 Conclusions

In this chapter, we have presented a series of experiments which concurred to achieve the detailed magnetic characterization of multilayers deposited by magnetron sputtering, with generic structure SL/IrMn(15nm)/FeCo(5nm)/CL. As shown in chapter 3, in these samples the IrMn layer is deposited in an amorphous metastable state and it subsequently undergoes a progressive crystallization at room temperature. Here, the results of the extensive magnetic characterization of these samples are summarized.

The magnetic behavior of the bilayers during the spontaneous phase transition in the IrMn was checked by VSM magnetometry measurements and Kerr images (section 4.2.1). Magnetometry measurements of as-deposited samples showed centered hysteresis loops with coercivity virtually equivalent to the one of a 5-nm-thick FeCo layer (figures 4.7 and 4.8). Combined magnetometry measurements and out-of-plane $\theta/2\theta$ scans confirmed that in this stage the IrMn is amorphous and it does not induce exchange bias in the FeCo layer (figure 4.7). Just by leaving the samples at room temperature in the remanent state of the F layer, the exchange bias develops spontaneously over a period of time which varies from few hours to several days. The progressive development of the EB was carefully characterized by consecutive magnetometry measurements (figure 4.8), and it seems to be the result of two distinct processes. Initially, an increasing amount of the hysteresis loop develops exchange bias, while the remaining centered part of the loop decreases proportionally. This is caused by nucleation and expansion of exchange-biased areas, according to a two-dimensional growth, which eventually cover the whole sample. Concurrently, the exchange-biased part of the hysteresis loop shifts laterally with time, increasing the exchange bias field even after the conclusion of the phase transition. Once the spontaneous formation of the exchange bias is complete, further XRD measurements indicate that the IrMn crystallized with a high (111) texture (figure 4.7).

Kerr microscopy images showed the presence of well-defined dendritic domains in which the FeCo is exchange biased, with the remaining part of the FeCo being free to reverse with low external fields (figure 4.9). The images confirmed that these domains expand with time following a two-dimensional growth process and eventually merge, covering the whole sample. Hence, this spontaneous formation of the exchange bias is indeed driven by the crystallization in the IrMn, which is a two-dimensional growth process, as shown in chapter 3. This fact allows the interesting possibility of a microscopic control of the direction of the exchange bias by changing the FeCo magnetization during the crystallization process. This was confirmed by Kerr images of a sample in which the direction of the remanent magnetization of the FeCo layer was reversed twice during the phase transformation of the IrMn. The result is a "patterning" in the form of annular domains with alternating direction of the exchange bias (figures 4.10, 4.11 and 4.12).

The magnetic properties of these samples in which the exchange bias developed spontaneously were characterized by magnetometry measurements at room temperature. Spontaneously crystallized samples not subjected to post-annealing treatment have an exchange bias field, H_{eb}, that reaches values between 600 Oe and 750 Oe, which implies an interfacial exchange coupling of about $J_K = 0.5 - 0.6\ erg/cm^2$, and a coercivity of about 70 Oe (figures 4.7 and 4.8). These samples show only a bland training effect, upon cycling the external field between -14 kOe and 14 kOe (figure 4.13). Moreover, the exchange bias proved to be quite stable upon performing a prolonged reversal experiment, showing a decrease of the exchange bias field of about 50% after 35 days (figure 4.14).

In order to achieve a thorough magnetic characterization of structurally stable IrMn/FeCo bilayers, a series of temperature dependent experiments were performed, based on the experimental procedure defined by the York Protocol (section 4.1.3). An experiment of standard setting of the exchange bias at increasing temperatures showed the unexpected lowering of the exchange bias field, together with a decrease of the coercivity and an improvement in the loop shape (figure 4.15). The variations of the two branches of the hysteresis loop highlighted two temperature ranges. In the range from 300 to 410 K, the coercivity drops rapidly as the loop gets squarer. In the range from 410 to 500 K, the shape of the loop is unaltered, but the exchange bias field decreases of about 24% (figure 4.16). This reduction of H_{eb} is counterintuitive because the setting procedure of the York Protocol should optimize the exchange bias in samples with polycrystalline IrMn. The second experiment consisted in setting the exchange bias at progressively higher magnetic fields. The data show

that only the descending branch of the loop is affected by the higher field, with an increase of the coercivity of about 18% (figure 4.17). The final experiment consisted in the temperature-controlled activation of the AF layer, according to the procedure defined in the York Protocol. The exchange bias field was plotted as a function of the activation temperature, and a median blocking temperature of 460 K was found. By rearranging the equations presented in section 4.1.3, a value for the median lateral grain size of D_m = 7.8 nm was found. This value is surprisingly small when compared to the crystalline grain size extracted from the structural characterization (chapter 3), and it indicates that the large IrMn grains are likely broken in AF domains, which affect the strength and the thermal stability of the induced exchange bias.

Chapter 5: Effects of the crystallization of the IrMn layer on the exchange bias

The research presented in this thesis has its origin in the delayed spontaneous crystallization of IrMn thin films deposited by magnetron sputtering, which is reported here for the first time. In chapter 3, the structural characterization of the IrMn layer during the various stages of the crystallization revealed a slow phase transition from amorphous to γ-IrMn, which takes place spontaneously at room temperature. Concurrently, the magnetic characterization presented in chapter 4 explained largely the magnetic behavior of the bilayers, but it also highlighted some discrepancies between the experimental data and the theoretical predictions. This peculiar behavior of the IrMn is a unique characteristic of the samples studied in this work, and its influence on the magnetic properties of exchange biased bilayers has never been studied before. This chapter focuses on the role of this phase transition in determining the final properties of the exchange bias. In the first section, the kinetics of the crystallization is studied in light of the experimental data collected during the phase transformation. The second section consists in a brief overview of the microstructure of crystallized IrMn, with particular emphasis on the planar defects, analyzed via TEM imaging. In the third section, we analyze the possible interpretations of the deviations from the theoretical predictions in the magnetic response of the crystallized samples, in light of the simulations performed with a strong antiferromagnetic domain wall (AF-DW) pinning model. Finally, we propose physical mechanism for the spontaneous setting of the exchange bias, which implies the slow development of strongly pinned spin clusters at interfacial defects between the F and the AF layer.

5.1 Kinetics of the crystallization of IrMn

The detailed structural characterization presented in chapter 3 revealed that the as-deposited IrMn layer is initially amorphous, and it subsequently crystallizes into a highly crystalline γ-phase. The TEM images (section 3.3.1) and the Kerr images (section 4.2.2) taken during the phase transition, indicated that the IrMn layer crystallizes according to a nucleation and growth process. In this section the data collected during the phase transition in the IrMn are analyzed in order to shed some light on the kinetics of the crystallization process. First, we introduce few concepts of crystallization in amorphous alloys that are relevant to the present study.

Amorphous metallic alloys, more commonly referred to as glassy or non-crystalline alloys, are metal alloys with no long range atomic order, whose disordered state of matter is achieved by rapid solidification of the alloying constituents from the vapor or liquid phases [Luborsky, 1983]. When an alloy in the liquid (or vapor) phase is slowly cooled below its melting temperature, the material undergoes the formation of one or more crystalline phases which minimize the Gibbs free energy of the system. This crystalline solidification, which can happen by several different processes, generally occurs for cooling rates lower than 10^3 K/s. However, if the alloy is cooled at a much higher rate (10^6 - 10^7 K/s) the constituents are prevented to form an ordered structure, and the rapid solidification results in an amorphous metallic alloy [Porter, 2009]. Such a high cooling rate requires rapid heat removal from the material, which can be achieved by maximizing the contact area between the alloy and the cooling medium. This process is called quenching.

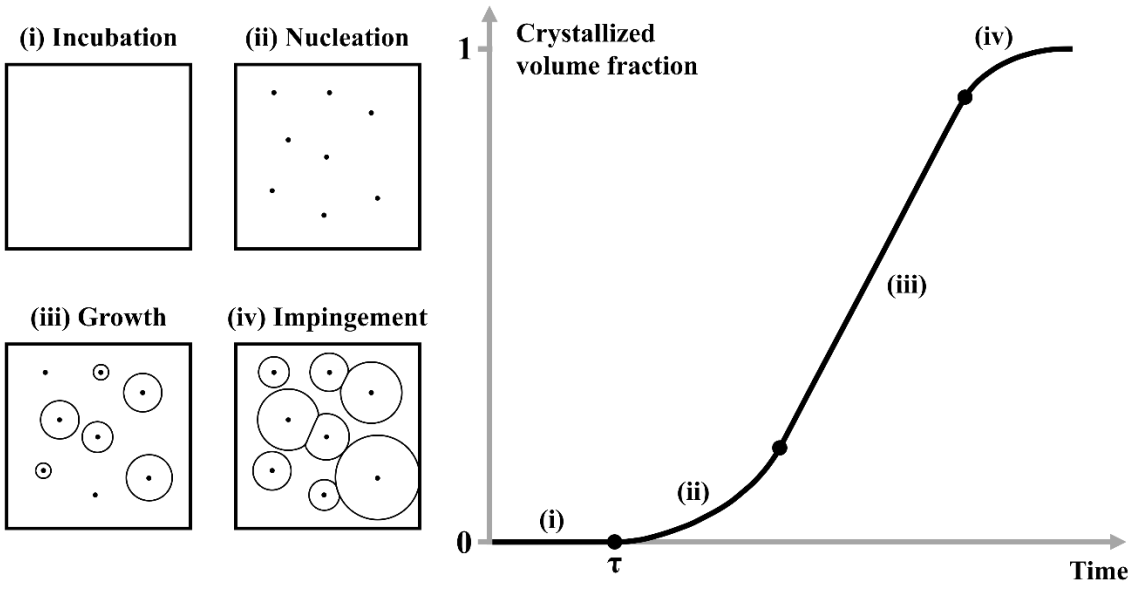

Figure 5.1: Schematic diagram of the crystallized volume fraction as a function of time, as a consequence of a nucleation and growth crystallization. Insets are two-dimensional illustrations representing the four stages of the nucleation and growth process.

Although the most common quenching techniques are based on the solidification from the liquid phase, amorphous metal alloys can also be obtained by physical vapor deposition. In fact, atom-by-atom preparation methods, such as magnetron sputtering, involve a high surface-to-volume ratio of the deposited material onto the substrate, which acts as the cooling medium, leading to cooling rates over 10^8 K/s [Liebermann, 1983]. In addition, the deposition of atoms having low mobility at the substrate surface [Scott, 1983], as well as contamination by

extraneous atom species, such as oxygen [Bennett, 1972; Leung, 1974], promote the formation of metallic glass. The first report of vapor-deposited amorphous metallic alloys was published by J. Kramer [Kramer, 1934]. Since then, the crystallization of amorphous thin films deposited by magnetron sputtering has been studied in several alloys, such as NiTi [Lee, 2004; Liu, 2007], GeSbTe [Jeong, 1999], AgInSbTe [Njoroge, 2001], CoNbZr [Jiang, 2005]. Nevertheless, the deposition of amorphous IrMn by magnetron sputtering and its consequent crystallization has never been reported before.

The Gibbs free energy associated with the amorphous phase of metallic alloys produced by quenching is higher compared to the corresponding crystallized phases. Hence, glassy alloys are metastable and, if provided with enough thermal energy, they can undergo an ordering phase transformation so to minimize the free energy. This structural transformation, which is referred to as "glass crystallization" or "devitrification", can take different forms but it generally happens by a nucleation and growth process [Scott, 1983]. The progression of the crystallization is usually represented by the crystallized volume fraction, $x = V_x/V_{tot}$, as a function of time, where V_x is the volume of the crystallized portion of the alloy and V_{tot} is the total volume. Nucleation and growth processes involve four different stages, which lead to the typical sigmoidal shape of the volume fraction as a function of time, shown in the schematic diagram of figure 5.1:

i. Initial incubation period, τ, necessary to the formation of the first nuclei, during which x is constant at zero as the crystallization is not initiated yet. The incubation time could be zero if nucleation sites form during the solidification of the alloy, as well as extremely long, depending on various factors, such as temperature, alloy composition and mode of nucleation.

ii. The crystallization begins with the nucleation of very small particles of the crystalline phase, called nuclei, within the metastable amorphous phase. Nucleation can be homogenous, if it is not influenced by extrinsic factors, or heterogenous, if it happens at sites such as defects, impurities and boundaries. The nucleation rate greatly influences the crystallization process of a glassy alloy. In the initial nucleation period x increases slowly with time.

iii. As soon as nuclei are formed, nearby atoms are energetically driven to arrange orderly at the interface between the crystalline and the amorphous phases. The nuclei growth can be limited by local interfacial kinetics (interface-controlled), by long-range

diffusion of the atoms (diffusion-controlled) or it can happen according to a mix of the two behaviors, depending on factors such as temperature, composition of the crystalline phase and atoms mobility in the glassy alloy. Nuclei growth accelerate the increase of x with time and it is therefore responsible for the crystallization of most of the alloy.

iv. The crystallization ends with the impingement of the growing crystals, whose phase transition is stopped where adjacent grains meet, but keeps spreading in the remaining available directions. Consequently, grains impingement slows down the approach of x to unity, which is reached when the whole sample is crystallized.

The study of the crystallization kinetics of a glassy alloy can be performed in isothermal, as well as non-isothermal conditions. Considering the type of measurements performed in this research work, only the former case is discussed here. For additional information about the analysis of the crystallization kinetics of glassy alloys, refer to [Mastai, 2012]. The isothermal crystallization can be characterized by measuring the crystallized volume fraction as a function of time, at fixed temperature. The kinetics of the crystallization process is generally analyzed with the Johnson-Mehl-Avrami-Kolmogorov (JMAK) model [Johnson, 1939; Avrami, 1939; Avrami, 1940; Avrami, 1941; Kolmogorov, 1937]. According to the JMAK model, the crystallized volume fraction during crystallization increases with time as

$$x(t) = 1 - \exp[-k(t-\tau)^n], \qquad (5.1)$$

where τ is the incubation period of nucleation, n is the Avrami exponent, which depends on the crystallization mechanism, and k is the kinetic parameter. The Avrami exponent can be expressed as $n = n_n + n_g$ [Scott, 1983]. The nucleation exponent, n_n, describes the time dependence of the nucleation rate and can assume the values $0 \leq n_n \leq 1$, where $n_n = 0$ indicates that nucleation sites are already present in the as-formed glassy alloy and no further nucleation occurs, $n_n = 1$ indicates constant nucleation rate during the crystallization and $0 < n_n < 1$ indicates decreasing nucleation rate. The growth exponent, n_g, describes the dimensionality of the crystal growth and can assume the values $1 \leq n_n \leq 3$, which indicate respectively one-, two- or three-dimensional growth processes. Hence, the Avrami exponent describes simultaneously the mode of nucleation and the dimensionality of the growth process and it can assume the values $1 \leq n \leq 4$.

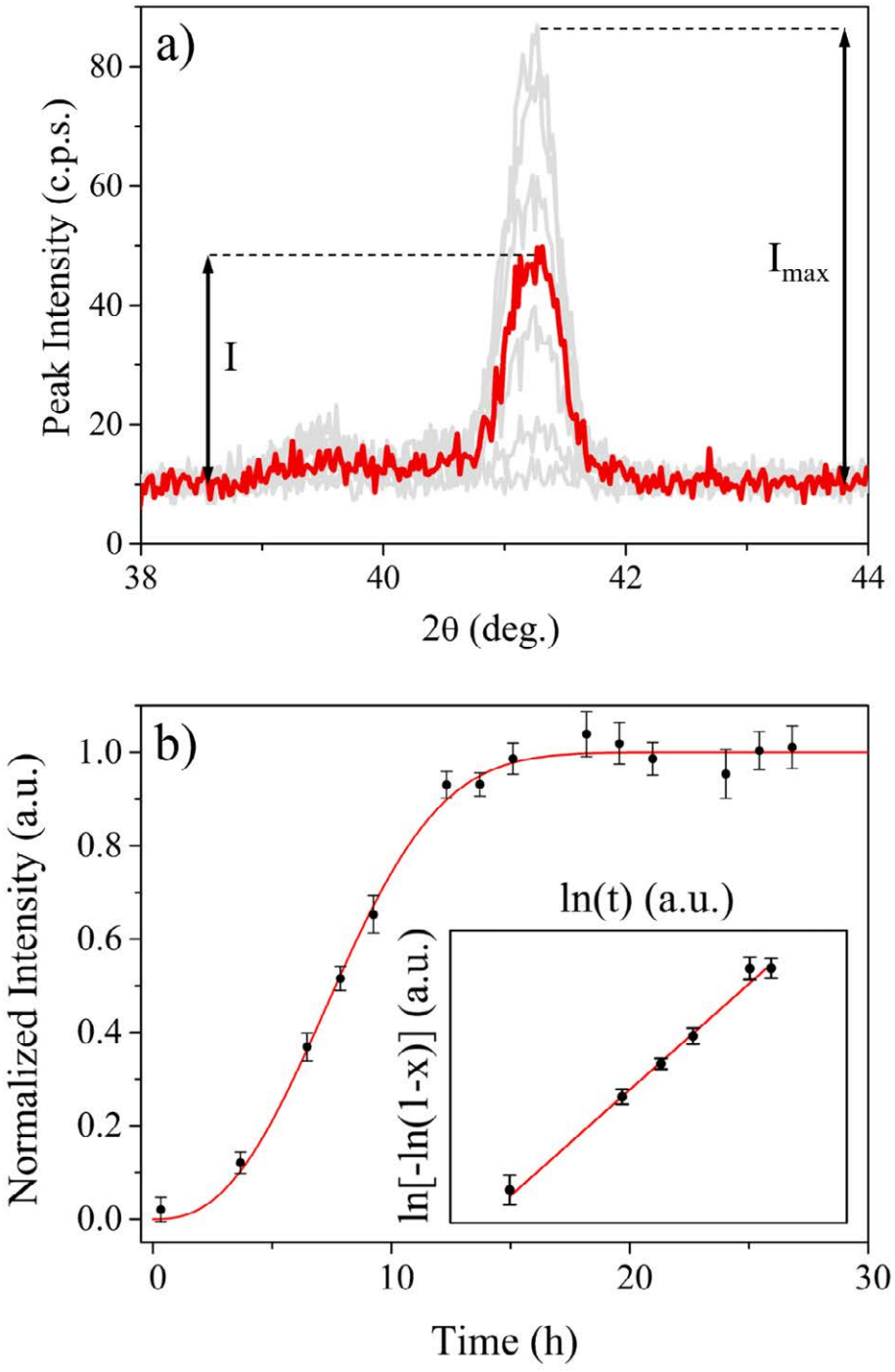

Figure 5.2: a) Definition of the crystallized volume fraction $x = I/I_{max}$ from XRD consecutive scans (from figure 3.5); b) normalized intensity of the (111) peak of IrMn as a function of time during the phase transition; the red line is a fit with equation 5.1; inset: linear fit to the double logarithmic plot $\ln[-\ln(1-x)]$ *vs* $\ln(t)$ from the data of b).

In this work, data about the crystallization process were collected in isothermal experiments at room temperature, by X-ray diffraction (XRD) and magnetometry measurements. Consecutive

XRD out-of-plane $\theta/2\theta$ scans were taken during the phase transition in the IrMn, and the results are shown in figure 3.5. The diffraction peak corresponding to the (111) reflection of the IrMn increases in intensity as the phase transition spreads in the IrMn layer. From this type of XRD measurements (see figure 5.2a), the crystallized volume fraction can be evaluated as $x = I/I_{max}$ [Zhang, 2006], where I is the integrated intensity of the diffraction peak during the crystallization and I_{max} is the averaged integrated intensity of the last ten scans, taken hours after the conclusion of the phase transition. A plot of x as a function of time is shown in figure 5.2b, where the black dots correspond to the data extracted from figure 3.5, and the red curve represents the best fit using equation 5.1. As expected, the data follow the sigmoidal shape typical of nucleation and growth processes. Note that the crystallization begins soon after deposition, without a proper incubation period, thus $\tau = 0$. From the fit using the JMAK equation a value of $n = 2.52$ is obtained. An estimation of the Avrami exponent can also be retrieved by evaluating the slope of a linear fit to the double logarithmic plot $\ln[-\ln(1-x)]\ vs\ \ln(t)$ [Mastai, 2012]. This plot is presented in the inset of figure 5.2b for values of x between 12% and 93%, and the linear fit gives a slope of $n = 2.41$.

According to the work of Očenášek et al. the crystallization process in thin films can be considered purely two-dimensional if $h < 0.17\bar{d}$, where h is the film thickness and $\bar{d}$ is the average grain size of the crystals [Očenášek, 2014]. This condition is here satisfied, since $h_{IrMn} \cong 15\ nm$ and $\bar{d} > 100\ nm$, as showed by the TEM analysis presented in chapter 3, and therefore the Avrami exponents can be estimated as $n_g \cong 2$ and $n_n \cong 0.4 - 0.5$, which indicate a two-dimensional growth process in presence of a decreasing nucleation rate.

The same kind of analysis can be performed starting from the magnetometry measurements presented in section 4.2.1. Consecutive hysteresis loops of IrMn/FeCo bilayers were measured during the phase transition in the IrMn, and the results are shown in figure 4.8. As time passes, the amount of the hysteresis loop which shows exchange bias increases, while the centered part of the loop decreases proportionally. As shown in figure 4.9, the bifurcated loop of figure 4.8 reflects the growth of exchange-biased domains in the FeCo layer. Hence, the crystallized volume fraction can be evaluated from magnetometry measurements as $x = M_{eb}/M_{tot}$, where M_{eb} is the magnetization of the part of the loop which shows exchange bias and M_{tot} is the total magnetization of the sample (see figure 5.3a). A plot of x as a function of time is shown in figure 5.3b, where the black dots correspond to the data extracted from figure 4.8, and the red curve represents the best fit using equation 5.1. Again, the data follow a sigmoidal shape,

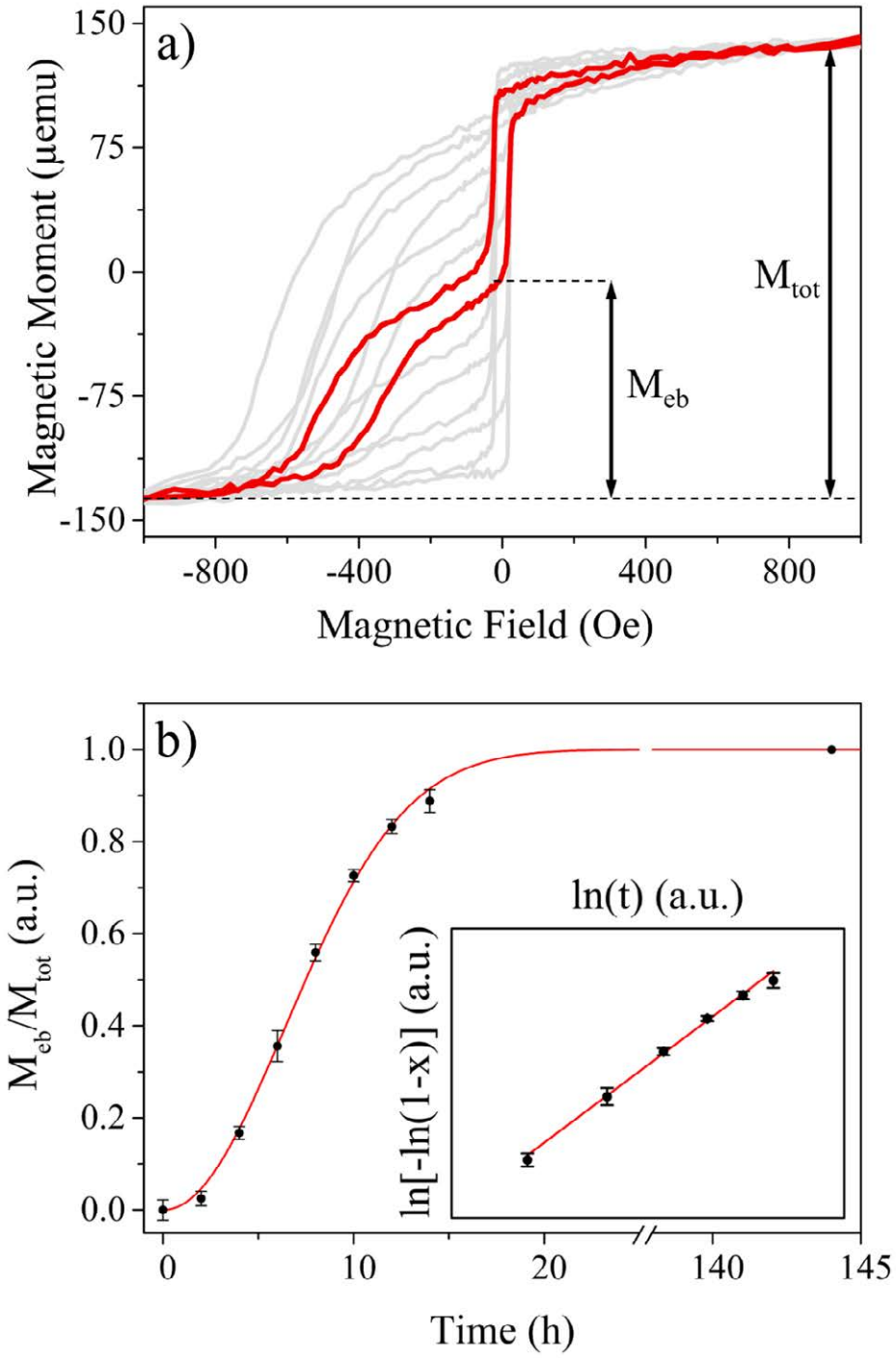

Figure 5.3: a) Definition of the crystallized volume fraction $x = M_{eb}/M_{tot}$ from consecutive magnetometry measurements (from figure 4.8); b) M_{eb}/M_{tot} as a function of time during the phase transition; the red line is a fit with equation 5.1; inset: linear fit to the double logarithmic plot $\ln[-\ln(1-x)]$ vs $\ln(t)$ from the data of b).

without a noticeable incubation period. From the fit using the JMAK equation a value of $n = 2.03$ is obtained. The double logarithmic plot $\ln[-\ln(1-x)]$ vs $\ln(t)$ is presented in the inset

of figure 5.3b for values of x between 17% and 89%, and the linear fit gives a slope of $n = 2.03$. Considering a purely two-dimensional growth, the Avrami exponents can be estimated as $n_g \cong 2$ and $n_n \cong 0$, which indicate a two-dimensional growth of nuclei formed during the deposition process.

In conclusion, the analysis of the kinetics of the crystallization of the amorphous IrMn confirms that it is a two-dimensional nucleation and growth process, in agreement with the TEM images taken during the phase transition (see figure 3.13). The mode of nucleation varies from sample to sample and it is probably influenced by factors such as the exact substrate temperature during deposition or small deviations in the IrMn composition and thickness, and by extrinsic factors, such as contaminants and defects. Nevertheless, the nucleation exponent is always found to be between zero and 0.5.

5.2 Planar defects in the crystallized IrMn

The structural characterization of chapter 3 and the study of the phase transition kinetics presented in the previous section, showed that the crystallization of the amorphous IrMn layer happens by a two-dimensional nucleation and growth process. The microstructural characteristics of the crystallized phase depends mainly on the mode of nucleation, which is influenced by the presence of defects and contamination by extraneous atomic species, and the type of growth of the nuclei, which in turn depends on the mobility of the atoms and the stoichiometry of the final phase with respect to the composition of the as-deposited material [Porter, 2009]. Indeed, nucleation and growth processes also depend strongly on the thermal energy provided to the material being in the metastable state. Hence, a systematic study of the microstructural properties of a crystallizing material is a challenging task that requires specific expertise and equipment, and, although such a study for the IrMn crystallization shown here would undoubtedly be interesting, it is beyond the scope of this thesis. Nevertheless, the interpretation of the magnetic data presented in the next section suggests that the microstructural defects present in the crystallized IrMn might play a pivotal role in the formation and the properties of the exchange bias of these bilayers. Thus, this section summarizes the analysis of the frequent planar defects which forms during the crystallization of the IrMn layer.

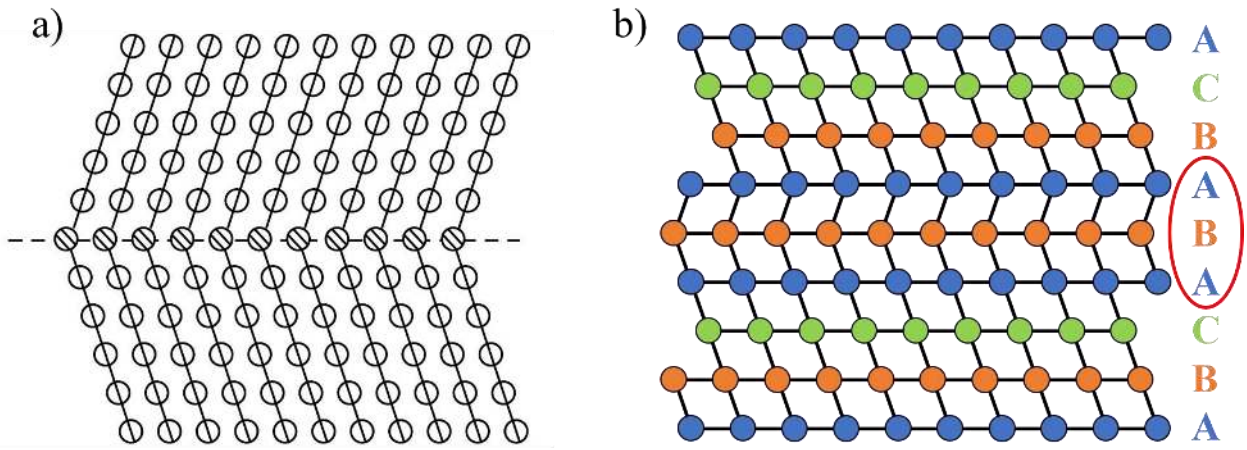

Figure 5.4: Schematic representation of a) coherent twinning, after [Porter, 2009], and b) stacking fault in fcc crystals.

A crystallographic defect is an irregular positioning of one or more atoms with respect to the perfect patterning defined by the crystal lattice [Phillips, 2001]. In crystallography, defects are organized according to their dimensionality: zero-dimensional, or point defect; one-dimensional, most commonly called dislocations; two-dimensional, or planar defects; and three-dimensional, or volume defects. Among these several irregularities of the crystal lattice, planar defects are the most important in crystalline engineering materials, but also the easiest to study thanks to their size and stationarity [Williams, 2009]. The formation of planar defects during solidification or crystallization of amorphous material is very common, and their nature and quantity depend on the kinetics of the phase transition process [Porter, 2009]. In materials where only one single crystalline phase is present, the possible planar defects are limited to twinning and stacking faults, whose structure is schematically represented in figure 5.4. Stacking faults are associated with mistakes in the stacking sequence of the crystalline planes in close-packed crystal structures, like fcc crystals (figure 5.4b) [Hirth, 1982]. Twinning takes place when two adjacent areas of a crystal are oriented with respect to each other according to some symmetry rule, and the boundary between them is referred to as the twin boundary (figure 5.4a) [Kelly, 2012]. A twin boundary can be the result of a particular type of stacking fault but it can also form at the boundary between two crystalline grains. Planar defects are generally studied by transmission electron microscopy (TEM), either in bright field (BF) and dark field (DF) mode, selective area diffraction (SAD) mode, or through high-resolution TEM (HRTEM) imaging [Williams, 2009].

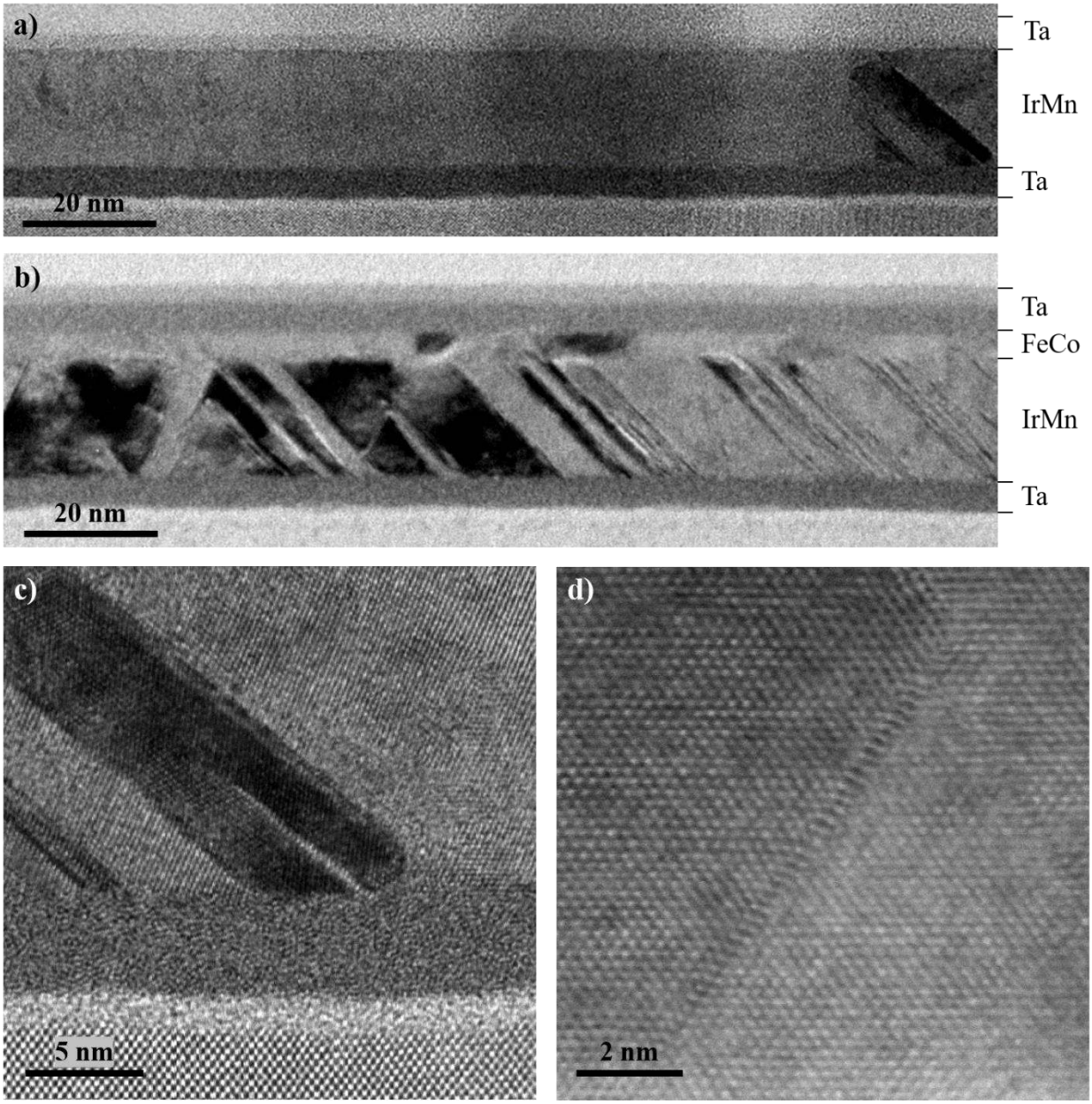

Figure 5.5: Cross-section TEM images of a) AF-type and b) AF/F-type samples; c) magnified view of the twin boundaries in the IrMn layer of the AF-type specimen; d) HRTEM imaging of one of the many stacking fault present in the AF/F-type sample

In this work, crystallographic defects were mainly analyzed by TEM and HRTEM in cross-section specimens with nominal structure Ta(3.5nm)/IrMn(15nm)/FeCo(5nm)/Ta(5nm) (AF/F-type) and Ta(3.5nm)/IrMn(15nm)/Ta(5nm) (AF-type), after the crystallization of the IrMn. Figure 5.5 shows bright field TEM images of an AF-type (a) and an AF/F-type (b) samples. The TEM images highlight the predominant presence of planar defects in the microstructure of the IrMn layer, which are visible at the boundaries between areas with different contrast. In these exemplary images it is evident that the IrMn in the AF/F-type sample

is studded with a much greater number of planar defects, which extend obliquely through the thickness of the IrMn layer. The AF-type specimen, instead, is almost flawless, with only an inclined defect on the right side of the TEM image, which is showed at higher magnification in figure 5.5c. The image indicates that this planar defect in the AF-type sample is the result of multiple twinning, as the crystalline order changes symmetrically at the defect boundary. Figure 5.5d shows an HRTEM image of one of the several planar defects detected in the AF/F-type specimen, which happens to be a stacking fault, resulting from an error in the stacking sequence of the (111) planes where the atomic order is clearly interrupted. Overall, the planar defects in the AF/F-type specimen are predominantly stacking faults which propagate through the whole thickness of the IrMn along the (111) planes.

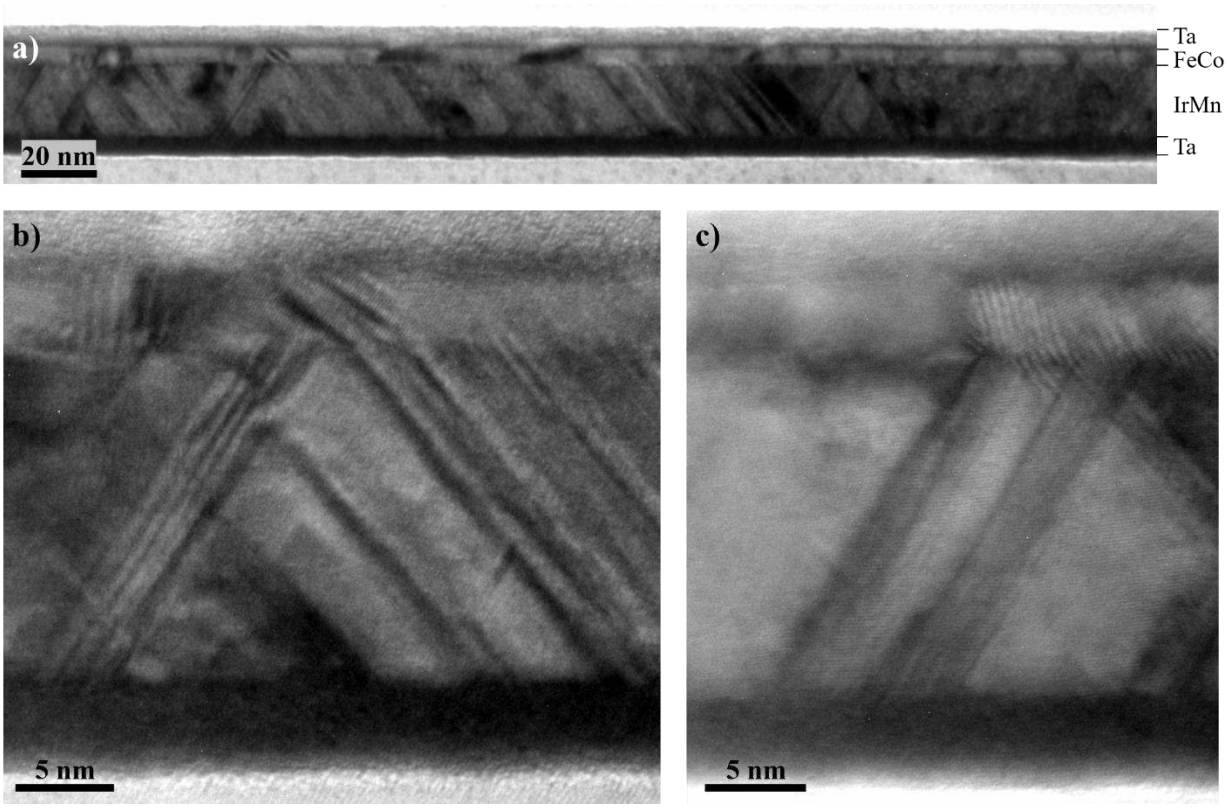

Figure 5.6: Bright field TEM image of a cross-section AF/F-type specimen; b) and c) magnified view of the typical fringes produced by stacking faults, in the IrMn layer.

The TEM images of figure 5.5 indicate that in AF/F-type samples the IrMn layer is likely to generate stacking faults during the phase transition from amorphous to γ-IrMn. In the AF-type specimens, instead, stacking faults, and planar defects in general, are almost absent. The formation of stacking faults is probably promoted by the presence of the polycrystalline FeCo layer adjacent to the amorphous IrMn. In AF-type samples, the crystallizing IrMn is in contact with amorphous Ta on both sides, and it is reasonable to assume that the atomic disorder of the

Ta layers does not influence the crystalline ordering of the IrMn. In AF/F-type samples, instead, the amorphous IrMn layer is also in contact with the FeCo layer, which is polycrystalline with small randomly oriented grains. It is therefore reasonable to assume that the order of the crystallizing IrMn may be affected by the adjacent FeCo grains, promoting the formation of defects at the IrMn/FeCo interface, which then propagates through the thickness of the IrMn layer.

The validity of these assumptions is strengthened by the bright-field TEM images of an AF/F-type specimen shown in figure 5.6. Due to diffraction effects, in this type of imaging stacking faults appear as a set of bright and dark fringes that run parallel to the planar defect direction [Fultz, 2013; Williams, 2009]. Figure 5.6 highlights the great number of planar defects that are present in the AF/F-type cross-section specimen throughout the IrMn layer (a) and presents two magnified views of the multilayer stack where the defects can be better appreciated (b and c). The images show the typical fringes produced by stacking faults that lay obliquely to the IrMn thickness. Fringed contrast is also present in the FeCo layer, possibly due to grain boundaries, in correspondence to the end of some of the stacking faults in the IrMn layer. This suggests that some orientations of crystalline grains of the FeCo layer, or the grain boundaries themselves, may have interfered with the crystallization process which arises in the IrMn, promoting the formation of stacking faults. Nonetheless, the magnetic exchange interaction between the FeCo spins and the ordering Mn atoms at the IrMn/FeCo interface may play a role as well, and such an option could not be ruled out.

In conclusion, the TEM analysis of cross-section specimens showed that, when the IrMn is in contact with the FeCo layer, the formation of stacking faults is promoted during the crystallization of the amorphous IrMn. The origin of this phenomenon seems to lay in the polycrystalline nature of the FeCo layer, which may affect the phase transition with its randomly oriented grains. This hypothesis is very interesting in light of the considerations which arise in the next section, according to which the planar defects play an important role in the magnetic and thermal properties of the exchange bias. In fact, controlling the microstructure of the FeCo layer by varying the deposition parameters may allow to tune the amount and the character of the planar defects in the crystallized IrMn, which would in turn influence the properties of the exchange bias.

5.3 The role of the IrMn crystallization on the exchange bias

As explained in the previous chapter, the York Protocol is the most suitable model to analyze the magnetic properties of IrMn-based exchange biased bilayers deposited by magnetron sputtering. This is confirmed by the several features and properties that the model is able to predict in this kind of samples [O'Grady, 2010]. Nevertheless, the thorough magnetic characterization presented in chapter 4 highlighted some discrepancies between the experimental results and the predictions of the York model. The phenomenology of these unexpected results is reported here in more detail, followed by a discussion on their interpretation, in light of the microstructural analysis presented in the previous sections.

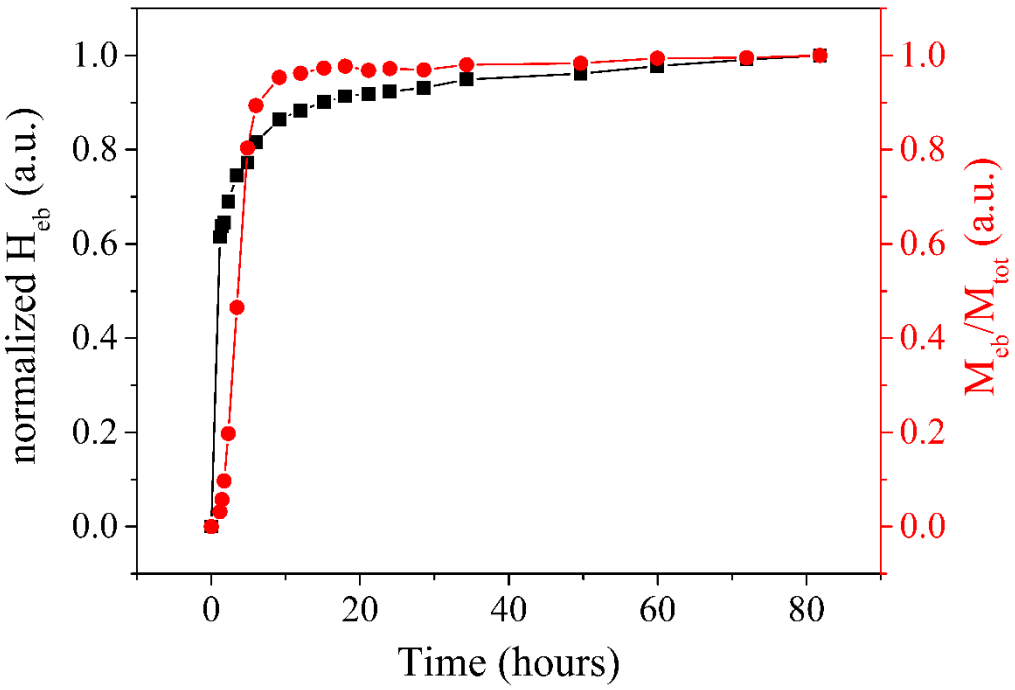

Figure 5.7: Normalized H_{eb} and crystallized volume fraction $x = M_{eb}/M_{tot}$ as a function of time of an as-deposited sample. Lines are a guide to the eye.

Increase of H_{eb} during the spontaneous setting. The spontaneous formation of the exchange bias was studied by consecutive magnetometry measurements, which are presented in figure 4.8. The results indicate that the initial setting of the exchange bias is caused by two distinct processes. As a consequence of the crystallization of the IrMn, the FeCo layer gets progressively exchange biased as the crystalline phase propagates, causing the bifurcated hysteresis loops shown in figure 4.8. In addition to this, the portion of the hysteresis loop which shows exchange bias shifts laterally with time, increasing the exchange bias field, H_{eb}. This

phenomenon is better shown in figure 5.7, where the normalized value of the exchange bias field and the crystallized volume fraction, $x = M_{eb}/M_{tot}$, are plotted as a function of time (see figure 5.3a for the definition of x). The crystallized volume fraction (red data in figure 5.7) varies according to the sigmoidal shape typical of the two-dimensional nucleation and growth processes (see section 5.1), and it saturates after 10-15 hours. The initial H_{eb}, instead, is about 60% of its final value, and it increases at a slower rate compared to the crystallized volume fraction, saturating only after 80 hours. In particular, the exchange bias field is at 85% of its final value when the crystallization is complete, and it keeps increasing for the remaining 65-70 hours. This increase indicates the concurrency of an additional process which progressively strengthens the exchange bias in the already crystallized areas of the sample. A similar phenomenon was observed by Paetzold et al. and Thomas et al. in NiO/NiFe bilayers [Paetzold, 2002; Thomas, 2003]. Their as-deposited samples showed an initial exchange bias field which increased spontaneously in the hours after the deposition.

A possible explanation for this phenomenon involves a progressive structural improvement of the already crystallized areas of IrMn, which would strengthen the exchange bias. This could be result of either a structural reorientation which promotes a better (111) texture, or the crystallization of smaller parts of the amorphous IrMn, whose phase transition was delayed by factors such as defects, contaminations or slow impingement of crystalline grains. In order to verify this scenario, consecutive XRD measurements were performed after the crystallization of the IrMn, and no structural improvement was detected in the period corresponding to the increase of H_{eb}. Nevertheless, small structural improvements in a 15-nm-thick polycrystalline thin film might not be easily detectable with XRD measurements, and this option cannot be ruled out completely.

Decrease of H_{eb} during the conventional setting. The magnetic response of IrMn/FeCo bilayers upon performing the conventional setting of the exchange bias following the York Protocol, is presented in figure 4.15. The data show that the exchange bias field initially remains constant but decreases sharply for setting temperatures higher than 410 K, as shown by the progressive loop shift toward positive fields presented in figure 5.8. The shape and the coercivity of the hysteresis loops remain virtually constant, whereas the exchange bias field decreases of about 25% upon increasing the setting temperature from 410 K to 500 K. This decrease of H_{eb} is counterintuitive, as thermal annealing should strengthen the exchange bias by optimizing the value of the exchange bias field. Paetzold et al. report the decrease of H_{eb} upon performing a field cooling procedure, which involved annealing the sample at 540 K (i.e.,

above the Neél temperature) for 20 minutes and then cooling to room temperature in a magnetic field of 1 kOe [Paetzold, 2002]. They also highlight that the value of H_{eb} after the field cooling is close to the initial value of the as-deposited sample, before the spontaneous increasing of H_{eb}.

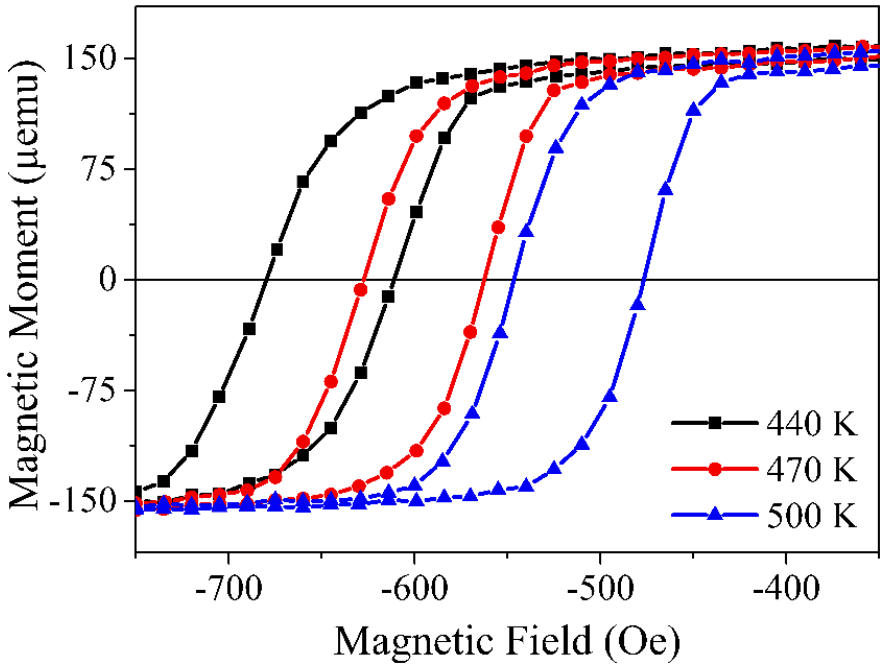

Figure 5.8: Magnetometry measurements taken after the EB setting at different temperatures. Lines are a guide to the eye.

Blocking temperature curve. Magnetometry measurements of IrMn/FeCo bilayers during a temperature dependent exchange bias relaxation experiment, performed according to the York Protocol, are presented in figure 4.18. The data show that the hysteresis loop shifts toward positive fields upon increasing the activation temperature, maintaining its shape and coercivity virtually constant. The resulting median blocking temperature, $<T_B>$, which corresponds to the activation temperature at which the exchange bias field goes to zero, is 460 K. From this value, the calculations performed according to the York model led to a median lateral grain size for the IrMn layer of 7.8 nm, which is evidently smaller than the average grain size suggested by the structural characterization presented in chapter 3.

The characteristics described here are unexpected and counterintuitive if interpreted in light of the sole granular model. Although our study did not highlight direct evidences of the phenomena which induce such behaviors in the samples, in the following sections we present

some hypotheses, based on indirect measurements, which could explain this unexpected phenomenology. The temperature dependent changes in the exchange bias, i.e. both the lowering of H_{eb} during the conventional setting and the low value of $<T_B>$, are described in light of a strong antiferromagnetic domain wall (AF-DW) pinning model, which allows the formation of multi-domain states and AF-DWs within each IrMn grain. We also propose a possible mechanism by which the exchange bias is set when the AF material undergoes an ordering phase transition, which would explain the initial increase of the H_{eb}.

5.3.1 Strong AF-DW pinning model for the exchange bias

The causes of these deviations from the standard response of IrMn/FeCo bilayers can be sought in the structural characteristics of the IrMn layer. In fact, the phase transition which arises in the IrMn is a feature unique to the samples studied in this work, whereas sputtering deposited IrMn is generally polycrystalline with relatively small grains. According to the York Protocol, these small IrMn grains are assumed to be single-domain that behave as Stoner-Wohlfarth entities [O'Grady, 2010]. Vallejo-Fernandez et al. suggests that the condition to have quasi-single-domain grains is a lateral grain size smaller than 20 nm [Vallejo-Fernandez, 2011a]. Contrarily, the structural characterization of chapter 3 showed the presence of grains with lateral grain size larger than 100 nm, whereas the calculation based on the data of the blocking temperature curve indicates that the magnetic volumes involved in the exchange bias are one order of magnitude smaller. These considerations suggest that the large IrMn grains can assume multi-domain states, due to the formation of AF-DWs within each grain. These multi-domains grains would not behave as Stoner-Wohlfarth entities, affecting the properties of the resulting exchange bias.

In spite of this, a pure multi-domain model for the exchange bias, such as the domain state (DS) model developed by Nowak et al. [Nowak, 2002], is not appropriate for the interpretation of the results presented here: firstly, the materials for which the DS model is able to predict the properties of the exchange bias are mainly diluted AF-oxides (CoO, CoMgO) [Keller, 2002; Miltényi, 2000; Fecioru-Morariu, 2010] and AF-flourides (FeF_2 and MnF_2) [Nogués, 2000]. Secondly, these samples are mostly produced by molecular beam epitaxy (MBE), which usually achieves extremely ordered structures due to its slow, atom-by-atom deposition, while the IrMn studied here is chemically disordered and consists of large grains studded with many planar defects. In addition, the application of the domain state model on IrMn-based exchange-

biased systems deposited by magnetron sputtering is not able to explain the several properties of the phenomenon, but for a qualitative explanation of the AF layer thickness dependence [Ali, 2003]. Hence, the DS model is not suitable for the present IrMn/FeCo system.

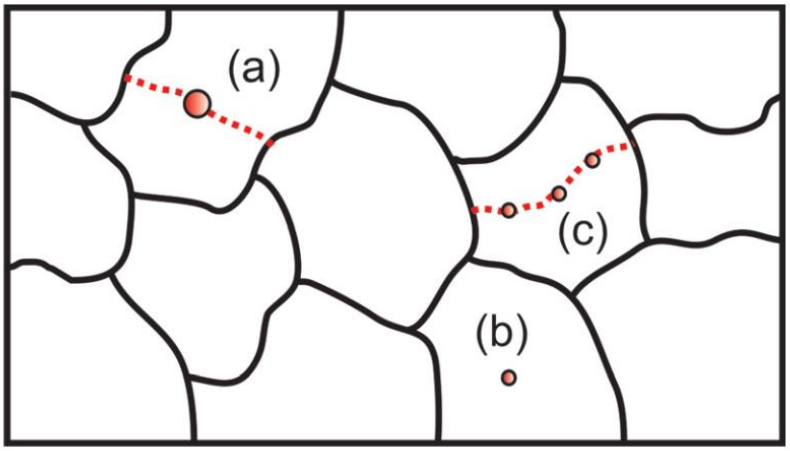

Figure 5.9: Schematic diagram of the microstructure of the AF layer, where AF-DWs (red dashed lines) are strongly pinned at defects and impurities (red dots) which lie within the large crystalline grains (black lines), after [Vallejo-Fernandez, 2011a].

In order to include the formation of multi-domain states within the IrMn grains and the presence of the several planar defects which propagate along their thickness, the data were analyzed according to the strong AF-DW pinning model developed by Vallejo-Fernandez et al. [Vallejo-Fernandez, 2011a; Vallejo-Fernandez, 2011b]. The model was originally proposed to explain the effects of defects and impurities in the AF layer of exchange-biased systems [Fecioru-Morariu, 2007; Aley, 2009; Mougin, 2000], and it consists in an extension of the York Protocol, in which AF domain walls can form and pin almost permanently at defects with strong pinning energy. Hence, a single grain can be divided in smaller AF volumes, whose dimension depends on the distribution of the pinned AF-DW (see figure 5.9). To simulate the presence of defects and impurities in the AF material, the model includes non-magnetic atoms randomly distributed across the sample. Each impurity is associated to a pinning energy, according to a lognormal distribution. A schematic diagram of the simulated microstructure of the AF layer is presented in figure 5.9. Depending on the amount of impurities and their pinning energy, there are three possible situations:

a) Defects with strong pinning energy can accommodate an AF domain wall which would divide the AF grains in smaller magnetic volumes. The critical pinning energy is taken as 30 $k_B T$.

b) Defects whose pinning energy is below the critical value are not strong enough to pin an AF domain wall, and therefore have no influence on the magnetic behavior of the grain.

c) When multiple defects are present in a given grain, if their combined pinning energy is above the critical value of 30 $k_B T$, an AF-DW can get pinned through them.

Hence, in samples with large grains and high density of defects and impurities, the properties of the exchange bias are determined by the AF volumes delimited by the pinned AF-DWs. These AF volumes are assumed to be independent from each other as long as the AF-DW are strongly pinned and their dimension determines whether they are in a single- or multi-domain state. According to the model, AF volumes with a lateral size smaller than 20 nm are considered single-domain, and hence behave as Stoner-Wohlfarth particles, whose reversal is well-described by the York Protocol. AF volumes with a lateral size larger than 20 nm, instead, are assumed to be multi-domain and therefore reverse via AF domain wall processes, resulting in a smaller contribution to the exchange bias field compared to the single-domain ones.

In this work, the simulations based on the strong AF-DW pinning model were performed directly by Dr. Vallejo-Fernandez. The parameters used in the simulations includes: $K_{AF} = 8 \times 10^6\ erg/cm^3$; average grain size after crystallization, 150 nm; standard deviation of the grain size distribution, assumed to be lognormal, 0.42; average value of the pinning strength at room temperature, 30 $k_B T$; standard deviation of the distribution of pinning energies, 0.35; thickness of the AF layer, 15 nm; defect concentration, ~1% of the volume; characteristic attempt frequency of $f_0 = 2.1 \times 10^{12}\ Hz$, as measured in ref. [Vallejo-Fernandez, 2010]; number of grains simulated to ensure good statistics, 10^4. The temperature dependence of the magnetocrystalline anisotropy is of the form $(1 - T/T_N)$, where $T_N = 690\ K$ is the Néel temperature of the bulk IrMn. The same temperature dependence was assumed for the pinning strength. The contribution to the exchange bias of a multi-domain volume is assumed to be 60% lower than that of a single-domain volume.

The results of the simulation of the blocking temperature curve using the strong AF-DW pinning model is shown in figure 5.10. The data correspond to those of the measurements presented in figure 4.18. The good quality of the fitting suggests that the model describes correctly the magnetic behavior of the IrMn layer, according to which the large crystalline IrMn grains are broken into AF domains, with the AF-DWs strongly pinned, possibly at the frequent structural defects visible in figures 5.5-5.6. Depending on their dimension, these AF domains

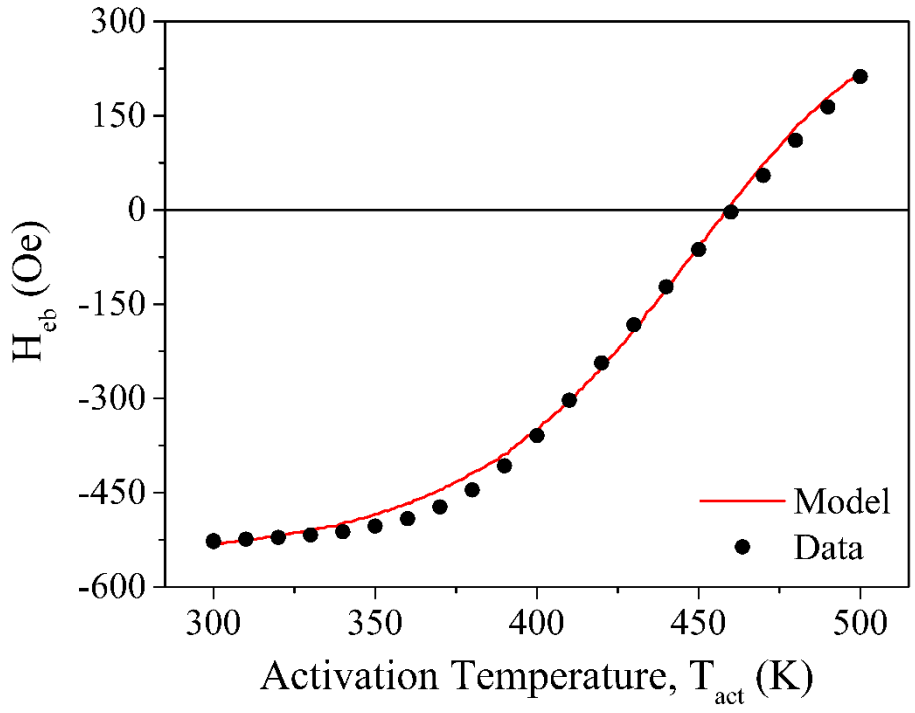

Figure 5.10: Fitting of the median blocking temperature curve using the strong AF-DW pinning model.

can be single- or multi-domain, with different contributions to the exchange bias. The size of the AF domains is such that the median blocking temperature is 460 K. In addition, as the activation temperature increases, some of these strongly pinned AF-DWs could become unpinned, giving rise to larger multi-domains that no longer follows the Stoner-Wohlfarth model during reversal. Since these domains would result in a lower contribution to the exchange bias, the unpinning of some AF-DWs explains the fact that at high temperatures the blocking temperature curve in figure 5.10, tends toward a value of H_{eb} which is smaller than the corresponding H_{eb} at low temperatures (~500 Oe).

Considerations based on the strong AF-DW pinning model can also help to explain the decrease of H_{eb} during the conventional setting of the exchange bias, shown in figure 5.8. It is reasonable to assume that the as-deposited IrMn, whose magnetic order is progressively set as the crystalline phase propagates, is in a metastable magnetic state, with misaligned small AF domains separated by lightly pinned AF-DWs, not mobile at room temperature. During the conventional setting of the exchange bias, as the temperature rises, these AF-DWs would be able to move and minimize their energy or get pinned at the defects which act as strong pinning sites. This process would change the average dimension of the AF volumes in the IrMn layer, influencing the properties of the exchange bias. According to the model, the decrease of 25%

in the H_{eb} shown in figure 5.8 might be the result of two distinct situations. In the first scenario, the thermal activation of the AF-DWs would lead to a decrease of the average dimension of the AF volumes, with some of which being too small and therefore unstable, according to the York model, generating no exchange bias. This circumstance is not probable as the non-activation temperature, T_{NA}, was unaltered after the conventional setting, which means that the whole IrMn layer actively contributes to the exchange bias. In the second and most likely scenario, instead, the activation of the AF-DWs would lead to an increase of the average dimension of the AF volumes, with some of which passing from being single-domain to multi-domain, and therefore lowering their contribution to the exchange bias, according to the strong AF-DW pinning model. In this scenario, considering that in the model the contribution to the exchange bias of a multi-domain volume is assumed to be 60% lower than that of a single-domain volume, and assuming that initially the whole volume of the IrMn contributes to the exchange as a single-domain state, a decrease of 25% in the H_{eb} would imply the formation of multi-domain states corresponding to 40% of the IrMn volume.

Finally, a possible explanation of the increase of H_{eb} during the initial spontaneous setting of the exchange bias (see figure 5.7) involves the lightly pinned AF-DWs formed during the crystallization of the IrMn, which were discussed above. According to the pinning model, the exchange bias field could improve if the AF-DWs that form during the crystallization could move at room temperature, leading to the enlargement of some small, thus unstable, AF volumes. These enlarging volumes could progressively become stable at room temperature, inducing a stronger exchange bias. Although reasonable, this situation seems unlikely because it assumes that the AF-DWs are mobile at room temperature, a thing which would reduce the thermal stability of the exchange bias. Contrarily, the room temperature EB relaxation experiment, presented in figure 4.14, showed a good thermal stability of the as-deposited samples, with a decrease of H_{eb} of about 19% in the first 80 hours, compared to the initial increase which is about 66% in the same period of time (see figure 5.7). Nevertheless, this option cannot be ruled out completely because the effects of the crystallization and the spontaneous increase of H_{eb} cannot be decoupled in the initial stage of the measurements (first 10 hours of figure 5.7), and the initial increase of H_{eb} could be partially due to the ongoing structural transformation.

5.3.2 A new mechanism for the initial setting of the exchange bias

In this part we propose a possible mechanism for the initial setting of the exchange bias, as the ordering phase transition of the AF material propagates, which would explain the initial increase of the H_{eb}. Although we could not retrieve direct evidences of the assumptions advanced here, we believe that a discussion based on indirect measurements could improve the understanding of the phenomenon. In order to better introduce the proposed mechanism, we initially present the results of structural and magnetic characterization of a peculiar set of samples, which shows mixed crystallographic texture.

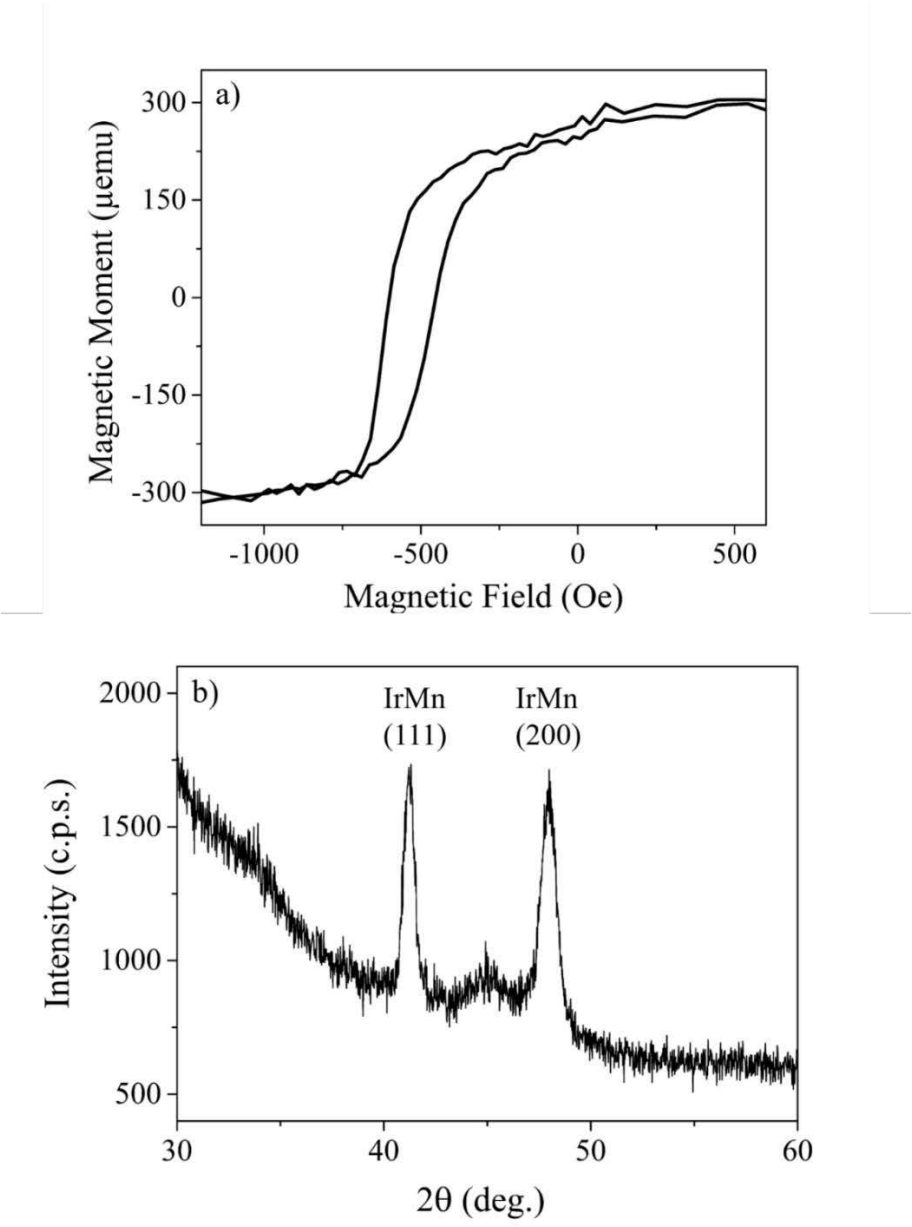

Figure 5.11: a) Magnetometry measurement and b) out-of-plane $\theta/2\theta$ XRD scan of an AF/F-type sample showing mixed (111) and (100) texture.

As explained in section 3.2.4, the (111) texture of IrMn is considered extremely important for technological applications since many studies confirmed that it promotes a higher exchange bias field [Hoshino, 1996; Pakala, 2000; Anderson, 2000]. Consequently, the influence of the material used as seed layer on the texture of the IrMn has been thoroughly studied over the years [Hoshino, 1996; van Driel, 2000; Anderson, 2000; Aley, 2008]. However, the results are sometimes contradictory, and few studies also indicate that the (111) texture does not affect the strength of the exchange bias [Devasahayam, 1998; Yagami, 2001]. Although most of the samples presented in this work include a Ta seed layer to promote the (111) texture of IrMn, according to results of van Driel et al. [van Driel, 2000], we also showed that the IrMn crystallizes with a high (111) texture even in absence of seed layer, i.e. directly deposited on SiO_2 (see section 3.2.4). However, even though the quasi-totality of the samples deposited in this work is (111) textured, a very few of the AF/F-type samples deposited over a Ta seed layer resulted to have a mixed (111) and (100) texture.

The magnetic and structural characterization of one of these samples is presented in figure 5.11. The out-of-plane $\theta/2\theta$ XRD scan (b) shows two intense diffraction peaks, respectively at $2\theta = 41.24°$ and $2\theta = 47.96°$, which correspond to the IrMn (111) and (200) reflections. Note that, as the IrMn is chemically disordered, the (100) diffraction is forbidden and therefore only the (200) peak is detected. Contrarily to the expectations, the magnetometry measurement (a) shows a good exchange bias, with $H_{eb} = -527\ Oe$, and a coercivity of $74\ Oe$. These values are comparable to the ones of (111) well-textured samples presented before.

In order to investigate the origin of this anomalous (100) texture and to clarify its role in the generation of a strong exchange bias, we performed scanning TEM (STEM) imaging at the IrMn/FeCo interface in a cross-section specimen. Figure 5.12a shows a high-angle annular dark-field (HAADF) STEM image, where the IrMn part is brighter due to the higher atomic number of the Ir (for a brief explanation of the HAADF-STEM imaging technique see section 2.2.2). This image is purposely zoomed at a well-distinguishable interface defect, highlighted by the yellow line. As shown by the black lattice orientation diagram superimposed, the IrMn is indeed (100) textured, although with a misalignment of 7°. Consequently, the dashed lines which define part of the interface, do not correspond to a specific lattice plane. Nevertheless, the full part of the line lies parallel to the (111) lattice plane, as shown by the yellow part of the lattice orientation diagram.

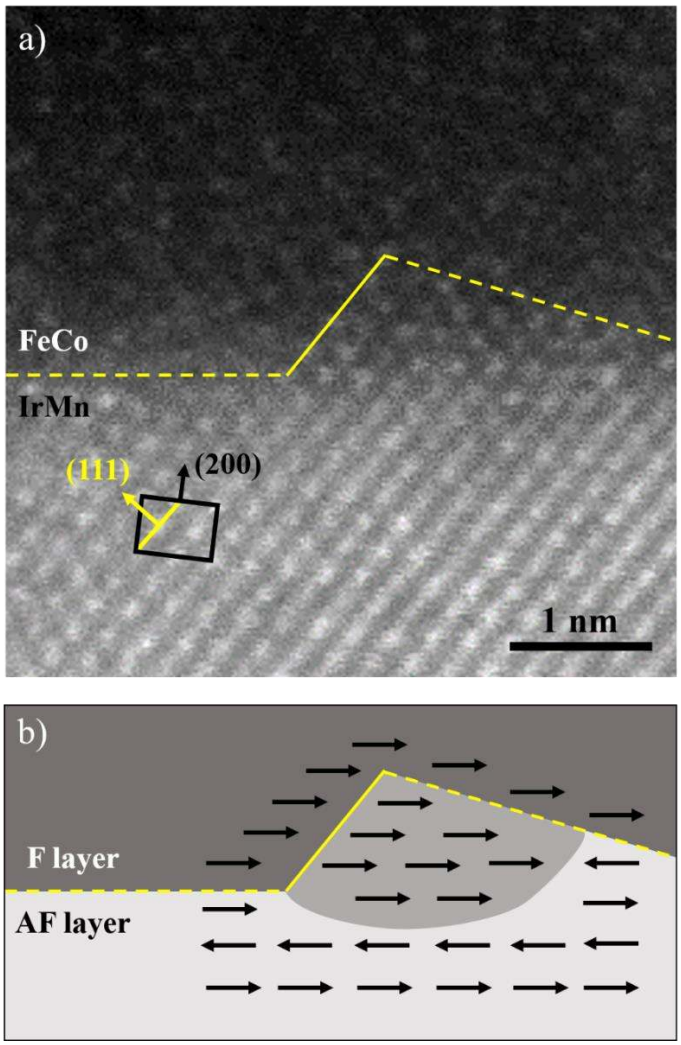

Figure 5.12: a) HAADF-STEM image at atomic resolution of the IrMn/FeCo interface in (110) zone axis; b) schematic diagram of a possible magnetic configuration due to the interface roughness.

Hence, although the IrMn is preferably (100) oriented, a moderate interface roughness can generate an IrMn/FeCo interface along the (111) lattice plane of the IrMn, whose contribution to the exchange bias is stronger. This may explain why, although these samples present a mixed texture, their exchange bias field is as high as the (111) well-textured samples.

Figure 5.12b shows a graphic illustration of the interface defect and a possible magnetic configuration, represented by the black arrows, where the medium-toned gray-colored area corresponds to an interfacial ferromagnetic cluster in the AF material. Because of the direct exchange coupling with the F material both at left and right of the interface defect, the formation of a ferromagnetic cluster could be energetically favorable. The presence of interfacial ferromagnetic clusters in exchange-biased system has already been inferred experimentally, based on several measurements performed using the York Protocol, by the group of Prof. K. O'Grady [O'Grady, 2010]. They showed that spin clusters analogous to a

spin glass are formed in the AF grains at temperatures below 25 K (see figures 20 and 21 in ref. [O'Grady, 2010]), and are responsible for interfacial processes that can occur independently of the AF ordered material.

The explanation for the increase of H_{eb} during the spontaneous formation of the exchange bias proposed here is based on a mechanism for the initial setting of the exchange bias, which involves the interfacial spin clusters. During the crystallization of the IrMn, factors such as the low mobility of atoms at room temperature or the impingement of growing crystalline grains, inevitably induce a series of non-ideal atomic arrangement in the resulting crystallized material, e.g. mechanical tensions, crystallographic defects or high interface roughness. As the crystalline phase propagates, the magnetic ordering of the crystallizing IrMn can be influenced by these factors, as exemplified by the presence of a spin cluster in correspondence of an interfacial defect in figure 5.12b. When this happens, some magnetic moments at the IrMn/FeCo interface may settle strongly pinned, causing the initial loop shift which forms during the crystallization of the IrMn. Then, driven by direct exchange interaction and promoted by thermal activation at room temperature, this strongly pinned area may expand slightly, forming a cluster-like magnetic structure. As the spin cluster grows, the interfacial ferromagnetic areas adjacent to the ordering spins progressively strengthen their exchange-bias in the hours after the crystallization of the IrMn. This microscopic mechanism is reflected macroscopically by an appreciable increase of H_{eb} in the already crystallized samples.

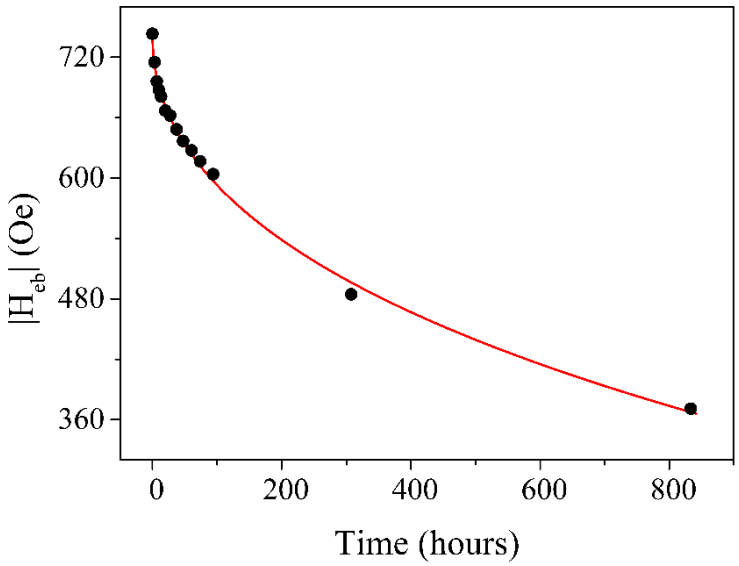

Figure 5.13: Decay of H_{eb} as a function of time during an exchange bias relaxation experiment at room temperature. The red line represents the fit to the data using equation 5.2.

In support to the validity of this assumptions we present a couple of indirect measurements which indicate the presence of these strongly pinned spin clusters. Firstly, we analyzed the room temperature exchange bias relaxation experiment presented in figure 4.14, in light of the work of Xi et al. [Xi, 2007]. They elaborated a theoretical model, partially based on the JMAK one (see section 5.1), to explain the relaxation of the exchange bias field as

$$H_{eb}(t) = H_{eb}^{0}\{2 \cdot \exp[-(t/\tau)^{\beta}] - 1\} \qquad (5.2)$$

where H_{eb}^{0} is the initial value of the exchange bias field, t is time, τ is a relaxation constant and β is the exponent factor which determine the type of magnetic relaxation. The result of the fit to our experimental data using Xi's model is shown by the red line in figure 5.13, and values for $\beta = 0.47$ and $\tau = 11{,}225\ h$ were obtained, with a standard error of 1.6 % for β and 6 % for τ. Since the value of β associated to spin glass relaxation at the spin-glass transition temperature is 1/3 [Phillips, 1996], the slightly larger value of $\beta = 0.47$ obtained from the reversal experiment could indicate a relaxation of spin glass at room temperature, well above the spin-glass transition temperature, which is below 25 K according to Prof. O'Grady's results [O'Grady, 2010].

A second indirect evidence that indicates the presence of strongly pinned areas in the crystallized samples comes from magnetic force microscopy (MFM) measurements. Figure 5.14 shows MFM images of one of the AF/F-type sample where the exchange bias direction was patterned by switching the remanent magnetization of the FeCo layer during the phase transition in the IrMn (see figures 4.10-4.11). The images are taken in presence of an external magnetic field applied parallel to the direction of exchange bias, and the difference in contrast between the central area and the "side bands" highlights that the exchange bias is directed in opposite directions. At zero-applied field the magnetic structure of the domain walls which separate the two oppositely directed areas is in evidence. In addition to that, we also note the presence of dark dotted features located far from the boundaries between the areas with opposite exchange bias, as shown by the black arrow in figure 5.14. These features gain intensity when the field is applied in the direction opposite to the exchange bias. As there is no correlation between the topographic images and these dotted features, the origin of such a dark contrast is purely magnetic. In these dots, there is a large stray field coming out of plane, enhanced when the external field is magnetizing against the direction of exchange bias. Therefore, these dots may mark areas where the magnetization is strongly pinned in the direction of the exchange bias, revealing where these hypothetical spin clusters are located.

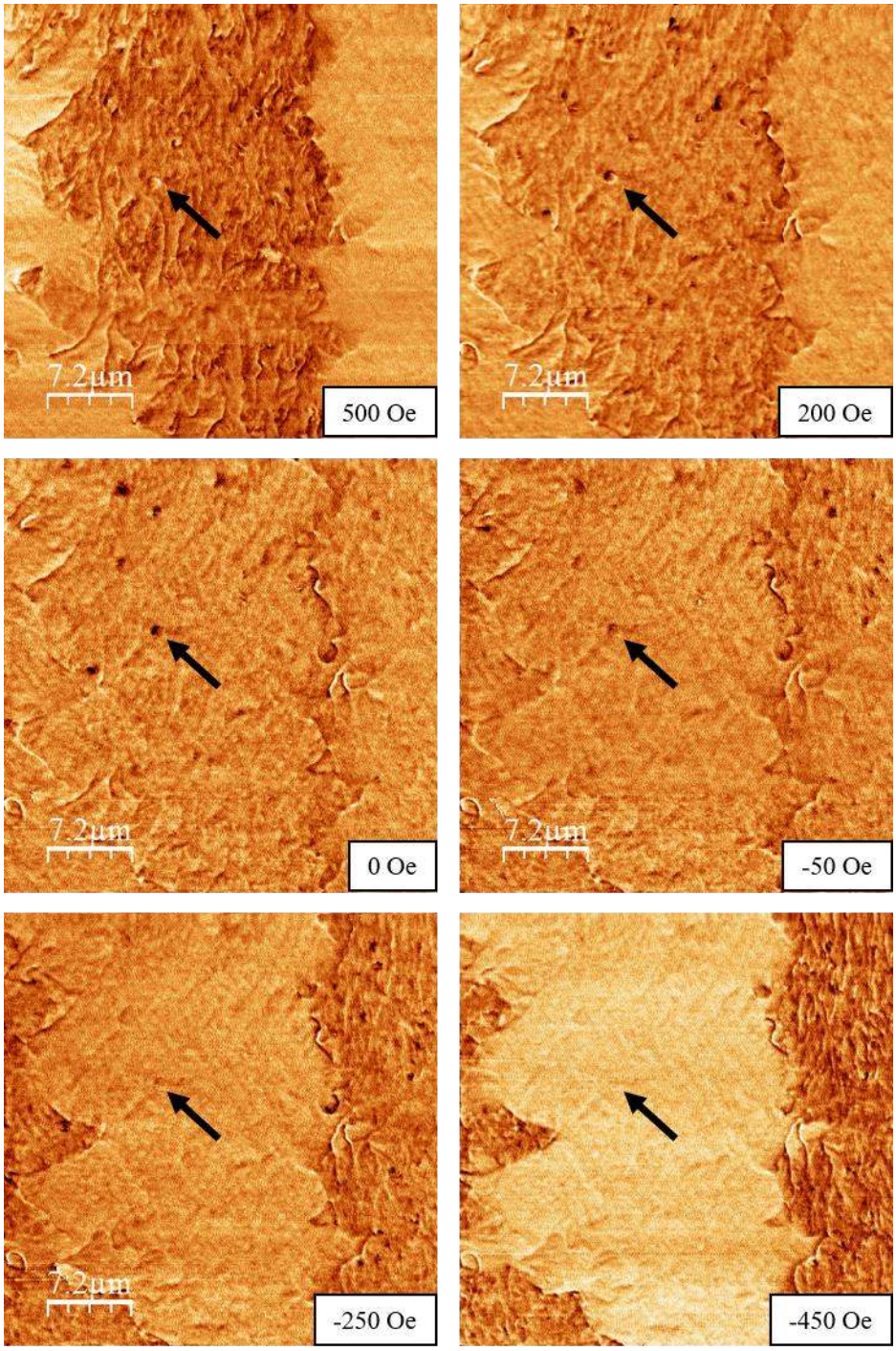

Figure 5.14: MFM images of an AF/F-type sample with patterned exchange bias, taken at different values of the external field.

5.4 Conclusions

In this chapter, we treated the effect of the crystallization of the amorphous IrMn layer on the magnetic and thermal properties of the exchange bias developed in bilayers with generic

structure SL/IrMn(15nm)/FeCo(5nm)/CL. In the previous chapters, the IrMn layer of these samples was shown to undergo a phase transition whose characteristics have never been studied before. The magnetic response of the crystallized samples also showed some deviations from the predicted behavior, according to the York Protocol. In order to explain these behaviors, we analyzed the experimental results, including the study of the microstructure of the IrMn, in light of a strong AF-DW pinning model. We also proposed a physical mechanism for the initial setting of the exchange bias when the AF material undergoes a phase transition, which can explain the characteristics of the spontaneous formation of the exchange bias.

The kinetics of the crystallization of the IrMn layer was studied in isothermal conditions by analyzing the experimental data collected during the phase transition (section 5.1). The analysis was performed by extracting from the data the crystallized volume fraction as a function of time and fitting it with the Johnson-Mehl-Avrami-Kolmogorov (JMAK) model (equation 5.1). The volume fraction could be evaluated from XRD out-of-plane $\theta/2\theta$ scans (figure 5.2) and from magnetometry measurements (figure 5.3) taken during the phase transition in the IrMn. Both the sets of data led to a growth exponent $n_g \cong 2$, which indicates a two-dimensional growth process. The nucleation exponent was respectively $n_n \cong 0.5$ and $n_n \cong 0$ for the first and the second sets of data. Hence, in the first sample the nucleation rate decreased with time, whereas in the second one, the nucleation occurred entirely during the deposition process.

The analysis of the microstructure of the crystallized IrMn was performed by TEM and HRTEM in both AF-type and AF/F-type cross-section specimens (section 5.2). The images showed that the AF-type specimen is almost flawless, with only some twin boundaries, whereas the AF/F-type one is studded with stacking faults which extend through the thickness of the IrMn layer (figure 5.5). Bright-field TEM imaging suggests that these frequent planar defects in the AF/F-type samples have their origin in the polycrystalline nature of the FeCo layer (figure 5.6). The presence of the randomly oriented FeCo grains adjacent to the amorphous IrMn could in fact influence its ordering during the phase transition, inducing stacking faults at the IrMn/FeCo interface, which then propagate along the (111) planes through the whole thickness of the IrMn layer.

Finally, we attempted to elaborate a reasonable interpretation of the deviations in the magnetic behavior from the predictions of the York Protocol (section 5.3). Since the crystallization of the IrMn in AF/F-type samples leads to the formation of large crystalline grains with frequent planar defects which lay obliquely to the thickness of the layer, a strong AF-DW pinning model

is an appropriate choice to describe the magnetic behavior of the bilayers. According to the model, the large IrMn grains are broken into AF domains, whose DWs lay along the structural defects which act as strong pinning sites (figure 5.9). Hence, the magnetic volume which determines the properties of the exchange bias is not the whole grain volume, but the smaller AF domain volumes, whose dimension depends on the positioning of the AF-DWs. Depending on the size of these AF volumes, they may behave as quasi-single-domain entities, reversing according to the York Protocol, or as multi-domain entities, reversing via AF domain wall processes, which results in a smaller contribution to the exchange bias.

Simulations performed using this model allowed to fit the blocking temperature curve measured according to the procedures of the York Protocol (figure 5.10). Hence, the small value of the median blocking temperature (460 K) is due to the fragmentation of the IrMn grains in smaller AF domains, whose thermal stability is lower compared to the entire grains. The decrease of H_{eb} during the conventional setting of the exchange bias is a counterintuitive effect, since thermal annealing should strengthen the exchange bias according to the York Protocol (figure 5.8). To explain this phenomenon, we assumed that the as-deposited IrMn is in a metastable magnetic state, with misaligned small AF domains separated by lightly pinned AF-DWs. During the thermal annealing, these AF-DWs would be able to move, resulting in an increase of the average dimension of the AF volumes, with some of which passing from being single-domain to multi-domain, and therefore weakening the final exchange bias.

Finally, we proposed a new mechanism for the initial setting of the exchange bias, which can explain the increase of H_{eb} in the time after the crystallization of the IrMn (figure 5.7). We started by analyzing the structural and magnetic characterization of few samples which show mixed (111) and (100) texture in the IrMn (figure 5.11). Interestingly, the strength of the exchange bias in these samples is comparable to the exchange bias of the (111) well-textured samples. The analysis by HAADF-STEM imaging of the IrMn/FeCo interface showed that the interface roughness can promote the presence of (111) texture in part of the interface, even in (100) textured areas (figure 5.12). We considered that at this interface defects, a F-oriented spin cluster can form, due to direct exchange coupling with the F layer. The slow formation at room temperature of these interfacial spin clusters can explain the increase of H_{eb} in the time after the crystallization of the IrMn. We have provided indirect evidences which strengthen the validity of these assumptions. The room temperature exchange bias relaxation of our samples can be fitted with Xi's model, giving a value of $\beta = 0.47$ which could indicate a relaxation of spin glass at a temperature higher than the spin-glass transition temperature (figure 5.13). In

addition, MFM imaging highlighted the presence of strongly pinned areas which might be due to the predicted spin clusters (figure 5.14). Nevertheless, further characterization is required to test the validity of the proposed mechanism for the initial setting of the exchange bias.

Chapter 6: Conclusion

The results obtained in this thesis work can be organized in two categories. The structural results, related to the study of the phase transition which occurs in the IrMn layer, are mostly described in chapter 3. The magnetic results, which include the spontaneous formation of the exchange bias and its thermal properties, can be found in chapter 4. Nevertheless, in chapter 5 we have shown that these results are strongly correlated, and that the structural properties of the crystallized IrMn may influence the mechanism by which the exchange bias is established, with important consequences on the quality of the resulting exchange bias. This chapter aims to summarize all these experimental and interpretative results in a coherent and comprehensive picture of the spontaneous exchange bias formation driven by a structural phase transition in the AF material.

6.1 Results

The specimens investigated in this research work are multilayered thin films deposited by magnetron sputtering, with nominal structure SL/IrMn(15nm)/FeCo(5nm)/CL (AF/F-type) and SL/IrMn(15nm)/CL (AF-type). The seed layer is Ta(3.5nm), when present, whereas the capping layer is either Cu(7nm)/Pt(1.5nm) or Ta(5nm), depending on the measurements to be performed. The samples were deposited over naturally oxidized Si(100) substrates, thermally oxidized Si(111)/SiO_2 substrates and TEM grids. All the materials are grown at high deposition rate by DC magnetron sputtering, except for the IrMn layer, which is deposited by RF magnetron sputtering, from a target of nominal composition $Ir_{25}Mn_{75}$. Nevertheless, EDS measurements showed that the actual composition of the sputtered material is $Ir_{30}Mn_{70}$.

Although deposition by magnetron sputtering generally leads to polycrystalline materials, at these sputtering conditions the as-deposited IrMn is mainly amorphous with some randomly oriented nanocrystalline grains. The shaded annular pattern detected by plan-view SAD imaging clearly indicates that the IrMn is mostly amorphous, while plan-view TEM imaging highlights the presence of scattered nanocrystalline grains within the amorphous material. GID-XRD scans indicates that these small grains are randomly oriented. The rapid growth of the IrMn by RF magnetron sputtering is most likely the responsible of its deposition in form of a glassy alloy. The Ta layers are amorphous, whereas the FeCo layer is polycrystalline with small randomly oriented grains. As-deposited AF/F-type samples with amorphous IrMn show no

exchange bias, according to magnetometry measurements, which are characterized by a centered hysteresis loops with low coercivity.

The glassy form of the as-deposited IrMn is metastable and, at room temperature, the 15-nm-thick IrMn layer has sufficient thermal energy to undergo an ordering structural transformation, from amorphous to crystalline. This crystallization is recorded in a sequence of plan-view TEM images, which shows the dendritic growth of the crystallites. Since the crystallized IrMn is (111) textured, the structural change is also detected by consecutive out-of-plane $\theta/2\theta$ XRD scans, which reveal a progressive development of the initially absent (111) diffraction peak. TEM imaging and GID-XRD measurements show that, as the crystalline phase of the IrMn propagates, the scattered nanocrystalline grains are reoriented. The phase transition of the IrMn occurs independently of the presence of the FeCo layer or the Ta seed layer. In both cases, the crystallized IrMn is very well-textured in the (111) direction. The phase transition in the IrMn is accompanied by a progressive formation of the exchange bias in AF/F-type samples. Consecutive magnetometry measurements and Kerr microscopy imaging show that the FeCo layer gets progressively exchange-biased as the crystalline phase of the IrMn develops. The magnetometry measurements also highlight an increase of the exchange bias field in the hours after the crystallization of the IrMn. Analysis of the data in light of the Johnson-Mehl-Avrami-Kolmogorov (JMAK) model confirms that the crystallization happens according to a two-dimensional nucleation and growth process. In general, the crystallization of the IrMn may take from few hours to several days.

Thorough structural characterization of the samples after the phase transition indicates that the IrMn is in a highly crystalline chemically-disordered γ-phase. The exact phase was identified through in-plane $\varphi/2\theta_\chi$ XRD scans, plan-view SAD imaging, cross-section SAD imaging and HAADF-STEM imaging. Dark-field imaging of cross-section specimens highlights the presence of grains larger than 100 nm, with extended defects that propagate through the entire thickness of the IrMn layer. A detailed TEM study of these planar defects indicates that the presence of the polycrystalline FeCo layer promotes the formation of stacking faults in the crystallizing IrMn. The crystallized AF/F-type samples are characterized by a loop shift of the order of 600 Oe, which implies an interfacial exchange energy of about $J_K = 0.51\ erg/cm^2$, and a coercivity of about 75 Oe. The crystallized samples show only a mild training effect, which scales with ln(N), and are quite stable upon performing a prolonged reversal experiment at room temperature, with a decrease of the exchange bias field of about 50% after 35 days. As the direction of the exchange bias is defined by the remanent magnetization of the FeCo layer,

we also demonstrated that a patterning of the exchange bias is possible by simply switching the remanence of the FeCo layer as the crystalline phase of IrMn propagates.

The standard setting of the exchange bias, performed according to the York Protocol, showed the unexpected lowering of the exchange bias field, together with a decrease of the coercivity and the improvement of the hysteresis loop shape. In addition, the temperature-controlled activation of the AF layer led to a median blocking temperature of 460 K, which implies an estimated value for the median lateral grain size of D_m = 7.8 nm, more than one order of magnitude smaller than the effective grains size detected by TEM imaging. In order to interpret these results, we employed a strong AF-DW pinning model which assumes that the large IrMn grains are broken into AF domains, whose DWs lay along the structural defects which act as strong pinning sites. Simulations allowed to fit the blocking temperature curve, which is an indication that the IrMn grains are fragmented in smaller AF domains, whose thermal stability is lower compared to the entire grains. A possible explanation of the lowering of H_{eb} during the conventional setting of the exchange bias, involves the assumption that the as-deposited IrMn is in a metastable magnetic state, with misaligned small AF domains separated by lightly pinned AF-DWs. These AF-DWs can move as long as they are given thermal energy during the annealing, resulting in an increase of the average dimension of the AF volumes and therefore weakening the final exchange bias.

Although the quasi-totality of the samples deposited in this work is (111) textured, a very few AF/F-type samples developed a mixed (111) and (100) texture and their exchange bias show a strength comparable with the (111) well-textured samples. HAADF-STEM imaging of the IrMn/FeCo interface shows that the interfacial roughness can promote the (111) texturing even in (100) textured areas. These interfacial defects, may promote the formation of F-oriented spin clusters which would critically contribute to the strength and the thermal stability of the exchange bias. Hence, we proposed a new mechanism for the initial setting of the exchange bias. The non-ideal atomic arrangement at the IrMn/FeCo interface, due to mechanical tensions, crystallographic defects or high interface roughness, inevitably induced by the crystallization of the IrMn, may host strongly pinned magnetic moments as soon as the IrMn crystallizes, causing the initial hysteresis loop shift. Driven by direct exchange interaction and promoted by thermal activation at room temperature, this strongly pinned area may expand slightly, forming a spin cluster. As these spin clusters grow, the interfacial ferromagnetic areas adjacent to the ordering spins progressively strengthen their exchange-bias in the hours after the crystallization of the IrMn. This microscopic mechanism is reflected macroscopically by

an appreciable increase of H_{eb} in the hours after the crystallization has finished covering the entire surface of the sample. The analysis of the exchange bias relaxation of as-deposited AF/F-type samples, performed at room temperature, in light of Xi's model, gives a value of $\beta = 0.47$, which could indicate the relaxation of spin glass at a temperature higher than the spin-glass transition temperature. In addition, MFM imaging highlighted the presence of strongly pinned areas which might be due to the predicted spin clusters. Although these results provide indirect evidences of the presence of the strongly pinned spin clusters, further characterization is required to test the validity of the proposed mechanism for the initial setting of the exchange bias.

6.2 Future works

Many of the experimental results presented in this research work have never been reported in the scientific literature before, including the deposition of amorphous IrMn, the crystallization of glassy IrMn at room temperature, the consequent spontaneous formation of the exchange bias, as well as the selective patterning of the exchange bias during a phase transition in the AF material. Although the present work has indubitably the merit of having characterized the phenomenon, laying the foundations for further research on this topic, there still are many aspects which require deepening through further studies and investigations.

Glassy IrMn. IrMn-based magnetic multilayers deposited by magnetron sputtering are extremely common in both research and industrial applications. Nevertheless, to our knowledge this is the first research work in which IrMn is deposited in an amorphous state. The reason of this probably lies in the small window of the sputtering conditions for the deposition of glassy IrMn. A systematic study of the deposition of glassy IrMn should include the effects of RF vs DC magnetron sputtering, as well as varying multiple parameters such as the growth rate, the Ar pressure, the composition of the IrMn target and the substrate temperature.

Crystallization of IrMn. A thorough characterization of the crystallization of the amorphous IrMn should include isothermal as well as non-isothermal kinetics studies, at different temperatures and heat flows. The investigations should be repeated for different deposition parameters and material compositions and thicknesses, so to correlate the nucleation and growth activation energy to the characteristics of the deposited IrMn. Such a tuning of the

activation energy could allow the precise control of the phase transition process by varying the sample temperature.

Role of the FeCo layer. The TEM images presented here indicate that the polycrystalline nature of the FeCo layer plays a crucial role in the formation of stacking faults during the crystallization of the IrMn. Further TEM characterization of samples with FeCo deposited at different sputtering conditions may clarify how the FeCo affects the microstructure of the crystallizing IrMn. In addition, the control of the phase transition process could allow the investigation on how the role of the FeCo layer changes at different growth rates of the crystalline phase.

Role of the seed layer. In the present work we showed that the IrMn crystallizes with (111) texture even in absence of a seed layer. We also showed that, despite the Ta seed layer, few samples developed a mixed (111) and (100) texture. Nevertheless, these peculiar samples show a strong exchange bias. Hence, the role of the seed layer must be clarified. A systematic study should also include additional materials commonly used in industrial application as a seed layer for exchange-biased systems, such as NiFeCr [Dieny, 2004].

Role of defects and interfacial roughness. TEM imaging showed that the interface roughness may play a crucial role by promoting the (111) texture even in (100) oriented IrMn. Ideally speaking, a (100) textured sample with a rough interface could present a large amount of exposed (111) planes, even larger than in a sample with a perfect interface and (111) texture. Similar situations can occur with frequent structural defects. This research option is even more interesting in light of the possible spin clusters which could form at these sites.

Thickness of IrMn. The magnetic characterization of AF/F-type samples with 15-nm-thick IrMn layers showed moderately strong and thermally stable exchange bias. However, this thickness of the AF layer is the double of what is usually employed in industrial applications. In addition, the possibility of generating very large AF grains by controlling the phase transition in the AF material, opens the door to further reducing of the AF thickness. Hence, the study of the magnetic and thermal response of similar samples, but with thinner IrMn layer, could be interesting for industrial applications.

Spontaneous EB setting at high fields. In the present work the spontaneous formation of the exchange bias inevitably occurred in absence of an external magnetic field, due to technical limitations. However, it is well known that the exchange bias is strengthened when set in presence of high external fields, with improvements of the exchange bias field up to 30 %. As

this is thought to be related to ferromagnetically alignment of the interfacial spin clusters, it would be interesting to analyze the effect of the initial increase of H_{eb} in presence of high fields.

Low temperature magnetic measurements. An important increase of the exchange bias field is detected in samples cooled at liquid-helium temperatures. This phenomenon is believed to be the consequence of the low temperature ordering of the interfacial spin clusters. Again, this kind of characterization on the samples studied in the present work could give a possible indication of the correctness of the proposed mechanism for the exchange bias setting, by confirming the role of the predicted spin clusters.

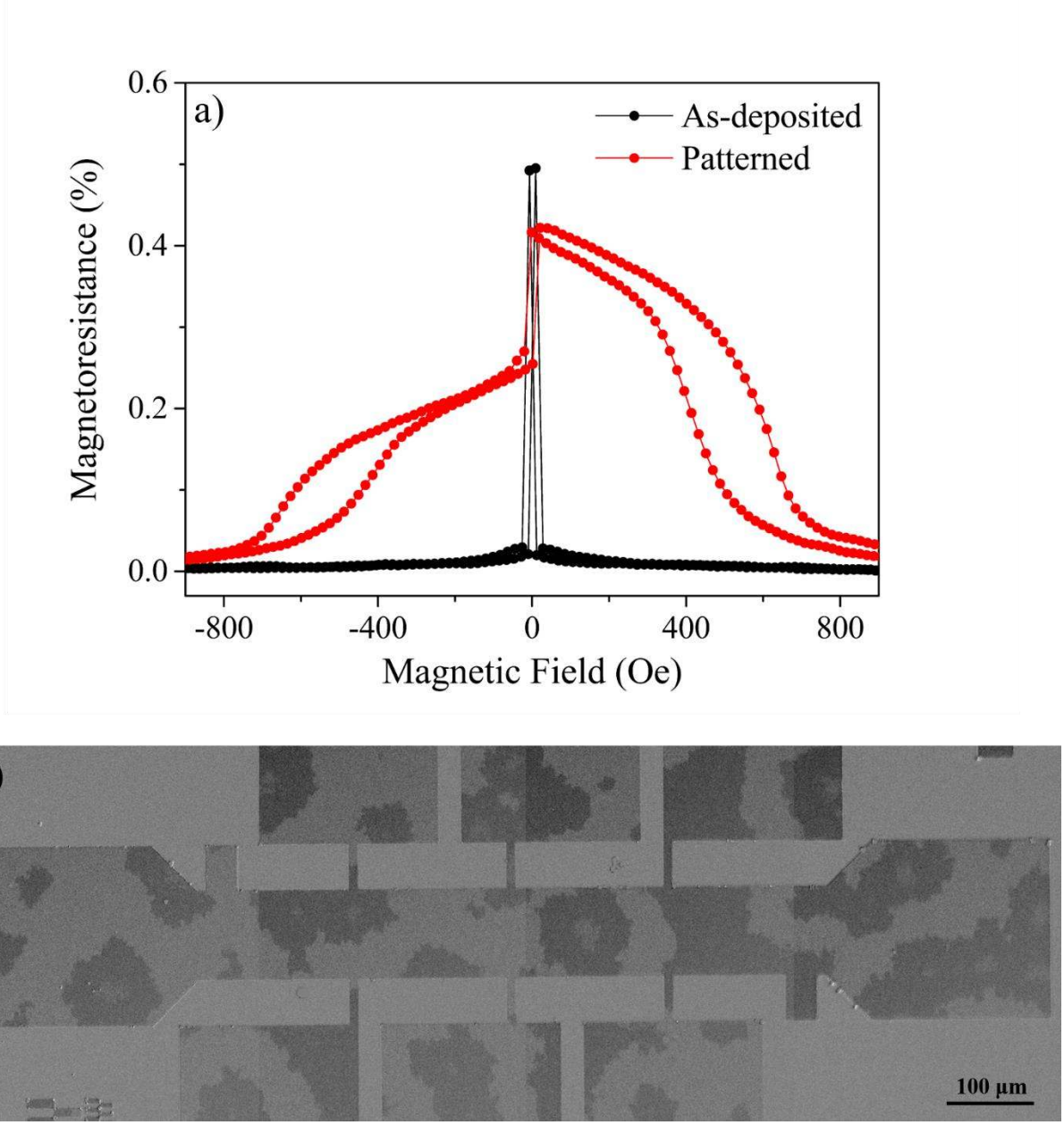

Figure 6.1: a) Magnetoresistive response of a spin valve, with amorphous IrMn (black curve) and after the patterning of the exchange bias (red curve); b) Kerr images of one of the microdevices with patterned EB.

Anisotropy dispersion analysis. During the conventional setting of the exchange bias, the shape of the hysteresis loop improves drastically at moderate temperatures. We interpreted this change as a reduction of the anisotropy dispersion in the samples due to the field annealing. Nevertheless, a dispersion analysis via vector-MOKE measurements at various stages of the setting procedure may clarify what is the origin of the initial shape improvement, and the subsequent exchange bias field reduction.

One of the collateral work that our research group is developing consists in the study of the magnetic dynamics of the free layer of spin valves with patterned exchange bias, in micro- and nanodevices. Some results from preliminary works are shown in figure 6.1. The deposited spin valves have the following structure: SL/IrMn(15nm)/FeCo(5nm)/Cu(2.5nm)/FeNi(6nm)/CL. Micro- and nanodevices are produced by optical and e-beam lithography, and then by lift-off or dry etching processes. These devices are characterized through magnetoresistive measurements, and the response of an as-deposited sample is represented by the black curve in figure 6.1a. As the IrMn is amorphous, there is no exchange bias and both the F layers switch at small external fields. Then, during the crystallization of the IrMn, the remanent magnetization of the FeCo layer is inverted repeatedly, so to achieve the desired patterning of the exchange bias direction. A Kerr image of one of these microdevices is shown in figure 6.1b, where dark and bright contrasts correspond to oppositely directed exchange-biased areas. The resulting MR response is represented by the red curve in figure 6.1a. The analysis of the magnetic dynamics of the free layer in such devices is under development.

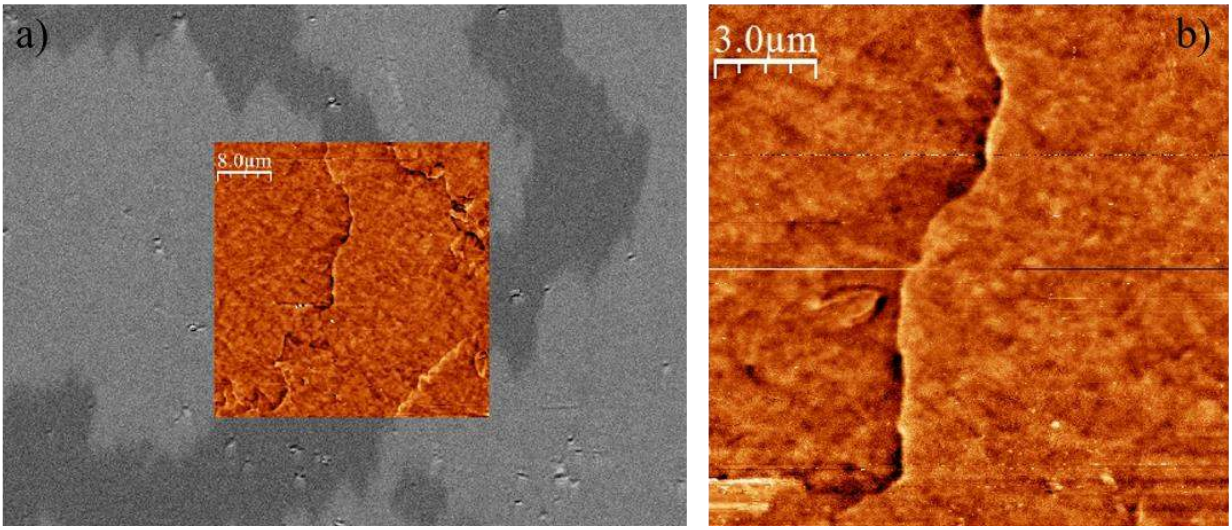

Figure 6.2: a) Imaging of a sample with patterned exchange bias, measured by Kerr microscopy and MFM; b) magnified MFM image of a DW at the boundaries between oppositely oriented exchange-biased areas.

Another research work that our group is developing consists in the study of the strongly pinned magnetic features detected by MFM measurements. These features include both the DWs which separate areas with oppositely directed exchange bias, and the dotted areas located far from the boundaries, which may result from the predicted strongly pinned interfacial spin clusters. Figure 6.2a shows superimposed Kerr and MFM images of the same area of an AF/F-type sample. MFM measurements here are taken at zero applied field. A magnified MFM image is shown in figure 6.2b, where both a DW and the richness of the magnetic microstructure of the sample can be appreciated. The research may also involve further TEM characterization, mainly through Lorentz microscopy.

In conclusion, the results presented in this research work open the door to explore local magnetic interactions at the interface between the AF and the F layers, as well as study the magnetic behavior of DWs at the boundaries between oppositely directed exchange-biased areas. Furthermore, this alternative mechanism to establish the exchange bias could contribute to the improvement of the thermal stability of modern technological applications based on the exchange bias, as well as to design innovative devices.

References

Åkerman, J. Toward a universal memory. *Science* **308,** 508–510 (2005).

Aley, N. P. *et al.* Texture effects in IrMn/CoFe exchange bias systems. *IEEE Trans. Magn.* **44,** 2820–2823 (2008).

Aley, N. P., Bonet, C., Lafferty, B. & O'Grady, K. Effect of Cu Impurities on K_{AF} in $IrMn_{1-x}Cu_x$/CoFe Exchange Bias System. *IEEE Trans. Magn.* **45,** 3858–3861 (2009).

Ali, M. *et al.* Antiferromagnetic layer thickness dependence of the IrMn/Co exchange-bias system. *Phys. Rev. B* **68,** 214420 (2003).

Anderson, G., Huai, Y. & Miloslawsky, L. CoFe/IrMn exchange biased top, bottom, and dual spin valves. *J. Appl. Phys.* **87,** 6989–6991 (2000).

Avrami, M. Kinetics of Phase Change. I General Theory. *J. Chem. Phys.* **7,** 1103–1112 (1939).

Avrami, M. Kinetics of Phase Change. II Transformation-Time Relations for Random Distribution of Nuclei. *J. Chem. Phys.* **8,** 212–224 (1940).

Avrami, M. Granulation, Phase Change, and Microstructure Kinetics of Phase Change. III. *J. Chem. Phys.* **9,** 177–184 (1941).

Baibich, M. N. *et al.* Giant magnetoresistance of (001)Fe/(001)Cr magnetic superlattices. *Phys. Rev. Lett.* **61,** 2472–2475 (1988).

Bennett, M. R. & Wright, J. G. Amorphous films of the transition elements. *Phys. Status Solidi* **13,** 135–144 (1972).

Berkowitz, A. E. & Takano, K. Exchange anisotropy — a review. *J. Magn. Magn. Mater.* **200,** 552–570 (1999).

Binasch, G., Grünberg, P., Saurenbach, F. & Zinn, W. Enhanced magnetoresistance in layered magnetic structures with antiferromagnetic interlayer exchange. *Phys. Rev. B* **39,** 4828–4830 (1989).

Binnig, G., Quate, C. F. & Gerber, C. Atomic Force Microscope. *Phys. Rev. Lett.* **56,** 930–933 (1986).

Camarero, J. *et al.* Origin of the Asymmetric Magnetization Reversal Behavior in Exchange-Biased Systems: Competing Anisotropies. *Phys. Rev. Lett.* **95,** 57204 (2005).

Cardoso, S., Freitas, P. P., Jesus, C. de, Wei, P. & Soares, J. C. Spin-tunnel-junction thermal stability and interface interdiffusion above 300 °C. *Appl. Phys. Lett.* **76,** 610 (2000).

Chikazumi, S. *Physics of Ferromagnetism, 2nd ed.* (Oxford University Press, Oxford, 1997)

Childress, J. R. *et al.* IrMn spin-valves for high density recording. *IEEE Trans. Magn.* **37,** 1745–1748 (2001).

Childress, J. R. & Fontana, R. E. Magnetic recording read head sensor technology. *Comptes Rendus Phys.* **6,** 997–1012 (2005).

Cullity, B. D., Stock, S. R. *Elements of X-Ray Diffraction, 3rd ed.* (Pearson Education Limited, Harlow, 2014).

Daughton, J. M. Magnetoresistive memory technology. *Thin Solid Films* **216,** 162–168 (1992).

Daughton, J. *et al.* Magnetic Field Sensors Using GMR Multilayer. *IEEE Trans. Magn.* **30,** 4608–4610 (1994).

Devasahayam, A. J., Sides, P. J. & Kryder, M. H. Magnetic, temperature, and corrosion properties of the NiFe/IrMn exchange couple. *J. Appl. Phys.* **83,** 7216–7218 (1998).

Dieny, B. *et al.* Giant magnetoresistive in soft ferromagnetic multilayers. *Phys. Rev. B* **43,** 1297–1300 (1991).

Dieny, B. *Spin valves*, in M. Johnson (Ed.), *Magnetoelectronics* (Elsevier Academic Press, Amsterdam, 2004)

Porter, D. A. *Phase Transformations in Metals and Alloys, 3rd ed.* (CRC Press, Boca Raton, 2009)

Egerton, R. F. *Physical Principles of Electron Microscopy. An Introduction to TEM, SEM, and AEM, 2nd ed.* (Springer International Publishing, Switzerland, 2016)

El-Hilo, M., O'Grady, K. & Chantrell, R. W. The origin of non-linear ln(t) behaviour in the time dependence of magnetisation. *J. Magn. Magn. Mater.* **109,** L164–L168 (1992).

Feldman, M. *Nanolithography. The art of fabricating nanoelectronic and nanophotonic devices and systems* (Woodhead Publishing, Cambridge, 2014)

Fernandez-Outon, L. E., O'Grady, K. & Carey, M. J. Thermal phenomena in IrMn exchange biased systems. *J. Appl. Phys.* **95,** 6852–6854 (2004).

Fernandez-Outon, L. E., Vallejo-Fernandez, G., Manzoor, S. & O'Grady, K. Thermal instabilities in exchange biased materials. *J. Magn. Magn. Mater.* **303,** 296–301 (2006).

Fernandez-Outon, L. E., Vallejo-Fernandez, G. & O'Grady, K. Interfacial spin effects on Hex in metallic polycrystalline exchange biased systems. *J. Appl. Phys.* **103,** 07C106 (2008).

Fecioru-Morariu, M., Ali, S. R., Papusoi, C., Sperlich, M. & Güntherodt, G. Effects of Cu dilution in IrMn on the exchange bias of CoFe/IrMn bilayers. *Phys. Rev. Lett.* **99,** 97206 (2007).

Fecioru-Morariu, M. *Exchange Bias by Antiferromagnetic Oxides*, in L. Duò, M. Finazzi & F.Ciccacci (Eds.), *Magnetic Properties of Antiferromagnetic Oxide Materials. Surfaces, Interfaces, and Thin Films.* (Wiley-VCH, Weinheim, 2010)

Fitzsimmons, M. R. *et al.* Asymmetric magnetization reversal in exchange-biased hysteresis loops. *Phys. Rev. Lett.* **84,** 3986–3989 (2000).

Foner, S. Versatile and Sensitive Vibrating-Sample Magnetometer. *Rev. Sci. Instrum.* **30,** 548–557 (1959).

Fuke, H. N., Saito, K., Kamiguchi, Y., Iwasaki, H. & Sahashi, M. Spin-valve giant magnetoresistive films with antiferromagnetic Ir-Mn layers. *J. Appl. Phys.* **81,** 4004 (1997).

Fulcomer, E. & Charap, S. H. Temperature and frequency dependence of exchange anisotropy effects in oxidized NiFe films. *J. Appl. Phys.* **43,** 4184–4190 (1972a).

Fulcomer, E. & Charap, S. H. Thermal fluctuation aftereffect model for some systems with ferromagnetic-antiferromagnetic coupling. *J. Appl. Phys.* **43,** 4190–4199 (1972b).

Fultz, B. *Transmission Electron Microscopy and Diffractometry of Materials, 4th ed.* (Springer-Verlag, Berlin, 2013)

Grove, W. R. On the Electro-Chemical Polarity of Gases. *Philos. Trans. R. Soc. London* **142,** 87–101 (1852).

Guinebretière, R. *X-Ray Diffraction by Polycrystalline Materials* (Wiley-ISTE, London, 2007).

Hagedorn, F. B. Exchange anisotropy in oxidized permalloy thin films at low temperatures. *J. Appl. Phys.* **38,** 3641–3645 (1967).

Haugstad, G. *Atomic Force Microscopy: Understanding Basic Modes and Advanced Applications* (Wiley, Hoboken, 2012)

Hirth, J. P. *Theory of dislocations, 2nd ed.* (Krieger Pub. Co, Malabar, 1982)

Hoffmann, A. Symmetry Driven Irreversibilities at Ferromagnetic-Antiferromagnetic Interfaces. *Phys. Rev. Lett.* **93,** 97203 (2004).

Hoshino, K., Nakatani, R., Hoshiya, H., Sugita, Y. & Tsunashima, S. Exchange Coupling between Antiferromagnetic Mn–Ir and Ferromagnetic Ni–Fe Layers. *Jpn. J. Appl. Phys.* **35,** 607–612 (1996).

Hubert, A. *Magnetic Domains: The Analysis of Magnetic Microstructures* (Springer-Verlag, Berlin, 1998)

Imakita, K. I., Tsunoda, M. & Takahashi, M. Giant exchange anisotropy observed in Mn-Ir/Co-Fe bilayers containing ordered Mn3Ir phase. *Appl. Phys. Lett.* **85,** 3812–3814 (2004).

Imakita, K. I., Tsunoda, M. & Takahashi, M. Thickness dependence of exchange anisotropy of polycrystalline Mn3Ir/Co-Fe bilayers. *J. Appl. Phys.* **97,** 1–4 (2005).

Iwasaki, H., Saito, A. T., Tsutai, A. & Sahashi, M. Excellent reliability of CoFe-IrMn spin valves. *IEEE Trans. Magn.* **33,** 2875–2877 (1997).

Jacobs, I. S. & Kouvel, J. S. Exchange anisotropy in mixed manganites with the hausmannite structure. *Phys. Rev.* **122,** 412–418 (1961).

Jeong, T. H., Kim, M. R., Seo, H., Kim, S. J. & Kim, S. Y. Crystallization behavior of sputter-deposited amorphous Ge2Sb2Te5 thin films. *J. Appl. Phys.* **86,** 774–778 (1999).

Jiang, X., Zhang, H., Wen, Q., Zhong, Z.-Y. & Tang, X. Crystallization kinetics of magnetron-sputtered amorphous CoNbZr thin films. *Vacuum* **77,** 209–215 (2005).

Johnson, W. A. & Mehl, R. F. Reaction kinetics in processes of nucleation and growth. *Tranz AIME* **135,** 416 (1939).

Johnson, A. (2003). *Spin Valve Systems for Angle Sensor Applications* (Doctoral dissertation)

Johnson, M. *Magnetoelectronics* (Elsevier Academic Press, Amsterdam, 2004)

Jungwirth, T., Marti, X.,Wadley, P. & Wunderlich, J. Antiferromagnetic spintronics. *Nat. Nanotech.* **11,** 231-241 (2016).

Keller, J. *et al.* Domain state model for exchange bias. II. Experiments. *Phys. Rev. B* **66,** 14431 (2002).

Kelly, P. J. & Arnell, R. D. Magnetron sputtering: a review of recent developments and applications. *Vacuum* **56,** 159–172 (2000).

Kelly, A. *Crystallography and Crystal Defects, 2nd ed.* (Wiley, Chichester, 2012)

Kent, A. D. & Worledge, D. C. A new spin on magnetic memories. *Nat. Nanotech*. **10,** 187-191 (2015).

Kerr, J. On rotation of the plane of polarization by reflection from the pole of a magnet. *Phil. Mag. (5)* **3,** 321–343 (1877)

Kiwi, M. Exchange bias theory. *J. Magn. Magn. Mater.* **234,** 584–595 (2001).

Knoll, M. & Ruska, E. Das Elektronenmikroskop (Electron Microscope) *Z. Phys.* **78,** 318–339 (1932).

Kohn, A. *et al.* The antiferromagnetic structures of IrMn3 and their influence on exchange-bias. *Sci. Rep.* **3,** 2412 (2013).

Kolmogorov, A. N. *On the Statistical Theory of Metal Crystallization,* in A. N. Shiryayev (Ed.), *Selected Works of A. N. Kolmogorov, vol. II* (Springer Science, Moscow, 1992)

Koon, N. C. Calculations of Exchange Bias in Thin Films with Ferromagnetic/Antiferromagnetic Interfaces. *Phys. Rev. Lett.* **78,** 4865–4868 (1997).

Kramer, J. Über nichtleitende Metallmodifikationen. *Ann. Phys.* **411,** 37–64 (1934).

Lahtinen, T. H. E., Franke, K. J. A. & van Dijken, S. Electric-field control of magnetic domain wall motion and local magnetization reversal. *Sci. Rep.* **2,** 258 (2012).

Leung, P. K. & Wright, J. G. Structural investigations of amorphous transition element films: II. Chromium, iron, manganese and nickel. *Philos. Mag.* **30,** 995–1008 (1974).

Lee, H.-J. & Ramirez, A. G. Crystallization and phase transformations in amorphous NiTi thin films for microelectromechanical systems. *Appl. Phys. Lett.* **85,** 1146–1148 (2004).

Liebermann, H. H. *Sample preparation: methods and process characterization*, in F. E. Luborsky (Ed.), *Amorphous Metallic Alloys* (Butterworth-Heinemann, London, 1983)

Liu, K. T. & Duh, J. G. Kinetics of the crystallization in amorphous NiTi thin films. *J. Non. Cryst. Solids* **353,** 1060–1064 (2007).

Luborsky, F. E. *Amorphous Metallic Alloys*, in F. E. Luborsky (Ed.), *Amorphous Metallic Alloys* (Butterworth-Heinemann, London, 1983)

Malozemoff, A. P. Random-field model of exchange anisotropy at rough ferromagnetic-antiferromagnetic interfaces. *Phys. Rev. B* **35,** 3679–3682 (1987).

Martí, X. et al. Electrical measurement of antiferromagnetic moments in exchange-coupled IrMn/NiFe stacks. *Phys. Rev. Lett.* **108,** 017201 (2012).

Mastai, Y. *Advances in Crystallization Processes* (Intech, Rijeka, 2012)

Mauri, D., Siegmann, H. C., Bagus, P. S. & Kay, E. Simple model for thin ferromagnetic films exchange coupled to an antiferromagnetic substrate. *J. Appl. Phys.* **62,** 3047–3049 (1987).

McCord, J., Schäfer, R., Mattheis, R. & Barholz, K.-U. Kerr observations of asymmetric magnetization reversal processes in CoFe/IrMn bilayer systems. *J. Appl. Phys.* **93,** 5491–5497 (2003).

McFadyen, I. R., Fullerton, E. E. & Carey, M. J. State-of-the-Art Magnetic Hard Disk Drives. *MRS Bull.* **31,** 379–383 (2006).

Meiklejohn, W. H. & Bean, C. P. New Magnetic Anisotropy. *Phys. Rev.* **102,** 1413–1414 (1956).

Meiklejohn, W. H. & Bean, C. P. New Magnetic Anisotropy. *Phys. Rev.* **105,** 904–913 (1957).

Meinert, M., Büker, B., Graulich, D. & Dunz, M. Large exchange bias in polycrystalline MnN/CoFe bilayers at room temperature. *Phys. Rev. B - Condens. Matter Mater. Phys.* **92,** 1–7 (2015).

Meyer, E. *Scanning Probe Microscopy* (Springer-Verlag, Berlin, 2004)

Migliorini, A. *et al.* Spontaneous exchange bias formation driven by a structural phase transition in the antiferromagnetic material. *Nat. Mater.* **17,** 28–34 (2018).

Miltényi, P. *et al.* Diluted Antiferromagnets in Exchange Bias: Proof of the Domain State Model. *Phys. Rev. Lett.* **84,** 4224–4227 (2000).

Morales, R. et al. Exchange-bias phenomenon: the role of the ferromagnetic spin structure. *Phys. Rev. Lett.* **114,** 097202 (2015).

Mougin, A. *et al.* Modification of the exchange bias effect by He ion irradiation. *IEEE Trans. Magn.* **36,** 2647–2649 (2000).

Mougin, A. *et al.* Magnetic micropatterning of FeNi/FeMn exchange bias bilayers by ion irradiation. *J. Appl. Phys.* **89,** 6606–6608 (2001).

Néel, L. *Ann. Phys. (Paris)* **2,** 61 (1967).

Njoroge, W. K. & Wuttig, M. Crystallization kinetics of sputter-deposited amorphous AgInSbTe films. *J. Appl. Phys.* **90,** 3816–3821 (2001).

Nogués, J. & Schuller, I. K. Exchange bias. *J. Magn. Magn. Mater.* **192,** 203–232 (1999).

Nogués, J., Leighton, C. & Schuller, I. K. Correlation between antiferromagnetic interface coupling and positive exchange bias. *Phys. Rev. B* **61,** 1315–1317 (2000).

Nogués, J. *et al.* Exchange bias in nanostructures. *Phys. Rep.* **422,** 65–117 (2005).

Nowak, U. *et al.* Domain state model for exchange bias. I. Theory. *Phys. Rev. B* **66,** 14430 (2002).

O'Grady, K., Chantrell, R., Popplewell, J. & Charles, S. Time dependent magnetization of a system of fine cobalt particles. *IEEE Trans. Magn.* **17,** 2943–2945 (1981).

O'Grady, K., Fernandez-Outon, L. E. & Vallejo-Fernandez, G. A new paradigm for exchange bias in polycrystalline thin films. *J. Magn. Magn. Mater.* **322,** 883–899 (2010).

Očenášek, J., Novák, P. & Agbo, S. Finite-thickness effect on crystallization kinetics in thin films and its adaptation in the Johnson–Mehl–Avrami–Kolmogorov model. *J. Appl. Phys.* **115,** 43505 (2014).

Ohldag, H. *et al.* Correlation between Exchange Bias and Pinned Interfacial Spins. *Phys. Rev. Lett.* **91,** 17203 (2003).

Paccard, D., Schlenker, C., Massenet, O., Montmory, R. & Yelon, A. A New Property of Ferromagnetic-Antiferromagnetic Coupling. *Phys. Status Solidi* **16,** 301–311 (1966).

Paetzold, A. & Röll, K. Thermally activated self-alignment of exchange coupling in NiO/NiFe bilayers. *J. Appl. Phys.* **91,** 7748–7750 (2002).

Pakala, M., Huai, Y., Anderson, G. & Miloslavsky, L. Effect of underlayer roughness, grain size, and crystal texture on exchange coupled IrMn/CoFe thin films. *J. Appl. Phys.* **87,** 6653–6655 (2000).

Phillips, J. C. Stretched exponential relaxation in molecular and electronic glasses. *Reports Prog. Phys.* **59,** 1133–1207 (1996).

Phillips, R. Crystals, *Defects and Microstructures. Modeling Across Scales* (Cambridge University Press, Cambridge, 2001)

Polisetty, S., Sahoo, S. & Binek, C. Scaling behavior of the exchange-bias training effect. *Phys. Rev. B* **76,** 184423 (2007).

Proenca, M. P., Ventura, J., Sousa, C. T., Vazquez, M. & Araujo, J. P. Exchange bias, training effect, and bimodal distribution of blocking temperatures in electrodeposited core-shell nanotubes. *Phys. Rev. B - Condens. Matter Mater. Phys.* **87,** 1–7 (2013).

Raub, E. & Mahler, W. Alloys of Manganese with Platinum, Iridium, Rhodium, and Ruthenium. *Z. Metallkd.* **46**(4), 282–290 (1955).

Samant, M. G., Lüning, J., Stöhr, J. & Parkin, S. S. P. Thermal stability of IrMn and MnFe exchange-biased magnetic tunnel junctions. *Appl. Phys. Lett.* **76,** 3097–3099 (2000).

Schlenker, C. Couplage ferro-antiferromagnétique et traînage magnétique dans des couches minces multiples Co-CoO et Ni-NiO. *Phys. Status Solidi* **28,** 507–517 (1968).

Scott, M. G. *Crystallization*, in F. E. Luborsky (Ed.), *Amorphous Metallic Alloys* (Butterworth-Heinemann, London, 1983)

Sharma, J. & Suresh, K. G. Observation of giant exchange bias in bulk $Mn_{50}Ni_{42}Sn_8$ Heusler alloy. *Appl. Phys. Lett.* **106,** 072405 (2015)

Sharma, S. K. *Exchange Bias. From Thin Film to Nanogranular and Bulk Systems* (CRC Press, Boca Raton, 2017)

Stamps, R. L. Mechanism for exchange bias. *J. Phys. D. Appl. Phys.* **33,** 247–268 (2000).

Takahashi, M., Yanai, A., Taguchi, S. & Suzuki, T. A Study of Exchange Anisotropy in Co-CoO Evaporated Thin Films. *Jpn. J. Appl. Phys.* **19,** 1093–1106 (1980).

Thomas, L. & Negulescu, B. Metastable antiferromagnetic domain configurations in exchange biased bilayers. *J. Appl. Phys.* **93,** 8606–8608 (2003).

Tsang, C. *et al.* Design, Fabrication & Testing of Spin-Valve Read Heads for High Density Recording. *IEEE Trans. Magn.* **30,** 3801–3806 (1994).

Tsunoda, M., Imakita, K. ichi, Naka, M. & Takahashi, M. L12 phase formation and giant exchange anisotropy in Mn3Ir/Co-Fe bilayers. *J. Magn. Magn. Mater.* **304,** 55–59 (2006).

Tumanski, S. *Handbook of Magnetic Measurements* (CRC Press, Boca Raton, 2011)

Ueltzhöffer, T. *et al.* Néel walls between tailored parallel-stripe domains in IrMn/CoFe exchange bias layers. *J. Appl. Phys.* **117,** 1–6 (2015).

Vallejo-Fernandez, G., Fernandez-Outon, L. E. & O'Grady, K. Measurement of the anisotropy constant of antiferromagnets in metallic polycrystalline exchange biased systems. *Appl. Phys. Lett.* **91,** 212503 (2007).

Vallejo-Fernandez, G., Kaeswurm, B., Fernandez-Outon, L. E. & O'Grady, K. Effect of the Ferromagnetic Layer Thickness on the Blocking Temperature in IrMn/CoFe Exchange Couples. *IEEE Trans. Magn.* **44,** 2835–2838 (2008a).

Vallejo-Fernandez, G., Fernandez-Outon, L. E. & O'Grady, K. Antiferromagnetic grain volume effects in metallic polycrystalline exchange bias systems. *J. Phys. D. Appl. Phys.* **41,** 112001 (2008b).

Vallejo-Fernandez, G., Aley, N. P., Fernandez-Outon, L. E. & O'Grady, K. Control of the setting process in CoFe/IrMn exchange bias systems. *J. Appl. Phys.* **104,** 1–6 (2008c).

Vallejo-Fernandez, G., Aley, N. P., Chapman, J. N. & O'Grady, K. Measurement of the attempt frequency in antiferromagnets. *Appl. Phys. Lett.* **97,** 3–6 (2010).

Vallejo-Fernandez, G., Kaeswurm, B. & O'Grady, K. Defect and impurity effects in exchange bias systems. *J. Appl. Phys.* **109,** 07D738 (2011a).

Vallejo-Fernandez, G. & O'Grady, K. Effect of Non-Magnetic Dilutions on the Blocking temperature of Exchange Biased Systems. *IEEE Trans. Magn.* **47,** 3304–3307 (2011b).

van der Heijden, P. A. A. *et al.* Thermally assisted reversal of exchange biasing in NiO and FeMn based systems. *Appl. Phys. Lett.* **72,** 492–494 (1998).

van Driel, J., de Boer, F. R., Lenssen, K.-M. H. & Coehoorn, R. Exchange biasing by Ir19Mn81: Dependence on temperature, microstructure and antiferromagnetic layer thickness. *J. Appl. Phys.* **88,** 975–982 (2000).

Vopsaroiu, M. *et al.* Deposition of polycrystalline thin films with controlled grain size. *J. Phys. D. Appl. Phys.* **38,** 490–496 (2005).

Wang, Y. Y. et al. Room-temperature perpendicular exchange coupling and tunneling anisotropic magnetoresistance in an antiferromagnet-based tunnel junction. *Phys. Rev. Lett.* **109,** 137201 (2012).

Williams, D. B. *Transmission electron microscopy. A Textbook for Materials Scien*ce (Springer Science, New York, 2009)

Wolf, S. A. *et al.* Spintronics: A spin-based electronics vision for the future. *Science* **294,** 1488–1495 (2001).

Wu, J. et al. Direct measurement of rotatable and frozen CoO spins in exchange bias system of CoO/Fe/Ag(001). *Phys. Rev. Lett.* **104,** 217204 (2010).

Xi, H. & White, R. M. Antiferromagnetic thickness dependence of exchange biasing. *Phys. Rev. B - Condens. Matter Mater. Phys.* **61,** 80–83 (2000).

Xi, H., Franzen, S., Mao, S. & White, R. M. Exchange bias relaxation in reverse magnetic fields. *Phys. Rev. B* **75,** 14434 (2007).

Yagami, K., Tsunoda, M. & Takahashi, M. Enhancement of exchange bias in Mn–Ir/Co–Fe based spin valves with an ultrathin Cu underlayer and in situ Mn–Ir surface modification. *J. Appl. Phys.* **89,** 6609–6611 (2001).

Yamaoka, T. Antiferromagnetism in γ-Phase Mn-Ir Alloys. *J. Phys. Soc. Japan* **36,** 445–450 (1974).

Yoo, C. S. *et al.* Effect of diffusion barrier in the thermally annealed exchange-biased IrMn-CoFe electrode in magnetic tunnel junctions. *IEEE Trans. Magn.* **38,** 2715–2717 (2002).

Zhang, L., Xie, C. & Wu, J. In situ X-ray diffraction analysis on the crystallization of amorphous Ti–Ni thin films. *Scr. Mater.* **55,** 609–612 (2006).

Zhang, W. & Krishnan, K. M. Epitaxial exchange-bias systems: From fundamentals to future spin-orbitronics. *Mater. Sci. Eng. R Reports* **105,** 1–20 (2016).

Zhou, X. et al. Mapping motion of antiferromagnetic interfacial uncompensated magnetic moment in exchange-biased bilayers. *Sci. Rep.* **5,** 9183 (2015).